PZE-transduced Suspended Microchannel Resonators for sensing applications

THÈSE Nº 8624 (2018)

PRÉSENTÉE LE 13 JUILLET 2018

À LA FACULTÉ DES SCIENCES ET TECHNIQUES DE L'INGÉNIEUR

LABORATOIRE DE MICROSYSTÈMES 1

PROGRAMME DOCTORAL EN MICROSYSTÈMES ET MICROÉLECTRONIQUE

ÉCOLE POLYTECHNIQUE FÉDÉRALE DE LAUSANNE

POUR L'OBTENTION DU GRADE DE DOCTEUR ÈS SCIENCES

PAR

Annalisa DE PASTINA

acceptée sur proposition du jury:

Prof. J. Brugger, président du jury Prof. L. G. Villanueva Torrijo, directeur de thèse Prof. A. Boisen, rapporteuse Prof. S. Manalis, rapporteur Prof. F. Gallaire, rapporteur







Abstract

This PhD thesis aims at developing a system which can measure the mechanical properties of fluidic samples in the picoliter range. The ultimate goal is the characterization of cancer cells and viscoelastic fluids (i.e. biological fluids), in order to study their *mass* and *stiffness* for diagnostic applications.

The core of this project is the design, fabrication and characterization of hollow micromechanical resonators containing embedded microfluidic channels and provided with integrated piezoelectric (PZE) transduction. The measurement strategy consists in monitoring the device resonance frequency over time, while the analyte flows through the microchannel.

Arrays of singly-clamped and doubly-clamped *resonators* are made of low stress Silicon Nitride (Is-SiN_x) and vibrate in a frequency range from tens of kHz to few MHz. *Microfluidic channels* span 25%, 60% and 100% of the cantilever length in order to compare the resonance frequency shift induced by the same particle at different positions, along identically-designed beams. The goal is to disentangle analyte *mass* and *stiffness* contribution from the suspended microchannel resonator (SMR) mechanical response. The cross section of the *suspended fluidic channel*, 6 μ m x 10 μ m, is designed to measure particles in the same size range (i.e. red blood cells or circulating tumor cells). This aims at keeping the cell constrained in the channel and maximize its effect on the frequency response.

SMR energy dissipation is studied via FEM simulation, as a function of fluidic properties and geometrical dimensions. A coupled fluid-structure interaction (FSI) problem, based on linear elasticity and linearized Navier Stokes equations, is studied. The model is found well in agreement with theory and experiments presented in literature, considering the viscosity range of interest in case of biosensing application (1 – 1000 mPa s).

The fabrication of transparent and PZE-transduced suspended microchannel resonators is achieved via a 6-mask process flow. 250, 500, 750 and 1000 µm long singly- and doubly-clamped SMRs are fabricated. Microfluidic channels are defined via the etching of high aspect ratio-trenches through a sacrificial layer of polysilicon, and filled with ls-SiN_x. *Discontinuous etch apertures* are defined on top of the buried fluidic network and enable channel emptying in 25 minutes via KOH etching. PZE electrodes in platinum and aluminum nitride are deposited via sputter deposition and provide independent actuation and readout of each resonator, for the first time in SMR arrays.

The development of an *experimental platform* enables fluidic and electrical connections, as well as temperature control during devices characterization.

The mechanical response of fabricated sensors is measured in air and vacuum environment, while channels are filled with air, water and Isopropyl Alcohol. PZE electrodes demonstrate efficient actuation, in the order of 1.5 nm/V for $250 \mu m$ - long singly-clamped SMRs. However, PZE detected signals result very low in amplitude, thus optical detection via laser Doppler vibrometer is preferred. The best values obtained for mass and

temperature responsivities, probing singly clamped beams, are 1120 mHz/pg, and 27.76 ppm/°C, respectively. These results are in line with what reported in literature for resonators in the same frequency and mass range.

Frequency stability of fabricated sensors is studied in order to estimate their sensing performances and characterize their physical limitations. $250 \mu m$ -long SMRs filled with DI water exhibit a frequency stability of $30 \mu m$ -long smrs filled with values found in literature for SMRs sensors and translates in an estimated mass sensitivity of few femtograms.

Keywords:

Mechanical sensor	Piezoelectricity	Microtechnology	MEMS
Resonators	FEM simulation	Microfabrication	Frequency noise
Microfluidics	Fluid-structure interaction	Thin films	Allan Deviation

Résumé

Cette thèse de doctorat a pour but le développement d'un système permettant la mesure des propriétés mécaniques d'échantillons fluidiques dans la plage du picolitre. L'objectif ultime est la caractérisation de cellules cancéreuses et de fluides viscoélastiques (par ex : fluides biologiques), afin d'étudier leur *masse* et *rigidité* dans des applications de diagnostic médical (1).

La partie centrale de ce projet est la conception, la fabrication et la caractérisation de résonateurs micromécaniques creux comprenant des canaux microfluidiques et une transduction piézoélectrique intégrée. La stratégie pour les mesures consiste en la surveillance de la fréquence de résonance de l'appareil au cours du temps, alors que l'analyte circule dans le microcanal.

Des séries de *résonateurs* fixés à une ou à leurs deux extrémités sont composés de Nitrure de Silicium à faible tension (ls-SiNx) et vibrent dans une plage de fréquence allant des dizaines de kHz à quelques MHz. Des *canaux microfluidiques* couvrent 25%, 60% et 100% de la longueur de la poutre afin de comparer le changement de la fréquence de résonance provoqué par la même particule à différentes positions, le long de poutres à la conception identique. L'objectif est d'utiliser la réponse mécanique des microcanaux suspendus pour démêler la contribution de l'analyte en *masse* et en *rigidité*. La coupe transversale du canal fluidique suspendu, 6μm x 10μm, est conçue pour mesurer des particules dans la même plage de tailles (par ex : cellules rouges ou cellules tumorales circulantes). Le but est de forcer la cellule à rester dans le canal et de maximiser son effet sur la fréquence de résonance.

La dissipation d'énergie des SMRs est étudiée par simulation avec une méthode à éléments fînis, en fonction des propriétés fluidiques et des dimensions géométriques. Un problème avec interaction couplée fluide/structure, basé sur l'élasticité linéaire et les équations de Navier-Stokes linéarisées, est étudié. Le modèle s'avère être en bon accord avec la théorie et les expériences présentées dans la littérature, en considérant la plage de viscosité d'intérêt dans le cas d'applications de biodétection (1 – 1000 mPa s).

La fabrication de résonateurs à microcanaux suspendus transparents à transduction piézoélectrique est réalisée avec un flux de processus comprenant 6 masques. Des SMRs fixés à une ou à leurs deux extrémités, de longueur 250, 500, 750 et 1000 µm, sont fabriqués. Des canaux microfluidiques sont définis par la gravure de tranchées au rapport d'aspect élevé dans une couche de polysilicium sacrificielle, et le remplissage par ls-SiNx. Des *ouvertures discontinues de gravure* sont définies sur le dessus du réseau fluidique enfoui et permettent de vider les canaux par gravure au KOH en 25 minutes. Les électrodes piézoélectriques en platine et nitrure d'aluminium sont formées par dépositions par pulvérisation et offrent un actionnement et une détection indépendants pour chaque résonateur, pour la première fois dans des séries de résonateurs à microcanaux suspendus.

Le développement d'une *interface expérimentale* permet les connections fluidiques et électriques, ainsi qu'un contrôle de la température durant la caractérisation des appareils.

La réponse mécanique des capteurs fabriqués est mesurée dans un environnement d'air et dans le vide, et les canaux sont remplis d'air, d'eau, et d'alcool isopropylique. Les électrodes piézoélectriques démontrent un actionnement efficace, de l'ordre de 1.5 nm/V pour des SMRs de 250 µm de long fixés à une extrémité. Néanmoins, les signaux piézoélectriques détectés sont très faibles en magnitude, et donc une détection optique avec un vibromètre laser à effet Dopler est préférée. Les meilleures valeurs pour la responsivité en masse et en température, sur des poutres fixées à une extrémité, sont de 1120 mHz/pg et 27.76 ppm/°C, respectivement. Ces résultats sont en adéquation avec les valeurs rapportées dans la littérature pour des résonateurs dans les mêmes plages de fréquences et de masses.

La stabilité en fréquence des capteurs fabriqués est étudiée afin d'estimer leurs performances en détection et de caractériser leurs limites physiques. Des SMRs de 250 µm de long remplis d'eau déionisée montrent une stabilité en fréquence de 30 ppb avec un temps d'intégration de 400 ms, en environnement d'air. Ce résultat est en bon accord avec les valeurs trouvées dans la littérature pour des capteurs SMRs et se traduit par une sensibilité en masse de quelques femtogrammes.

Mots-clés:

Capteur mécanique	Piézoélectricité	Microtechnologie	MEMS
Résonateurs	Simulation FEM	Microfabrication	Bruit fréquentiel
Microfluidique	Interaction	Film fin	Déviation d'Allan
	fluide/structure		

Contents

Abstract		i
Résumé		iii
Contents		v
List of Figu	ures	viii
List of Tab	oles	xii
List of Abb	breviations	xiii
Contributi	ons	xiv
Chapter 1	INTRODUCTION	1
1.1	Motivation	2
	1.1.1 Cell Mechanical Properties	2
	1.1.2 Rheology of complex fluids	4
1.2	Mechanical Biosensors	6
	1.2.1 Static mode biosensors	6
	1.2.2 Dynamic mode biosensors	7
1.3	Suspended microchannel resonators: state of the art	10
	1.3.1 Applications	11
	1.3.2 Transduction techniques	12
1.4	Thesis outline	14
Chapter 2	DESIGN	17
2.1	Introduction	18
2.2	Hollow resonators design	18
	2.2.1 Requirements	18
	2.2.2 Materials and dimensions	20
2.3	Microfluidic network	22
	2.3.1 Requirements	23

	2.3.2 Materials and dimensions	23
2.4	PZE electrodes	25
	2.4.1 Requirements	26
	2.4.2 Materials and dimensions	26
2.5	Complete wafer overview	29
2.6	Chapter conclusion	32
Chapter 3	SIMULATIONS	35
3.1	Introduction	36
3.2	Energy dissipation in SMRs	37
3.3	FEM modeling: Fluid Structure Interaction	39
	3.3.1 Model geometry and mesh	39
	3.3.2 Boundary conditions and physics	41
	3.3.3 Numerical Results	41
3.4	Chapter conclusion	43
Chapter 4	FABRICATION	47
4.1	Introduction	48
	4.1.1 State of the art	48
	4.1.2 Fabrication overview: materials and requirements	50
4.2	Microfluidic channels	51
	4.2.1 Trenches technology	51
	4.2.2 Opening from the bottom	55
	4.2.3 Opening from the top	58
4.3	Piezoelectric electrodes	63
4.4	Release	68
4.5	Chapter conclusion	71
Chapter 5	EXPERIMENTAL SETUP	75
5.1	Introduction	76
	5.1.1 SMR packaging in literature	76
	5.1.2 Packaging strategy	76
5.2	Fluidic interface	77
5.3	Electrical connection	79

5.4	Temperature control	80
5.5	Measurement setup	81
5.6	Chapter conclusion	82
Chapter 6	CHARACTERIZATION	85
6.1	Piezoelectric Transduction	86
6.2	Mass Responsivity	90
6.3	Fluidic parameters	92
6.4	Temperature Responsivity	94
6.5	Study of frequency stability	96
	6.5.1 Allan variance	97
	6.5.2 Experimental parameters	99
	6.5.3 Experimental results	101
	6.5.4 Beads	106
6.6	Chapter Conclusion	
Chapter 7	CONCLUSIONS AND OUTLOOK	111
7.1	Conclusions	
7.2	Future development	114
Appendix .	A Full Fabrication Process Flow	117
Appendix 1	B Fabrication Run Card	123
Appendix	C Wafer Layout	136
Appendix 1	D Microfluidic connector: drawings	137
	First Prototype	
	Second Prototype: Bypass Channels	
Appendix 1	E Codes	140
	Lorentzian Fit – Matlab	
	Allan Deviation – Matlab	141
	Resonator parameters – Mathematica code	143
Bibliograp	hy	148
Curricului	n Vitae	154
Acknowled	lgements.	158

List of Figures

Figure 1.1: Few examples of microfluidic chips for CTC isolation based on their mechanical properties4
Figure 1.2: Schematic of the microfluidic device used by Prof. Toner's group (top), computational simulation
(centre) and optical pictures (bottom)4
Figure 1.3: Stress-strain relation of solid, liquid and linear viscoelastic materials
Figure 1.4: Working principle of a static mode biosensor
Figure 1.5: Working principle of a dynamic mode mechanical mass sensor
Figure 1.6: Schematic of Quartz Crystal Microbalance (QCM).
Figure 1.7: Schematic of a Surface Acoustic
Figure 1.8: 3-D representation of a suspended microchannel resonator (SMR) [57]10
Figure 1.9: Sensing principle of suspended microchannel resonators
Figure 1.10: Schematic and working principle of the devices implemented for evaluation of cell deformability
[60]
Figure 1.11: Drawing of the 3-channel configuration used for cell density evaluation with SMRs [61]12
Figure 2.1: Schematic (a) and working principle (b) of the device developed during this PhD thesis18
Figure 2.2: Microfluidic channels span different cantilever lengths in order to disentangle analyte mass and
stiffness contribution. Stiffening structures are distributed around the clamp to provide structura
support
Figure 2.3: Design and dimensions of low-stress silicon nitride SMR array21
Figure 2.4: Microfluidic and resonator design23
Figure 2.5: Microfluidic–electrical analogy for a portion of the design SMR network25
Figure 2.6: Overview of piezoelectric electrodes pattern
Figure 2.7: (top image): Piezoelectric electrodes integrated on 250 μm- and 500 μm- long SMRs27
Figure 2.8: Study of PZE electrodes thickness and length via FEM simulations28
Figure 2.9: Butterworth-Van Dyke (BVD) electrical equivalent circuit of PZE-transduced resonator [71]28
Figure 2.10: Layout of electrical test structures30
Figure 2.11: Full wafer layout31
Figure 2.12: Chip designs included in the wafer31
Figure 3.1: 2-way coupled fluid-structure interaction
Figure 3.2: Normalized quality factor $Feta$ as a function of Reynolds number eta in case of incompressible (a) and
compressible (b) fluid38
Figure 3.3: Simulated 3-D geometry40

Figure 3.4: Mesh of solid and fluid domain	40
Figure 3.5: First eigenmode of a 2-D simulated geometry.	40
Figure 3.6: First eigenmode of 3-D simulated Device B (symmetry exploited).	40
Figure 3.7: Numerical model results	42
Figure 3.8: Numerical model: result for on-axis case, incompressible fluids.	42
Figure 3.9: Examples of dynamic viscosity values.	43
Figure 4.1: SMR sensors obtained from a process flow based on the wet etching of a sacrificial material	48
Figure 4.2: Examples of SMR fabricated without the use of a deposited sacrificial material.	49
Figure 4.3 First part of SMR process flow, in cross section (not in scale).	51
Figure 4.4: Optical microscope image of the result of first e-beam lithography (EBL1).	52
Figure 4.5: Comparison between trenches defined via continuous (top row) and pulsed dry etching (bot	ttom
row) [66]	53
Figure 4.6: SEM image of a trench pattern etched through polysilicon (top view).	54
Figure 4.7: SEM image of a trench cross section before resist strip in oxygen plasma	54
Figure 4.8: Bosch ® process optimization: example of trench underetching (a) and overetching (b)	54
Figure 4.9: Microfluidic channel fabricated via trench technology and filled with sacrificial PolySi	54
Figure 4.10: Schematic of the process flow for fluidic openings from the wafer backside (not in scale)	55
Figure 4.11: Squared 550 $\mu m \times$ 550 μm inlet, designed in the first generation of devices	55
Figure 4.12: KOH etching of a <100> - oriented silicon wafer.	56
Figure 4.13: Suspended microfluidic channel filled with PolySi, after 5 hours of anisotropic etching in KOH	I56
Figure 4.14:Optical image of the backside of a wafer before channel emptying	57
Figure 4.15: Collection of optical microscope images showing a Complete Chip design, first generation	58
Figure 4.16: Fluidic openings from the top of the wafer can be defined with one lithographic and one	dry
etching step (a), followed by the long wet etching in KOH for channel emptying (b)	59
Figure 4.17: Wafer after 24 h KOH, with the top surface exposed to the etching	59
Figure 4.18: Channel emptying from the top of the wafer is achieved defining dashed-line apertures along	g the
channel length	60
Figure 4.19: SEM image of microfluidic channel, showing the geometry of the dashed apertures, defined	d via
the second e-beam lithography (EBL2).	61
Figure 4.20: Example of nitride membrane break due to the inefficient distribution of etch apertures	61
Figure 4.21: Wafer conditions after channel emptying via top apertures.	61
Figure 4.22: Results of channel emptying from the top through etch apertures.	61
Figure 4.23: Cross section of a cleaved wafer, showing two u-shaped microfluidic channels below the	flat
surface of the wafer	62
Figure 4.24: During the filling of EBL2 etch apertures via LPCVD process, Is-SiNx is also deposited in the in	ıside
of the fluidic channel.	63
Figure 4.25: SEM inspection of EBL2 etch apertures, after Is-SiNx deposition	63
Figure 4.26: 300 nm top Is-SiNx does not confer enough robustness to the inlet membrane to survive the	кон
etching	63

Figure 4.27: SEM inspection of a Is-SiNx filled aperture at SEM, after nitride thin-down in IBE etching6
Figure 4.28: Process flow for PZE electrodes fabrication on top of embedded fluidic channels6
Figure 4.29: Comparison between a Pt layer patterned without (a) and with (b) the protective SiO_2 layer 6
Figure 4.30: Bottom and top layers after development.
Figure 4.31: First and second generation of top and bottom electrode design6
Figure 4.32: Top layers smoothly stepping on the bottom layers
Figure 4.33: Fence resulting from Pt etching in chlorine chemistry.
Figure 4.34: Polysilicon islands defined below adjacent tracks, to limit electrical coupling through the
conductive sacrificial layer6
Figure 4.35: Final steps of SMR process flow to release the hollow resonators.
Figure 4.36: Optical images of devices at two different stages of the release process
Figure 4.37: SEM image of two released cantilevers, 250 μ m- and 500 μ m-long
Figure 4.38: Fluidic inlets opened during the release process
Figure 4.39: Residues of passivation layer on the sides of a resonator, after release and resist strip79
Figure 4.40: Fabricated SMRs with integrated PZE transduction
Figure 4.41: Fabricated doubly-clamped SMRs with integrated PZE transduction7
Figure 5.1: Schematic of the fluidic interface
Figure 5.2: 3-D drawing of developed fluidic connector [106]
Figure 5.3: Fluidic connector with bypass channels.
Figure 5.4: Flip-lock connectors from Hirose (HRS, FH12 Series)
Figure 5.5: Schematic drawing of a chip assembled with fluidic connector and custom PCB (top view)7
Figure 5.6: Picture of the experimental platform integrating fluidic and electrical connections8
Figure 5.7. Complete experimental platform including fluidic interface, electrical connection and temperature
control [107]8
Figure 5.8: Measuement setup for SMR characterization in air
Figure 6.1: Comparison between actuation via piezo-shaker (a) and PZE electrodes (b) for a doubly-clampe
SMR, empty in air, for 1.5 V driving voltage8
Figure 6.2: Mechanical response of a 250 μm-long SMR, in air environment
Figure 6.3: FEM model for analysis of PZE actuation8
Figure 6.4: Equivalent circuit representing the balanced bridging technique (blue branch), implemented t
balance parasitic reactances
Figure 6.5: Measurement of a fully PZE-transduced 500 μ m-long SMR before (a) and after (b) balancing the
parasitic current, in air8
Figure 6.6: Electrical tracks on chip
Figure 6.7: 250 μ m-long SMR (a,b,c) and 500 μ m-long SMR (d,e,f) characterization with different fluids9
Figure 6.8: Resonance frequency and quality factor as a function of applied fluidic flow for SMR-250 μm and
SMR-500 μm, filled with DI water, at room temperature and ambient pressure9
Figure 6.9: Experimental fluidic resistance Rf of a 4-Cantilever chip (short side) filled with water at 25°C, a
ambient pressure9

Figure 6.10: Frequency and quality factor as a function of temperature, for an empty 250 μ m-long SMR, in air.
96
Figure 6.11: Frequency and quality factor as a function of temperature, for a water-filled 250 μm -long SMR, in
air
Figure 6.12: Responsivity and frequency noise contributions to the monitored frequency signal97
Figure 6.13: Schematic of the Phase locked loop (PLL) for measurement of SMR frequency stability98
Figure 6.14: Example of Allan deviation plot as a function of the integration time (blue solid line)99
Figure 6.15: Frequency stability of 250 μ m-long (a) and 500 μ m-long (b) SMR, in air environment101
Figure 6.16: Quality factor extracted from the first resonant mode of four empty SMR sensors as a function of
external pressure
Figure 6.17: Example of noise (PSD) measurement obtained from a 250 μ m-long SMR, water-filled in air 102 μ m-long SMR, water-filled in air
Figure 6.18: Relative variations of TMN peak, frequency stability at 200 ms (inverse) and quality factor (square
root), with respect to the case of empty devices in air, for the 250 μ m-long SMR of Figure 6.19 103
Figure 6.19: Frequency stability (solid lines) of a 250 μ m-long SMR measured at $x=L$, resulting from ~800 mV
detected signals
Figure 6.20: Relative variations of TMN peak, frequency stability at 200 ms (inverse) and quality factor (square
root), with respect to the case of empty devices in air, for the 500 μ m-long SMR of Figure 6.21 103
Figure 6.21: Frequency stability (solid lines) of a 500 μ m-long SMR measured at $x=L$, resulting from ~800 mV
detected signals
Figure 6.22: Allan Deviation is measured focusing the LDV laser on three different spots along the resonator
length104
Figure 6.23: Allan deviation dependence on laser position along cantilever x and driving voltage $Vdrive$, for
a water-filled 250 μm long-SMR, in air (a) and vacuum (b) environment105
Figure 6.24: To estimate particle residence time at tip, a channel length of 50 μm is considered, shown by the
white arrow in the inset
Figure 6.25: SEM image of SMR inlet, after pushing beads into the embedded channel
Figure 6.26: Schematic of current fluidic inlet configuration, in cross section (side view)
Figure 6.27: Proposed inlet configuration for particle detection via SMRs, in cross section (side view) 107

List of Tables

Table 1.1: Typical ranges of few rheology measurement techniques reported in literature [17, 20-22].
Table 1.2: Common transduction techniques for mechanical sensors at the microscale. 13
Table 2.1: Typical values of density and Young's modulus for cells and low-stress silicon nitride19
Table 2.2: SMR parameters estimated from design.
Table 2.3: Motional parameters calculated for an empty 250 μ m-long SMR, assuming $ extit{ extit{Q}} = 50029$
Table 3.1: Geometrical properties of simulated devices [74]. 39
Table 3.2: Fluidic properties and corresponding Reynolds numbers used for numerical simulations43
Table 4.1: Etching rates and chemistry used for Is-SiNx and PolySi dry etching at Alcatel 601E55
Table 4.2: Measured etching rates of ls-SiNx, amorphous silicon (hard mask) and ZEP resist in Nitrure_1 etching.
60
Fable 4.3: Deposition parameter at Pfeiffer Spider 600, for AlN, Pt and SiO₂64
Fable 4.4: Etching parameters at STS Multiplex ICP for AIN, Pt and SiO₂ etching65
Table 4.5: Detailed parameters for SMR release at AMS 200 SE68
Table 5.1: Minimum pulsation-free flows achievable with different syringes operated by neMESYS fluidic
pump
Fable 6.1: Comparison between measured and simulated PZE actuation efficiencies in DC87
Table 6.2: Calculated feedthrough capacitance ${\it Cf}$ and parasitic capacitance ${\it C0}$ (single finger), with relative
electrode areas89
Table 6.3: Average values of measured resonance frequencies and quality factors of empty SMRs, full-channel
length, in air and in vacuum environment91
Table 6.4: Measured mass responsivities of SMR devices
Table 6.5: Experimental and analytical values of fluidic resistance of a 4-Cantilever chip, filled with water at
25°C94
Table 6.6: Noise characterization and quality factors of a 250 μ m- and a 500 μ m-long SMR, for four different
experimental conditions103

List of Abbreviations

SMR	Suspended Microchannel Resonators
MEMS	Microelectromechanical systems
NEMS	Nanoelectromechanical systems
AFM	Atomic force microscopy
CTC	Circulating tumor cells
FDA	Food and Drug Administration
EpCAM	Epithelial cell adhesion molecule
RBC	Red blood cells
VPT	Video particle tracking
DWS	Diffusing wave spectroscopy
SAW	Surface acoustic waves
BAW	Bulk acoustic waves
QCM	Quartz crystal microbalance
PZE	Piezoelectric
PCB	Printed Circuit Board
XRD	X-ray diffraction
FEM	Finite Element Modeling
ALE	Arbitrary Lagrangian to Eulerian transformation
FSI	Fluid-Structure Interaction
PID	Proportional-integral-derivative
SON	Silicon-On-Nothing
SEM	Scanning Electron Microscope
IBE	Ion Beam Etching
EPD	End Point Detection
ICP	Inductively Coupled Plasma
IPA	Isopropyl alcohol
DI water	Deionized water
SNR	Signal-to-Noise Ratio
TMN	Thermomechanical Noise
AD	Allan Deviation
FFT	Fast Fourier Transform

Contributions

Researcher	Position*	Contribution		
Luis Guillermo Villanueva	Professor	Supervisor		
Edit Guinerine vindideva	110103501	Matlab code for Allan Deviation		
Tom Larsen	Postdoc	Measurement protocols		
Kaitlin Howell	PhD student	XRD measurements in Chapter 4		
Damien Maillard	Master student / PhD student	 Fluidic interface in Chapter 5 Temperature measurements in Chapter 6 Fluidic resistance measurements in Chapter 6 Abstract translation in French 		
Andrea Gerbino	Master student	COMSOL simulations in Chapter 3		

^{*}Position of the researcher at the time of his/her contribution to this project.

Chapter 1 INTRODUCTION

This chapter presents the motivation behind this PhD project. A brief introduction to the scientific field and relevant prior research are described. At the end, an outline of the thesis is given.

1.1 Motivation

1.1.1 Cell Mechanical Properties

The importance of the link between cell mechanics and human diseases is becoming increasingly evident. For instance, the deformability of red blood cells (RBC) has been correlated to several diseases such as metabolic disorders, malaria and sickle cell anemia [1-3].

Furthermore, there is an accumulation of data in the last two decades that points out to the mechanical properties of cells as a reliable indicator of transformation into cancerous or metastatic cells: several studies have shown that a reduction in *stiffness* corresponds to increasing metastatic potential in human cancer cell lines, using several different *in vitro* biomechanical assays [4].

A breakthrough was made by Prof. Gimzewski's group, who introduced for the first time *ex vivo* stiffness probing via atomic force microscopy (AFM). Within the same sample, they found that the cell stiffness of metastatic cancer cells, isolated from the pleural fluid of human patients, is more than 70% softer than the benign cells. Their work shows that mechanical analysis can distinguish cancerous cells from normal ones even when they have similar shapes and sizes [5, 6]. However, the relevance of single cell measurements has been questioned due to the lack of three dimensional tissue environment. It is indeed known that cell mechanics is affected by the characteristics of the surrounding medium.

A valid answer to this issue was given few years later by Prof. Roderick Lim's group, who found a correlation between stiffness and stage of cancer, using *surgical biopsies* from real human patients (*in vivo*) [7]. The conclusion of this work was that: (i) even if tumors are stiffer than health tissues, cancer cells are more deformable than normal cells, and (ii) cancer cells deformability correlates with increased metastatic potential.

In addition, a study from Prof. San Paulo and coworkers from 2016 reported that the mechanical response of both healthy and cancer cells is *frequency dependent*, demonstrating the *viscoelastic nature of cells*. The Young's modulus of healthy and breast cancer cells was measured via AFM: increasing the frequency of the measurements from 1 Hz to 250 Hz, the Young's moduli values increased by about two orders of magnitude [8].

Such impressive results encouraged developments in cell mechanics research through the study of new dedicated sensor applications.

1.1.1.1 CANCER RESEARCH: CTCs

For most cancers, molecular analysis are typically performed on tissue acquired through a *surgical biopsy* at diagnosis. However, not all cancer tissues are easily accessible for sample extraction. In addition, monitoring how the tumor responds to therapies or naturally mutates over time is quite difficult due to the invasiveness of the surgical procedure.

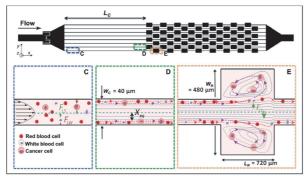
Liquid biopsy constitutes an outstanding alternative to standard surgical techniques, as it enables the tumor genetic profiling directly from body fluids (blood, saliva, urine, etc.) [9]. This cost-effective and minimally-invasive approach allows to easily and regularly repeat biofluid sampling in order to monitor disease mutations over time and responsivity to drugs and treatments, opening key opportunities for personalized medicine.

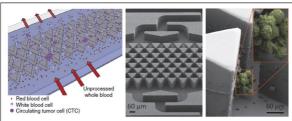
Liquid biopsy features different types of biomarkers such as circulating tumor cells (CTCs), cell-free DNA (cfDNA) and exosomes (extracellular nano-vesicles).

In particular, *circulating tumor cell* (CTCs) are cells that detach from their primary tumor and enter blood or lymphatic vessels. Malignant CTCs can subsequently invade and proliferate in tissues far from their primary tumor, and generate metastasis in the body, which are the main cause of death among cancer patients [10]. Detecting and analyzing CTCs has the potential to improve the diagnosis process, understand the tumor genesis and develop personalized treatments. However, these cells, between 15 and 25 µm in diameter, are extremely rare (between 1 to 10 CTCs per ml of blood) [9].

For this reason, in the last 70 years several technologies have been developed to isolate them on the base of their biological and physical properties. The only FDA-approved clinical device is the CellSearch by Veridex: this chip counts the CTC cells from peripheral blood using magnetic immunotargeting of a membrane protein (epithelial cell adhesion molecule, EpCAM) and fluorescence labeling [11]. Figure 1.1 shows few examples of microfluidic devices developed for CTC isolation based on their physical properties (typically size-based), label-free and in general simpler and faster than bio-targeting techniques.

After isolation, the study of CTCs mechanical properties like size, mass and stiffness is fundamental to understand the process of differentiation from the cell of origin and metastasis formation. In particular, their enhanced deformability (reduced stiffness) is the key element that allows these cells to detach from their primary tumor and breach through tissues and vessels. For example, in a study recently conducted by Prof. Toner's group, CTC aggregates (clusters) of up to 20 cells (between 15 and 25 μ m in diameter) successfully traversed capillaries as small as 5μ m in diameter with over 90% efficiency, as shown in Figure 1.2 [12]. The study demonstrates the ability of CTC clusters to transit through narrow vessels, thanks to their capacity to rapidly and reversibly unfold into highly deformable single-cell chains.





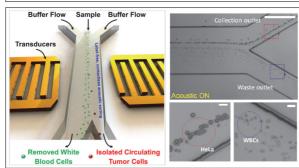


Figure 1.1: Few examples of microfluidic chips for CTC isolation based on their mechanical properties.

(Top): Vortex Chip developed by Prof. Di Carlo's group [13]. They combine the use of micro-scale vortices and inertial focusing to extract CTCs from whole blood samples, demonstrating healthy cell recovery and label-free application. Upon entrance in the wider sector of the channel, larger particles (CTCs) will experience a stronger divergent force, being pushed away from the main flow and into the vortices. Capture efficiency depends on cell size, density and compressibility. (Figure readapted with permission from Lab on a Chip, ref. [13].)

(Centre): Cluster Chip developed by Prof. Toner's group [14]. The device enables size-based, label-free isolation of CTC clusters from unprocessed whole-blood from patients with cancer. Triangular pillars funnel and trap CTC aggregates based on their size and on dynamic balance of frictional and viscous forces, while single blood cells pass through. (Figure readapted with permission from Nature Methods, ref. [14].)

(Bottom): First device for acoustic-based separation of CTCs from clinical blood samples, developed by Prof. Huang's group [15]. This technology is based on tilted-angle standing surface acoustic waves (taSSAW), which induce an acoustic force on flowing particles. Larger CTCs experience larger acoustic forces and are subjected to larger lateral displacement, being separated from the blood flow and collected at a specific outlet. This separation method is label-free, contactless and preserves cell viability. Scale bars: 30µm. (Figure readapted from PNAS, ref. [15].)

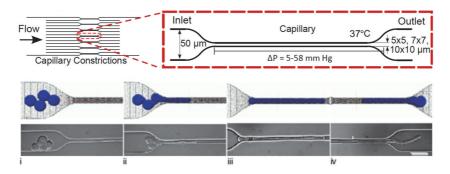


Figure 1.2: Schematic of the microfluidic device used by Prof. Toner's group (top), computational simulation (centre) and optical pictures (bottom). CTCs clusters of up to 20 cells isolated from melanoma patients travel through a 5 μm capillary constriction, under physiological conditions (temperature and pressure). This demonstrates their ability to unfold into single-cell chain and deform accordingly to the channel dimension, comparable to human capillaries. Scale bar: 50μm. (Figure readapted from PNAS [12].)

1.1.2 Rheology of complex fluids

Rheology is the study of the elastic and viscous properties of a fluid. Most biological fluids are complex (viscoelastic): they simultaneously exhibit solid (completely elastic) and fluid (completely viscous) behavior, therefore they may contain both elastic and viscous non-linearities (Figure 1.3). Also cells are viscoelastic media, and their mechanical properties are time and load dependent. For instance, viscoelasticity allows RBC to rapidly

increase their deformability in order to flow through narrow blood vessels or tissues [1]. Particular interest is thus found in rheology of complex biofluids, as this can give an insight of physiological flows [16]. Complex fluids are also present in several industrial applications (paints, shampoos, colloids, gels and foams) such as liquid crystal displays, inkjet printers, lubrication flows and heat sinks [17]. Engineered materials as hydrogels [18] or ionic liquids [19], which have been used in microfluidic systems for several years, are another example of viscoelastic materials.

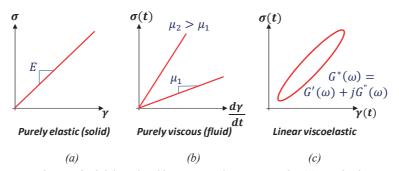


Figure 1.3: Stress-strain relation of solid, liquid and linear viscoelastic materials. (a) Purely elastic materials exhibit linear relation between stress and strain, characterized by the Young's modulus E, according to Hooke's law. (b) Newton's law describes the linear behavior between stress and strain rates, defined by the fluid dynamic viscosity μ and typical of liquids. (c) Linear viscoelastic fluids simultaneously exhibit solid-like and liquid-like behavior. They are described by the complex viscoelastic modulus G^* , given by the sum of the elastic and viscous moduli G' and G'', respectively).

Among the classical tools used to characterize the rheology of complex fluids, rheometers are able to extract both elastic and viscous components by applying a shear stress or an extensional stress to the fluidic sample. However, rheometers cannot perform in-situ measurements, but rather use macroscopic fluidic samples (in the order of milliliters) and are restricted to the low frequency range (less than 200 Hz), due to inertial limitations. Since the mechanical properties of complex fluids depend on the applied load, in order to provide full characterization of the material, it is fundamental to span the largest possible range of frequencies.

To overcome the volume and frequency range limitations, some alternative methods have been developed over the last century, giving rise to the field of *microrheology*. Microrheology enables in-situ measurement of microfluidic samples, typically dispersing micron-sized particles inside the fluidic volume and tracking or sensing their movement. Active measurement methods as optical or magnetic tweezers and AFM, can be distinguished from passive measurements methods based on recording the Brownian motion of dispersed particles, via video particle tracking (VPT) or diffusing wave spectroscopy (DWS) [20].

One of the best achievements in terms of higher frequency range and smaller sample volumes is given by *microcantilevers* immersed in the sample liquid. Dufour's group linked the damped cantilever motion to the rheological properties of the fluid, achieving hundreds of kHz and using less than 100µl sample volume [21].

Some examples of macro and micro-rheology typical ranges of frequency and volumes are shown in Table 1.1.

	Frequency range [Hz]	Sample Volume [µl]	Viscoelastic Modulus [Pa]
MECHANICAL			
Rotational rheometers	$< 10^{2}$	> 104	$1 - 10^2$
AFM	1 - 104	<< 1	10 ³ - 10 ⁹
Vibrating microcantilevers	$10^3 - 10^5$	10 - 10 ²	1 - 10 ⁵
OPTICAL			
DWS	10 - 10 ⁵	$> 10^2$	10 ⁻¹ - 10 ⁴
VPT	10-2 - 50	~ 10	10 ⁻⁵ - 1
Optical Tweezers	10 ⁻¹ - 10 ⁵	> 10	10 ⁻² - 10 ³

Table 1.1: Typical ranges of few rheology measurement techniques reported in literature [17, 20-22].

1.2 Mechanical Biosensors

Micro- and Nano- mechanical biosensors are mechanical transducers with micro- and nano- sized moving parts. Their fabrication relies on standard semiconductor processing techniques, enabling for efficient batch production. Nanomechanical biosensors are usually cantilever-shaped, but can also include doubly-clamped beams, membranes, and SAW or BAW (bulk acoustic waves) devices.

Robust and well-established electrical and optical sensors still dominate the field of biological detection in terms of market share. However, in the past two decades Micro- and Nano- Mechanical systems (N/MEMS) have been receiving a lot of attention at the research level. The main reason for this development of N/MEMS in life-science applications (BioMEMS) has been to address the *mechanical nature* of many fundamental biological processes. A clear example is cell mechanical properties such as stiffness or viscoelasticity, which represent a valid diagnostic biomarker for several pathologies like cancer, malaria and sickle cell anemia, among others [2, 23]. In addition, continuous advances in micro- and nano-fabrication techniques allow the size of mechanical devices to be comparable to the size of some biomolecules, thus resulting in a highly sensitive *mechanical response* and in outstanding *mass resolution* [24-26]. Furthermore, N/MEMS can exhibit extremely high *mechanical compliance*. This enables the measurement of pN forces generated by biological interactions, by translating them into a mechanical displacement, enhancing *force responsivity* [27, 28].

Mechanical biosensors can operate in *static* or *dynamic* mode, depending on whether quasi-static deflection or shifts in the resonance frequency are monitored and thus related to the biological event under study.

1.2.1 Static mode biosensors

Static-mode biosensors are usually cantilever shaped and typically measure surface stress or surface forces induced by biological entities such as single-base DNA, pathogens or protein biomarkers [29, 30]. Other approaches consider the detection of forces at the tip of cantilevers, using a configuration similar to that of an atomic force microscope (AFM) [31, 32].

Common surface stress biosensors consist of microcantilevers with one active side functionalized to attach a monolayer of receptors that exhibit high affinity to the target molecules, while the opposite passive side is inert. The devices are placed in a fluid cell where the sample solution is delivered. The binding of target molecules to the receptors causes a surface stress change that induces a quasi-static deflection of the cantilever.



Figure 1.4: Working principle of a static mode biosensor. Binding of target molecules induces a surface stress, which leads to a quasi-static deflection of the cantilever. This bending can be measured with optical or electrical displacement detection methods.

The stress-induced cantilever deflection is monitored in real-time via optical or electrical displacement detection methods. The surface stress variation can be evaluated through the change of curvature the microcantilevers undergo when the sample solution flows over them. According to the Stoney's equation $\Delta \kappa = 6 \frac{(1-\nu)h_f}{Eh_c^2} \Delta \sigma$, where κ is the curvature, ν and E the Posson's ratio and the Young's modulus of the material respectively, h_c the thickness of the cantilever, h_f the thickness of the film constituted by molecules binding on the cantilever, and $\Delta \sigma$ the surface stress change [33, 34].

These devices have shown remarkable label-free capabilities [35], however deflection is highly susceptible to non-specific binding, temperature and flow fluctuations. Very stable flows, together with differential measurements of non-functionalized cantilever help to partially circumvent spurious deflections [30].

1.2.2 Dynamic mode biosensors

Dynamic mode biosensors are mechanical devices which vibrate close to their resonance frequency f_r , which is proportional to the square root of the ratio between effective stiffness k and effective mass m of the structure. An analyte landing or binding on the resonator surface induces a change of its mass (and stiffness [36]), which is transduced into a shift of the resonance frequency, as seen in Figure 1.5.

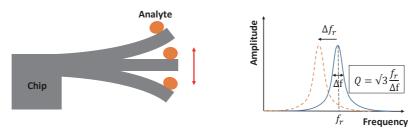


Figure 1.5: Working principle of a dynamic mode mechanical mass sensor. An analyte landing on the free-end surface of a singly-clamped beam resonator induces a change of its mass and stiffness, which is transduced into a shift of the resonance frequency Δf_r . The accuracy of the measurement of the resonance frequency is defined by the quality factor Q, related to the full width of the half maximum of the resonant peak Δf .

Micro- and Nano- mechanical resonators have demonstrated great capabilities in life-science label-free mass sensing applications, such as detection of viruses and single molecules [26, 37, 38].

Mass responsivity is defined as the change in resonance frequency due to a change in mass, calculated as in Eq. 1.1 [37, 39]:

$$\Re = \frac{\partial f_r}{\partial m} \approx -\frac{1}{2} \frac{f_r}{m}$$
 Eq. 1.1

In order to achieve the highest mass responsivity, one can reduce the mass or increase the frequency (or both).

The minimum detectable mass by a mechanical resonator is given by the ratio between the frequency noise and the responsivity, and it is typically given by [40]:

$$\delta m_{min} \approx \frac{\delta f_{min}}{\Re} = -2 \ m \frac{\delta f_{min}}{f_r} \approx -2 \ m \frac{1}{Q} \frac{Noise}{Signal}$$
 Eq. 1.2

From Eq. 1.2, it is clear that a large quality factor Q is required to maximize the sensing performance. Q determines the slope of the phase vs. frequency curve of the device near resonance. It can also be seen as the ratio between energy stored and energy lost per cycle of the resonator: $Q = 2\pi \frac{E_{stored}}{E_{lost}}$.

In order to attain large quality factors, energy losses need to be reduced. This typically implies to work in vacuum [29]. However, when tackling real time biosensing applications, like protein or DNA detection, the immersion of the resonator into fluids is inevitable since most biological processes naturally occur in a *fluidic environment*. In this scenario, fluid viscous damping causes a drop of *Q* of several orders of magnitude [41].

1.2.2.1 DETECTION IN LIQUIDS

The main strategies developed to exploit nanomechanical sensor performances for biological detection consist in (i) capture in fluidic phase and detection in vacuum, (ii) measurements in humid environment, and (iii) continuous operations in liquid focused on enhancing the quality factor [29, 30]. The first one will not be detailed here as the operation of the device is not performed in liquid.

Humid environment

Certain biological species like bacteria can grow and survive in humid environment. In this case, even though viscous damping is larger than in vacuum, it does not reach the levels of full immersion in liquid, thus the quality factor remains acceptable. An example of this biodetection is the growth monitoring of Escherichia coli using cantilevers coated with nutritive layers (sugar) and operation in air with 100% humidity [42].

Real-Time monitoring in liquid

There are many other cases, e.g. the detection of analytes, which require full fluidic immersion while the measurement is running. This, as announced before, poses a practical issue since viscous damping degrades Q. The solution for this has been, up to date, limited to a handful of experimental techniques. One example is the use of acoustic modes (QCM and SAW) [43, 44]. Another option, considering flexural devices, is to use higher vibrational modes (larger frequencies) [45], vertical nanopillars [46-48] and suspended microchannel resonators [49].

1.2.2.2 QUARTZ CRYSTAL MICROBALANCE

An interesting device from the performance point of view is the quartz crystal microbalance (QCM). It consists of a quartz disc with electrodes that allow for the excitation of a shear acoustic mode, which has an inherent low viscous interaction with the surrounding fluid (Figure 1.6) [50]. QCMs are used nowadays in a range of scientific disciplines, such as chemistry, biology, and material sciences, and demonstrated detection of biomolecules and bacteria [43]. The resonance frequencies of these devices are usually in the range of 10-50 MHz, and are determined by the thickness of the crystal. Because of the typical device thickness in the range of millimeters, the sensitivity of QCM is limited by its mass [43]. At higher frequencies the devices become very thin

and too fragile. The lowest limit of detection of QCM in liquid has been achieved in the work by Cho and coworkers [51]. They demonstrated nanomolar sensitivity for continuous analyte monitoring of C-reactive protein, a biomarker for coronary heart disease, using an indirect-competitive assay.

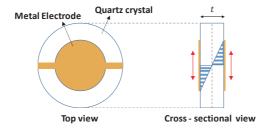


Figure 1.6: Schematic of Quartz Crystal Microbalance (QCM). A quartz crystal disk oscillates in thickness-shear mode when the metal electrodes deposited on each side of the disk are connected to an alternate voltage signal, generating a bulk shear acoustic wave (BAW).

1.2.2.3 SURFACE ACOUSTIC WAVE DEVICES

Another example of acoustic sensors are SAW devices, which demonstrated their capabilities in microfluidic actuation and micro-objects manipulation like mixing, pumping, merging and sorting among other applications [52].

SAW devices generate and detect acoustic waves using interdigital transducers (IDT) on the surface of a piezoelectric crystal, typically lithium niobate (LiNbO3) or lithium tantalate (LiTaO3). As shown in Figure 1.7, an input IDT converts an electrical signal into an acoustic wave through direct piezoelectric effect. On the opposite side, an output IDT converts the acoustic wave back into an electrical signal, through inverse piezoelectric effect. The surface acoustic wave travels along the space between the IDTs, known as the delay-line. The acoustic energy stays confined close to the surface of the PZE crystal in a depth range close to the acoustic wavelength, regardless of the thickness of the complete substrate. For this reason, the wave is potentially very sensitive towards any change on the surface, such as mass loading, viscosity and conductivity changes [44].

To permit the use of a SAW device as a biosensor, analyte-specific molecules are immobilized on the device surface to catch analyte molecules from the sample solution, as shown in Figure 1.7. Analytes binding to the immobilized receptor molecules will modulate the velocity of the SAW and hence the output signal measured by the system electronics. [44].

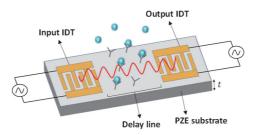


Figure 1.7: Schematic of a Surface Acoustic Wave sensor (SAW). An input interdigitated electrode (IDT) sitting on a piezoelectric substrate converts an electrical signal into an acoustic wave. An output IDT converts the acoustic wave back into an electrical signal. The surface acoustic wave travels along the space between the IDTs, known as the delay-line. Analytes binding to the immobilized receptors will modulate the velocity of the SAW and hence the output signal measured by the system electronics.

SAW devices represent a cost-effective technology for label-free detection of biomolecular interactions, allowing highly sensitive real-time detection of biomolecules such as DNA, protein and bacteria [44, 53]. Recently, Senvely and coworkers proposed a low cost innovative system capable of analyzing few picoliters of biological cell samples at high frequencies [54]. Tumor cells are trapped inside microcavities along the SAW device surface. Through interaction with the samples, the resultant SAW reaching the output electrode exhibits a phase delay which is related to the cell mechanical stiffness.

SAW devices can be as thin as few hundreds of micrometers and their typical frequencies are much larger than those of QCMs. However, the acoustic waves are not purely shear, and thus radiate compression waves into the liquid, which induces larger damping than in the case of shear modes, but lower than in the case of flexural [53].

1.3 Suspended microchannel resonators: state of the art

As discussed in paragraph 1.2.2, the minimum detectable mass that a resonator is able to measure is proportional to the mass of the device itself. In order to minimize said parameter, the optimum choice is to work with *flexural devices*, which can reach nanoscale dimensions and masses in the order of picograms, potentially allowing single molecule mass sensitivities. However, flexural devices exhibit out-of-plane vibrations, therefore their energy loss when they vibrate in a fluid environment is much larger compared to acoustic resonators.

An important contribution to mechanical biosensing in liquids came from Scott Manalis' group in 2003 [49], when they presented a device inspired from the millimeter scale densitometer developed by Stabinger and co-workers in 1967 [55]. *Suspended microchannel resonators* (SMRs), shown in Figure 1.8, are resonant mass sensors for continuous biomolecular detection in a pico-liter fluid volume.

SMRs consist of a hollow resonant containing embedded microfluidic structure channels. The fluid to be analyzed flows inside the resonator, thus viscous damping is almost completely suppressed, and mass loading is minimized. Real time analysis of fluidic samples is made possible while the whole device can be kept in dry environment, thus retaining high mechanical performances. Quality factors up to 15000 and mass sensitivities down to 1 attogram in 1 kHz bandwidth have been demonstrated [56]. One of the major challenges of these devices is the costly and rather challenging fabrication, involving several process steps, which also include the use of aggressive chemicals.

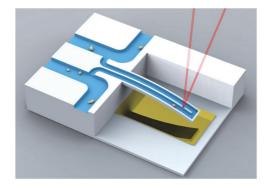


Figure 1.8: 3-D representation of a suspended microchannel resonator (SMR) [57]. A u-shaped microfluidic channel runs through a cantilever sensor. Real time mass detection is achieved by monitoring the resonance frequency over time, as diluted particles flow inside the resonator. Electrostatic actuation and optical detection are among the most typical transduction strategies for these devices.

Two modalities of operation are possible with SMRs devices: flow-through detection and affinity-based capture, shown in Figure 1.9.

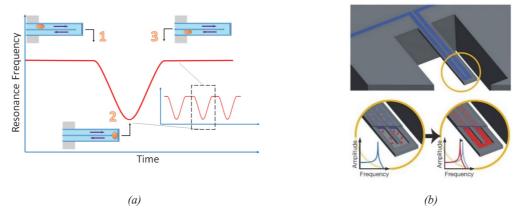


Figure 1.9: Sensing principle of suspended microchannel resonators. (a) Flow-through detection: a particle flowing inside the embedded microfluidic channel induces a shift in the resonance frequency of the device which is related to the particle mass and position along the structure. (b) Affinity-based capture: target analytes are captured by molecular recognition on a bio-functionalized surface of the device. This induces a shift in the resonance frequency due to mass loading effect. (Figure readapted with permission from Nature, ref. [56].)

In the *flow-through detection method* a particle travelling inside the microfluidic channel induces a shift in the resonance frequency of the device which is a function of the position of the particle along the resonating structure, and of the particle buoyant mass (particle mass minus mass of the displaced fluid). This approach has been mainly used to study the development of cells along time as a function of different conditions. In this case, the maximum flow rate is determined by the *minimum particle residence time*, which yields sufficient averaging to achieve a detectable signal above the noise floor.

In the *affinity-based capture method* target analytes are immobilized by molecular recognition on the biofunctionalized surface of the microfluidic channel. The functionalization can provide high specificity of capture, reducing false positives that can be caused by particles with similar masses. In this case, the added mass signal from immobilized target analytes can be averaged over a period of time longer than that of free-particle transit through the microchannel. Therefore, in contrast with the flow-through detection method, affinity-capture based SMRs devices are not limited by the analyte minimum residence time. Instead, the sensitivity is determined by the kinetics of diffusion and binding, which can be controlled through geometry and flow-rate.

The main limitation of this type of devices is the *throughput*, defined as the sample volume that can be analyzed per unit of time [58]. High throughputs can be obtained through pre-concentration of the analyte solution and device parallelization, as recently demonstrated by Cermak and co-workers [59].

1.3.1 Applications

SMRs have been successfully employed for several biosensing applications. In particular, measuring the travel time of the particles through an embedded constriction inside the buried channel *deformability* was assessed (Figure 1.10) [60]; to quantify *mass density*, mechanical traps and a three-channel-SMR enabled measurements of the buoyant mass of each particle in two fluids of different densities (Figure 1.11) [61]. *Mass* evaluation is performed in the default configuration, by monitoring the shift in resonance frequency induced by the particle flowing through the channel (Figure 1.9(a)). In addition, knowing these quantities allows to calculate the size

(*volume*) of the particles. High-throughput measurement of *cell growth* was also demonstrated by weighing the cell with multiple SMRs arranged in array configuration and separated by delay channels, which provide the cell time to grow between one cantilever sensor and the following [62].

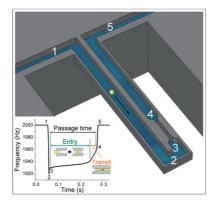


Figure 1.10: Schematic and working principle of the devices implemented for evaluation of cell deformability [60]. Deformability is dependent on the particle entry velocity in the microchannel constriction. Cell surface friction is dependent on the transit velocity in the narrower channel. (Figure readapted from PNAS, ref. [60].)

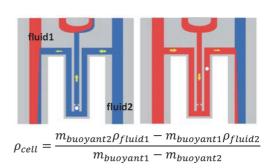


Figure 1.11: Drawing of the 3-channel configuration used for cell density evaluation with SMRs [61]. The particle is immobilized with a mechanical trap; a quick exchange of the surrounding fluid allows comparing the buoyant mass (particle mass minus mass of the displaced fluid) in two fluids with different densities. (Figure readapted with permission from Lab on a Chip, ref. [61].)

SMRs have also been implemented as rheological sensors, demonstrating measurement of fluidic *densities* and *viscosities*. Anja Boisen and coworkers provided the physical characterization of several alcohols and oils using transparent SMRs containing only 5 pl of liquid. By correlating the resonators mechanical response to fluidic properties, they achieved a density responsivity of 16 Hz/kg/m³, and a viscosity resolution of 0.025 mPas [63].

SMRs constitute an interesting and promising alternative probe for viscoelasticity measurement. Main improvements, compared to other existing techniques, lie in the minimum fluid volume required (in the order of pl), in the real time analysis and in the possibility to integrate the devices in a microfluidic platform on-chip.

1.3.2 Transduction techniques

Several actuation and readout strategies have been proposed for SMRs. Transduction needs to translate the mechanical vibration of the solid structure into a detectable electrical signal and vice-versa, for readout and actuation, respectively. Few examples of transduction strategies suitable for M-NEMS are listed in Table 1.2

The most basic actuation approach consists in using a commercial *piezo-shaker (or piezoceramic)* actuator, put in contact with the chip. In this case, a piezoelectric (PZE) block in the size range of few millimeters, delivers mechanical vibration at a specific frequency, upon connection to an external voltage source. This method is extremely practical, cheap and easy to implement; however, simultaneous actuation of multiple frequencies is not possible, and particular care is needed in order to firmly attach the PZE block to the chip.

The most widespread integrated actuation strategy found in literature for SMRs is *electrostatic actuation*. This is achieved by integrating, during the SMRs fabrication, two metal electrodes under and in proximity of the resonator (Figure 1.8). Electrostatic actuation is based on the Coulomb attraction force between oppositely charged

plates: $F_{es} = -\frac{1}{2} \frac{\varepsilon_0 \varepsilon_r A V^2}{x^2}$. The electrostatic force is proportional to the squared ratio of applied voltage V over electrodes distance x, and depends on the electrodes area A. In general, this technique provides a non-linear, but fast response with a low power consumption. The transduction current $I_{es} \propto \frac{A}{x}$ scales as l^2 (or l, if only the scaling of the device is considered, while the electrodes distance is assumed constant), thus losing efficiency at the nanoscale. The main limitation is the small achievable displacements.

Thermal actuation has also been reported by Craighead and coworkers, for doubly clamped hollow resonators [64].

Table 1.2: Common transduction techniques for mechanical sensors at the microscale. Actuation can be achieved by applying a pressure, a force or a deformation to the device. Readout is attained by reading on optical signal, or by sensing a generated force or deformation. Some techniques allows both actuation and readout.

Pressure		Force		1	Deformation	
ACTUATION	o Sha	pe Memory Polymers	0	Magnetic	0	Piezoelectric
			0	Electrostatic	0	Thermal
Optical			Force	Deformation		
DETECTION	o Opt	tical lever	0	Magnetic	0	Piezoelectric
	o Inte	erferometry	0	Capacitive	0	Piezoresistive

Two main displacement detection principles can be identified, namely electronic and optical techniques, which can achieve comparable displacement sensitivities in the order of $[fm/\sqrt{Hz}]$. Electrical strategies have impressive degree of miniaturization, but impose a higher fabrication complexity and design restrictions. Optical techniques offer enormous flexibility in fabrication and design, but require bulky instrumentation, set geometrical constraints between the optical probe and the device, and are limited at the nanoscale by light diffraction.

SMRs readout has been largely performed via *optical lever* and *interferometry*. Close feedback loop configuration involving n phase locked loops (PLLs) was recently implemented for the optical readout of n SMRs: devices were arranged in an array configuration and actuated by a piezoceramic actuator, driven by the sum of the n signals demodulated by the PLLs [62].

Integrated electrical readout was also demonstrated for SMRs: *piezoresistive sensors* were fabricated close to the resonator anchor, via ion implantation into single crystal silicon [65]. The deflection of the cantilever induces a change in resistance in the piezoresistor that can be easily measured with a Wheatstone bridge. Piezoresistive readout is easily implemented in large arrays, works for all modes of operation and is linear for small displacements; however, it is a dissipative phenomenon (thermal dissipation via Joule effect) and the thermal noise associated to thin piezoresistive layers can limit detection efficiency.

1.4 Thesis outline

Chapter 2: DESIGN

In this chapter, mechanical resonators, microfluidic network and piezoelectric transduction are separately discussed. Physical requirements, design strategy and main parameters are described.

Chapter 3: SIMULATIONS

This chapter summarizes the study on energy dissipation of Suspended Microchannel Resonators as a function of fluidic and geometrical properties of the devices. A 3-D eigenfrequency analysis of the fluid-structure interaction (FSI) problem is carried out. The obtained numerical results are validated through comparison with theoretical model and experimental data present in literature.

Chapter 4: FABRICATION

This chapter presents the details of the fabrication of arrays of transparent SMRs, with integrated PZE electrodes [66]. After a brief overview about the fabrication processes found in literature, the approach developed in this thesis is presented. Optimization of microchannel fabrication, piezoelectric electrodes definition and resonators release are presented, separately. Advantages and limitations of the developed process flow are discussed in each section. Detailed process flow and runcard are provided in Appendix A and B.

Chapter 5: EXPERIMENTAL SETUP

This chapter presents a brief introduction to MEMS packaging. Follows the description of the developed experimental platform which includes fluidic interface, temperature control and electrical connection. Measurement setup is also presented.

Chapter 6: CHARACTERIZATION

This chapter presents the characterization of fabricated SMRs. Mechanical response is detected for different fluids flowing inside the embedded channels, and for different temperatures. Study of frequency stability is carried out, correlated to a noise analysis of the experimental system in air and vacuum environment.

Chapter 7: CONCLUSIONS AND OUTLOOK

Conclusion and outlook of this PhD project are discussed.

APPENDICES

In order to support the information given in previous chapters, different appendices provide additional details. Fabrication process flow and runcard are included, as well as wafer and fluidic connector layout.

The last section includes the curriculum vitae of the candidate, with the list of attended courses, teaching activities and publications.

Chapter 2

DESIGN

In this chapter, mechanical resonators, microfluidic network and piezoelectric transduction are separately discussed. Physical requirements, design strategy and main parameters are described.

2.1 Introduction

The devices developed during this thesis are *hollow resonant structures* containing a *microfluidic channel* and provided with *piezoelectric electrodes* near the clamp region (Figure 2.1(a)) [66]. The embedded channel allows the real-time analysis of fluidic samples, while the PZE electrodes enable the independent actuation and detection of each resonator. Resonators are arranged in *array* configuration in order to measure the same analyte through multiple consecutive sensors.

Devices are designed in order to enable the real-time measurement of biological particles (i.e. bacteria, RBCs, CTCs, etc.), and extract their mass and stiffness from the resonance frequency response, as shown in Figure 2.1(b).

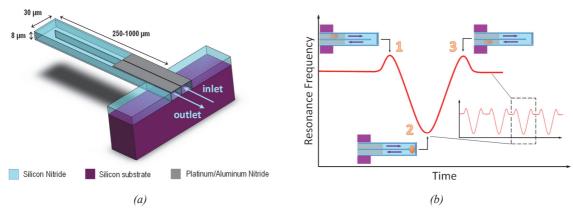


Figure 2.1: Schematic (a) and working principle (b) of the device developed during this PhD thesis. A hollow suspended structure contains a U-shaped microfluidic channel, while piezoelectric electrodes provide electrical actuation and readout [66]. The resonance frequency of the device is monitored over time, while single cells are flown inside the channel and the whole structure is kept in dry environment. The ultimate goal of this project is disentangling cell mass and stiffness effect on the resonance frequency, in order to provide a multiphysical characterization of biological samples in liquid.

2.2 Hollow resonators design

2.2.1 Requirements

Mass (or stiffness) sensitivity is defined as the minimum detectable mass (or stiffness) the device is able to perceive, and is inversely proportional to responsivity, which defines how responsive the device is to the target property. As shown in Eq. 2.1, both analyte mass and stiffness affect the device vibration. This opens to nanomechanical sensing based not only on mass, but also on *stiffness characterization* [29].

A particle flowing in the SMR induces a relative frequency shift given by Eq. 2.1 [67]:

$$\frac{\Delta f_r}{f_r} = \frac{3}{2} \frac{1}{\alpha_n^4} \frac{d^2 \phi_n(x)^2}{dx^2} \frac{E_a}{E_s} \frac{I_a}{I_s} - \frac{1}{2} \phi_n^2(x) \frac{\rho_a}{\rho_s} \frac{A_a}{A_s}$$
Eq. 2.1

where Δf_r is the frequency shift induced by the analyte flowing in the channel; $\phi(x)$ and $d^2\phi_n(x)/dx^2$ are the amplitude of vibration and the curvature of the nth mode at coordinate x along the cantilever length, respectively; E, ρ and I and A are Young's modulus, mass density, second moment of inertia and cross-sectional area, where subscripts a and s refer to analyte and solid cantilever, respectively.

Two linear contributions are found:

- stiffness-induced effect, proportional to the ratio between analyte and cantilever Young's modulus, results in a positive frequency shift (first term of Eq. 2.1). This effect dominates at x = 0 (clamp), where the curvature is maximum and the amplitude of vibration is close to zero.
- mass-induced effect, proportional to the ratio of analyte and cantilever density, produces a negative frequency shift (second term of Eq. 2.1). This effect dominates at x = L (tip), where the amplitude of vibration is maximum and the curvature is close to zero.

However, these effects are orders of magnitude apart, due to the mismatch between analyte and resonator material properties. The structural material of designed SMRs is low-stress silicon nitride (ls-SiN_x). The main reason of this choice is given by fabrication requirements, as will be explained in Chapter 4. In addition, ls-SiN_x presents a number of desirable properties for biosensing applications, such as transparency, biocompatibility, hydrophilicity and chemical stability [68]. As show in Table 2.1, while densities of cells and low-stress silicon nitride are in the same order of magnitude, Young's moduli differ by more than a factor of 10^9 .

Table 2.1: Typical values of density and Young's modulus for cells and low-stress silicon nitride. The ratio between Young's moduli is 8 orders of magnitudes lower than the one between densities. For this reason, the effect of cell mass is largely predominant on the resonance frequency shift, compared to the cell stiffness effect.

	Cells (typical range)) Low-stress Silicon nitride	$\frac{E_a}{E_s}$	$\frac{\rho_a}{\rho_s}$
Density [kg/m³]	~10 ³	3×10^3	10-0	100
Young's modulus [Pa]	~10 ³	260×10^{9}	~10 ⁻⁹	~10 ⁰

The cell mass contribution to resonance frequency clearly dominates over the stiffness effect. Therefore, resonators and fluidic network are designed in order to try to *disentangle the two contributions* and at the same time maximize the stiffness impact. As shown in Eq. 2.1, mass and stiffness effects can be decoupled by confining the cell where each contribution dominates. To achieve this, channels which span 25%, 60% and 100% of the cantilever length are designed (Figure 2.2). The goal is to compare the resonance frequency shift induced by the same particle at different positions along identically-designed cantilevers, and analytically decouple k and m contribution.

A fundamental requirement to achieve high mass and stiffness responsivities is to minimize the cantilever mass per unit length and wall thickness, thus reducing mass and stiffness of the resonator itself. Furthermore, Eq. 2.1 demonstrates that the resonance frequency shift resulting from the analyte flowing inside the resonator is directly proportional to the ratio between the volumes of analyte

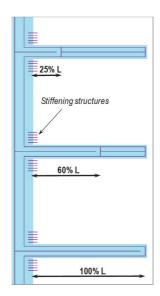


Figure 2.2: Microfluidic channels span different cantilever lengths in order to disentangle analyte mass and stiffness contribution. Stiffening structures are distributed around the clamp to provide structural support.

and cantilever. For this reason, the cross section of the fluidic channel is designed in order to:

- maximize the fluidic volume with respect to the solid volume, reducing the thickness of the channel walls.
- keep the analyte particle constrained in the fluidic channel, in order to maximize its mass and stiffness effect on the resonance frequency shift.

In order to probe the Young's modulus dependence on resonance frequency, which is a typical feature of viscoelastic media (i.e. biofluids and cells), as explained in Chapter 1, cantilevers are designed to span a large *frequency range*. In particular, four different cantilevers designs are considered, resulting in resonance frequencies from few tens of kHz to few MHz (considering the first two resonance modes), as will be shown in Table 2.2. In addition, this allows devices to operate above external vibration frequencies (few kHz).

Finally, it is fundamental to ensure that the top surface of the resonators is flat after channel definition. As will be explained in detail later in this chapter, devices will integrate piezoelectric actuation on top of each SMR. To enable the fabrication and operation of PZE transduction, microfluidic channels are embedded inside the resonators, while the top surface is kept flat.

2.2.2 Materials and dimensions

Figure 2.3 (a) shows the center of one chip (sensing window), which includes two independent arrays of 6 cantilevers each. The left array contains 250 μ m- and 500 μ m- long singly-clamped SMRs, while resonators in the array on the right are 750 μ m- and 1000 μ m-long. All cantilevers are 30 μ m wide and 8 μ m thick, and the cross section of the embedded channels is designed to be 6 μ m x 10 μ m (Figure 2.3 (b)). These dimensions have been chosen considering SMR designs reported in literature by other groups, fabrication feasibility, and the requirements discussed in the previous paragraph.

In particular, the channel cross section is chosen to be comparable in size to the particles and cells to be analyzed. For instance, RBCs are typically 3 μ m x 8 μ m, while CTCs have a diameter between 12 and 25 μ m [9]. The ability of these cells to rapidly deform and flow in capillaries down to few microns in diameter has been discussed in Chapter 1.1.1. Channel walls were initially designed to be around 0.5 μ m, more than 10 times thinner than fluidic channels, in order to minimize mass and stiffness of resonators. However, due to fabrication constraints, the top ls-SiNx wall results 1.4 μ m-thick, as will be explained in Chapter 4. The cross section shown in Figure 2.3 (b) corresponds to a fluidic volume 1.5 times larger than the one of ls-SiNx.

The next sections present the calculation of SMRs moment of inertia, resonance frequency, spring constant and neutral axis. The characteristic parameters of designed SMRs are finally summarized in Table 2.2.

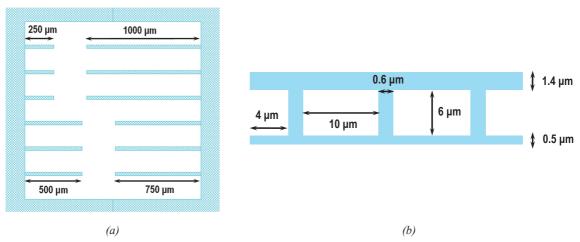


Figure 2.3: Design and dimensions of low-stress silicon nitride SMR array. (a) Detail of a chip design containing two arrays of 6 cantilevers each (sensing window). Resonators' length spans from 250 to 1000 μ m. (b) Cross sectional view of a microchannel cantilever. Resonators are 7.9 μ m thick and 30 μ m wide, and contain a 2-way microfluidic channel having a cross section of 10 μ m x 6 μ m.

2.2.2.1 MOMENT OF INERTIA

Moment of inertia I is calculated as the sum of different terms: moment of inertia of bottom nitride layer, three vertical walls and the top nitride layer (Figure 2.3 (b)). I of each portion is calculated according to Eq. 2.2, where z is the vertical coordinate of the cantilever cross section, z_0 is the neutral axis vertical coordinate, A is the cross sectional area, b and b are cantilever width and height, respectively [69].

$$I = \int_{A} (z - z_{0})^{2} dA = \int_{0}^{h} b \left(\frac{z}{2}\right)^{2} dz = \frac{bh^{3}}{12}$$
Eq. 2.2

$$I_{TOT} = I_{base} + 3I_{vertical} + I_{top} = 7.28 \cdot 10^{-22} \text{m}^4$$
 Eq. 2.3

Considering a Young's modulus equal to 260 GPa for the low-stress silicon nitride [70], the flexural rigidity of the designed SMRs is calculated as:

$$EI_{TOT} = 1.89 \cdot 10^{-10} \text{Nm}^2$$
 Eq. 2.4

2.2.2.2 RESONANCE FREQUENCY

Resonance frequency of the nth vibrational mode is calculated according to the Euler-Bernoulli beam theory [71]:

$$f_{r,n} = \frac{1}{2\pi} \sqrt{\frac{k}{m}} = \frac{1}{2\pi} \left(\frac{\alpha_n}{L}\right)^2 \sqrt{\frac{EI_{TOT}}{\rho A}}$$
 Eq. 2.5

k and m are effective stiffness and mass, respectively. L is the cantilever length, A is the resonator cross section, ρ is the ls-SiN_x density (3000 $\frac{\text{kg}}{\text{m}^3}$, from [70]). α_n is the eigenvalue associated to the nth resonance mode, and is equal to 1.1875 for the first mode of vibration.

2.2.2.3 SPRING CONSTANT (STIFFNESS)

The spring constant k of a singly-clamped beam of length L, subjected to a uniformly-distributed load q is given by the ratio of load and deflection at the tip [69]:

$$k = \frac{F(L)}{\delta(L)} = \frac{qL}{\left(\frac{qL^4}{8EI_{TOT}}\right)} = \frac{8EI_{TOT}}{L^3}$$
Eq. 2.6

Analytical values of resonance frequency and stiffness for the different cantilever geometries are given in Table 2.2.

2.2.2.4 NEUTRAL AXIS

Neutral axis of the low-stress silicon nitride cantilever, considering the cross section in Figure 2.3(b) is calculated as shown in Eq. 2.7. The same strategy used for the moment of inertia is adopted.

$$z_0 = \frac{\int bzdz}{\int bdz}$$
 Eq. 2.7

$$z_{0_{TOT}} = \frac{\int_{base} bzdz + 3\int_{vertical} bzdz + \int_{top} bzdz}{\int_{base} bdz + 3\int_{vertical} bdz + \int_{top} bdz} = 5.073 \cdot 10^{-6} \text{m}$$
Eq. 2.8

2.2.2.5 SUMMARY OF CHARACTERISTIC PARAMETERS

As shown in Table 1.1, designed resonators result in an operating frequency range between 15 and 240 kHz, calculated analytically according to Eq. 2.5. The estimated mass of the empty resonators ranges between 65 and 250 ng. The liquid-to-solid volume ratio from clamp to tip of a suspended resonator is about 1.5, considering a channel that spans the entire resonator length. Stiffness values are also reported for the four geometries, calculated as in Eq. 2.6.

Table 2.2: SMR parameters estimated from design. Values are calculated for singly clamped beams, assuming microfluidic channels of the same length as the resonator.

Cantilever Dimensions [μm]	Solid Mass	Solid volume	Liquid		e frequency Hz]	Stiffness
(width x thickness x length)	[ng]	[pl]	Volume [pl]	1st mode	2 nd mode	[fN/m]
30 x 7.9 x 250	64	19.9	30	236.86	1428.80	9.24×10^{-2}
30 x 7.9 x 500	128	39.5	60	60.6	367.70	1.18×10^{-2}
30 x 7.9 x 750	190	59.1	90	26.81	164.59	3.53×10^{-3}
30 x 7.9 x 1000	253	78.7	120	15.11	92.87	1.50×10^{-3}

2.3 Microfluidic network

A fluidic network is designed to deliver the microfluidic sample to all the resonators in the array. Fluidic inlets and outlets provide an interface with external connection to fluidic pumps, as further described in Chapter 5. Micropillars are embedded inside the fluidic channels to improve robustness and avoid structural collapse.

2.3.1 Requirements

To provide efficient and fast fluidic delivery to the SMR sensors, the *fluidic resistance* of the designed network should be minimized. Ideally, channels should be kept as short and wide as possible, as can be seen in Eq. 2.10. However, structural robustness of ls-SiN_x membranes, fabrication constraints and electrical tracks geometry are additional parameters that need to be considered (Chapter 4 and Paragraph 2.4). In addition, using a *hydrophilic material* as low-stress silicon nitride facilitates liquid delivery [72].

2.3.2 Materials and dimensions

Figure 2.4 shows the designed fluidic network (delimited by pink lines), integrated with the resonator geometry (solid light blue). In order to decrease the fluidic resistance, the microfluidic channel width gradually increases from 10 μ m in the resonator to 150 μ m near the inlets. To avoid channel collapse in this region where the aspect ratio of the top membrane becomes lower (< 0.01), 0.6 μ m x 4 μ m low-stress silicon nitride *micropillars* are integrated inside the channels: this provides mechanical support to the 1.4 μ m-thick top nitride layer (Figure 2.4). Pillars are not included close to the resonator arrays, where the channel width is reduced below 20 μ m and the lower aspect ratio of the ls-SiN_x membrane (~0.1) prevents structure collapse. Furthermore, including vertical pillars in the suspended channels could cause particle trapping and channel clogging.

Low-stress silicon nitride *stiffening structures* are distributed around the sensing window (center of the chip containing resonators) and around the clamp of the cantilevers in order to limit the effect of the undercut region, which results from isotropic release, as will be explained in Chapter 4.

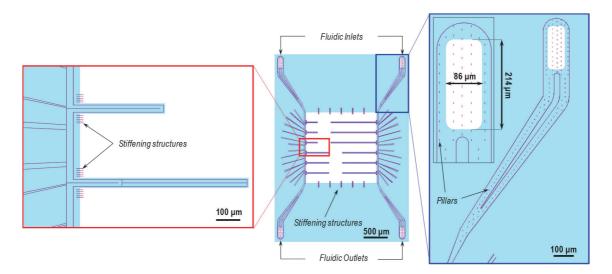


Figure 2.4: Microfluidic and resonator design. (centre) The chip contains two SMR arrays, presenting independent fluidic inlets and outlets. Microfluidic channels span 25%, 60% and 100% of the cantilever length, in order to evaluate and compare mechanical responses of particles traveling at different coordinates along the suspended resonators. Low-stress Silicon Nitride (ls-SiN_x) stiffening structures are distributed around the sensing window in order to limit the effect of the undercut region, which results from isotropic release, as will be explained in Chapter 4. In order to decrease the fluidic resistance, the microfluidic channel width gradually increases from $10 \mu m$ in the resonator to $150 \mu m$ near the inlets (right). Since the channels are then relatively wide close to the inlet and outlet, $0.6 \mu m \times 4 \mu m$ ls-SiN_x pillars are included to provide mechanical support and avoid channel collapse.

The designed microfluidic network can be characterized by two main parameters: Reynolds number and fluidic resistance. Other parameters relevant at the microscale such as diffusion coefficient, surface tension or surface to volume ratio are not determinant for the application developed in this thesis and will not be reported.

2.3.2.1 REYNOLDS NUMBER

Reynolds number β is an adimensional parameter representing the ratio between inertial and viscous phenomena taking place in a microfluidic channel, and providing information about the flow. Reynolds number below 2300, where viscous forces dominates and provide smooth fluidic motion, characterizes *laminar flows* [73].

In case of SMRs, the Reynolds number can be calculated as follows [74]:

$$\beta = \frac{\rho_f \omega h_f^2}{\mu_f}$$
 Eq. 2.9

where ρ_f is the fluidic density, μ_f is the dynamic fluidic viscosity and h_f is the channel thickness. Considering water, 100% channel length and first mode of resonance (Table 2.1), β ranges from 53 for the 250 μ m-long SMR, to 3.4 for the 1000 μ m-long SMR (considering the first mode of vibration). These values ensure laminar flow in the suspended microfluidic channels.

2.3.2.2 FLUIDIC RESISTANCE

The fluidic resistance of a channel is given by the ratio between applied differential pressure ΔP between inlet and oulet, and generated fluidic flow Q_f . For a rectangular channel with low aspect ratio, as in the case of designed SMRs, the fluidic resistance R_f can be evaluated as [73]:

$$R_{f} = \frac{\Delta P}{Q_{f}} = \frac{12\mu_{f}L}{bh_{f}^{3}} \cdot \frac{1}{1 - \frac{h_{f}}{b} \left[\frac{192}{\pi^{5}} \tanh\left(\frac{\pi b}{2h_{f}}\right)\right]}$$
 Eq. 2.10

The fluidic network can be divided in several sub- sections. The total fluidic resistance can be calculated considering the analogy to an equivalent electrical circuit, as shown in the example of Figure 2.5. R_f is calculated for the array of 6 cantilevers, from inlet to outlet, considering water at 25°C in the channels. In particular, the array composed of 250 μ m-long and 500 μ m-long SMRs (left side of Figure 2.3 (a)) presents a fluidic resistance equal to 3.44 \cdot 10¹⁶ [Pa s/m³], while for the longer array (right side of Figure 2.3 (a)) R_f is calculated to be 6.72 \cdot 10¹⁶ [Pa s/m³]. Applying a differential pressure across the SMR chip equal to 1 bar between inlet and outlet, and considering an incompressible fluid, the resulting flow is equal to 3.26 \cdot 10⁻¹²m³/s (0.19 μ l/min) and 1.67 \cdot 10⁻¹²m³/s (0.10 μ l/min), for the shorter and longer array, respectively.

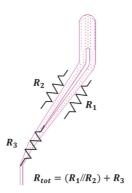


Figure 2.5: Microfluidic—electrical analogy for a portion of the design SMR network. This strategy is used for the calculation of the total hydraulic resistance of the designed devices.

2.4 PZE electrodes

Piezoelectricity (PZE) is the property of certain materials to respond with a mechanical deformation to an applied voltage (Eq. 2.11), and to generate charges when the material is deformed (Eq. 2.12).

The coupling between electrical and mechanical phenomena is given by the piezoelectric matrix d_{ji} , and can be analytically expressed as:

$$\varepsilon_i = C_{ij}\sigma_j + d_{ij}E_j$$
 Eq. 2.11

$$D_i = \epsilon_{ij} E_j + d_{ij}^T \sigma_j$$
 Eq. 2.12

where ε_i and σ_j are strain and stress vectors, D_i and E_j are displacement current and electric field, C_{ij} is the compliance matrix, ε_{ij} is dielectric permittivity, and d_{ji} is the piezoelectric matrix.

Piezoelectric transduction of mechanical resonators can be achieved by integrating a PZE layer, sandwiched between two metal electrodes, in contact with the vibrating structure. Applying an electrical voltage V(t) across the thickness of the piezoelectric layer causes a deformation in the material, which results in longitudinal expansion (assuming a structure working in pure elongation). The elongation force is translated into a bending moment $M_{PZE}(t)$ which induces cantilever deflection, proportional to the offset z_{offset} between the neutral axis of the solid structure and the neutral axis of the piezoelectric layer, as shown in Eq. 2.13 [75]:

$$M_{PZE}(t) = d_{31}E_{PZE}w_{PZE}z_{offset}V(t)$$
Eq. 2.13

where E_{PZE} is the Young's modulus of the piezoelectric material, and w_{PZE} is the electrodes' width.

The vibration of the cantilever produces a displacement field $D(\omega)$, resulting in a motional current $i_0(\omega)$ that can be measured from the displacement current $i_D(\omega)$, expressed as in Eq. 2.14 [71]:

$$i_D(\omega) = i_0 + i_m = \left(j\omega C_f + j\omega C_m \frac{1}{1 - \left(\frac{\omega}{\omega_n}\right)^2 + j\frac{\omega}{\omega_n Q_n}}\right) V(\omega)$$
 Eq. 2.14

where ω_n is the radial resonance frequency of the nth mode, while C_m is the motional capacitance of the resonator. C_f models the static capacitance (or feedthrough capacitance) between electrodes on the resonator and induces a parasitic current i_0 proportional to the applied voltage, but not related to the motion of the cantilever (first term of Eq. 2.14).

Piezoelectric transduction of mechanical resonators has been already reported in literature, demonstrating excellent efficiency of ultra-thin PZE layer (down to 50 nm) [76], but it has never been implemented in arrays of hollow resonators.

In this project, piezoelectric (PZE) transduction is integrated on top of each resonator to enable independent actuation and detection of devices [66]. Electrical connection between devices and an external lockin amplifier is provided via a custom-made printed circuit board (PCB), as described in Chapter 5.

2.4.1 Requirements

Piezoelectricity is chosen as transduction technique over other possibilities (see Table 1.2) because of several attributes [76, 77]. (i) Intrinsic integrability, as it does not require the fabrication of small gaps like electrostatic transduction, or external bulky setup like optical or magnetic techniques. (ii) High efficiency and low power consumption, that can be four times lower than the one of laser and piezoresistive transducers. (iii) In the case of AlN (chosen PZE material) low thermal budget while processing the piezoelectric layer, which allows for CMOS integration. (iv) Piezoelectricity is a non-dissipative effect due to low current flowing in the PZE layer, thus avoiding heating of the devices, typical of optical or piezoresistive techniques. (v) It provides a fast and linear response. (vi) It enables both actuation and detection and has low driving-voltage requirements (few Volts).

However, few design considerations are fundamental in order to attain successful transduction. In order to maximize the PZE-induced deflection, the piezoelectric layer and resonator axes should be placed as far as possible from each other (large z_{offset}), as shown in Eq. 2.13. PZE transducers' mass and stiffness need to have minimum impact on structure dynamics, while ensuring efficient sensing capabilities. Also, signal crosstalk between actuation and detection electrodes needs to be minimized.

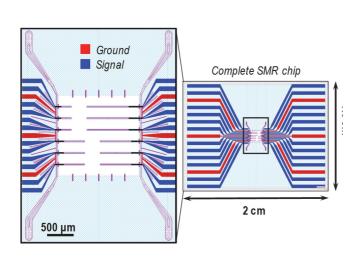
Finally, electrical tracks and microfluidic channels are designed in order to avoid to cross each other, except on top of resonators where the overlap cannot be avoided. This is a precaution to avoid parasitic losses through the liquid, and undesired electrical or thermal effect on the fluidic samples.

2.4.2 Materials and dimensions

In this project, *Aluminum nitride* (AIN) is chosen as piezoelectric material. AIN can be deposited with a low thermal-budget process (300°C) via standard clean-room sputter deposition, and has already been successfully implemented in flexural beam structures [76, 78]. In addition, AIN shows overall good material properties: it possesses a high dielectric strength (0.05 V/nm), which provides resistance to electrical breakdown, and low relative permittivity compared to other PZE materials ($\epsilon_{AIN} = 9$ at 1 MHz) compared to other PZE material, which results in low power requirements [78-80]. However, since AIN piezoelectric properties depend on the film thickness, fabricating ultra-thin (below 100 nm) AIN films that retain good electro-mechanical transduction efficiency is challenging [80].

In this thesis, to minimize the impact of piezoelectric electrodes on mechanical performance of SMRs, AlN thickness of 300 nm is chosen as a tradeoff between added stiffness and mass, and PZE efficiency (Figure 2.8). AlN is sandwiched between a bottom and a top *Platinum* (Pt) layer, 25 nm- and 50 nm-thick, respectively (Figure 2.7). Platinum demonstrated to be the optimum substrate for AlN growth, and together with a seed layer (15 nm AlN), limits residual stress and improves crystal orientation of the PZE film [81]. The top Pt layer is thicker than the bottom one, in order to ensure coverage of the 40 nm-thick step (seed layer and bottom electrode) during film deposition; it also provides robustness for electrical connections, as will be explained in Chapter 4.

PZE electrodes extend from the edge of the chip, until reaching the top of the resonators, as shown in Figure 2.6. In order to limit parasitic reactances, PZE tracks travel on separate paths, and the only geometrical overlap occurs on top of the SMRs, as shown in Figure 2.7. In addition, in proximity to the sensing window, where the distance between electrical tracks is reduced, trenches filled with ls-SiN_x are defined in between the tracks in order to limit capacitive coupling through the substrate. Substrate consists of a standard Silicon wafer coated with 500 nm of ls-SiN_x, $6 \text{ } \mu \text{m}$ of polysilicon (sacrificial material for microchannel fabrication), and $1.4 \text{ } \mu \text{m}$ of ls-SiN_x.



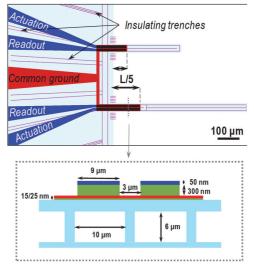


Figure 2.6: Overview of piezoelectric electrodes pattern. PZE electrodes extend from the edges of the chip to the top of resonators. Bottom Pt electrode (in red) delivers a ground signal, shared between pairs of SMRs. Two top Pt electrodes (in blue), deliver a voltage signal to each device, for independent actuation and readout. Size (450x4500 µm) and pitch (1 mm) of electrodes at the edge of the chip, are chosen in order to interface the SMR chip with commercial electrical connectors. Insulating trenches filled with Is-SiNx are defined between the electrical tracks in order to limit capacitive coupling through the substrate.

Figure 2.7: (top image): Piezoelectric electrodes integrated on 250 µm- and 500 µm- long SMRs Electrodes extend for one fifth of the total resonator length. Bottom and top electrodes overlap only on top of the SMRs. (bottom image): Cross sectional view of a PZE-transduced SMR. From the bottom it is possible to see: AlN seed layer, bottom Pt (ground, in red), active PZE layer (in green), top Pt (signal, in blue). Two separated AlN/Pt fingers deliver actuation and readout signals, in order to minimize crosstalk between actuation and detection.

Size $(450 \text{ x} 4500 \text{ }\mu\text{m})$ and pitch (1 mm) of electrodes at the edge of the chip are chosen in order to interface the SMR chip with commercial electrical connectors (Figure 2.6). The length of the electrodes is chosen to be 20% of the total resonator length (Figure 2.7 and Figure 2.8). The main reason is to allow visual access to the microfluidic channel: this will help tracking the particle position during experiments, as well individuating air bubbles or clogs. Even though full-length electrodes would provide the best transduction efficiency, the choice of

using electrode length equal to one fifth of cantilever length constitutes the second best option to simultaneously maximizes the amplitude of the first and second mode of vibration.

Each SMR is reached by three electrical tracks, as presented in Figure 2.7. Ground signal is delivered by the bottom Pt electrode (in red), which is deposited on top of the seed AlN layer (thin green layer). Actual voltage signal is delivered via two separated tracks, for independent actuation and detection, made up of top Pt electrode (in blue) placed on top of the active AlN layer (in green).

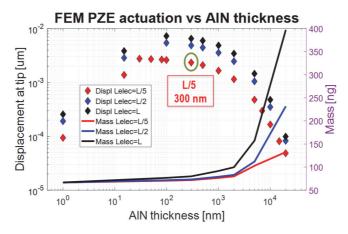


Figure 2.8: Study of PZE electrodes thickness and length via FEM simulations. A PZE-actuated singly clamped SMR is simulated, and the static deflection at tip is extracted for electrodes extending for 1/5, ½ and full SMR length. Actuation voltage of 1.5 V is applied in all cases, except for 15 nm- and 1 nm- thick AlN, where the maximum voltage allowed by the electrical breakdown is considered (assuming a breakdown field of 0.017 V/nm). The thickness of Aluminum Nitride is chosen to be 300 nm as tradeoff between transduction efficiency and mass and stiffness loading on the resonators. The length of the electrodes is set to one fifth on the resonator length to provide visual access to the channels.

2.4.2.1 MOTIONAL PARAMETERS

The expression of displacement current $i_D(\omega)$ given in Eq. 2.14, describes the transfer function of a cantilever resonator, that can be modeled according to Butterworth-Van Dyke (BVD) electrical equivalent circuit [71], as shown in Figure 2.9.

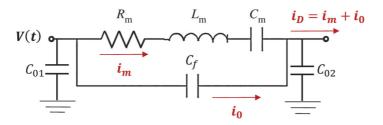


Figure 2.9: Butterworth-Van Dyke (BVD) electrical equivalent circuit of PZE-transduced resonator [71]. The SMR is modeled as a RLC network. Parasitic capacitances C_{01} and C_{02} model the electrical coupling to ground, through the PZE layer. Feedthrough capacitance C_f represents the electrical coupling between PZE track through the substrate. Displacement current i_D is given by the sum of motional current i_m , generated by the resonator vibration, and parasitic current i_0 , flowing in the feedthrough capacitance C_f . At the microscale, the parasitic current can predominate over the motional current, and balancing readout techniques need to be implemented.

The resonator is modeled as a series of *motional parameters* $(R_m, L_m \text{ and } C_m)$ evaluated as showed in Eq. 2.15 [71].

$$C_m = E_{PZE} w_{PZE} \left(d_{31} z_{offset} \phi_n'(L_{PZE}) \right)^2 \left(\frac{L}{t_{tot}} \right)^3, \qquad L_m = \frac{1}{\omega_n^2 C_m}, \qquad R_m = \sqrt{\frac{L_m}{C_m}} \frac{1}{Q} \qquad Eq. \ 2.15$$

where $\phi'_n(L_{PZE})$ is the first spatial derivative of the beam eigenmode, evaluated at coordinate $x = L_{PZE}$, and t_{tot} is the total thickness of the PZE stack.

Motional parameters are calculated in case of electrodes length equal to one fifth of total cantilever length, as designed, and compared to the case of PZE stack which spans the full resonator length. The analytical code used for the calculation is included in Appendix E, while Table 2.3 shows the numerical values for an empty 250 µmlong SMR. As expected, limiting the PZE electrodes length deteriorates the transduction efficiency, which ideally requires large motional capacitances and small motional resistances. As previously explained, this constitutes a tradeoff with added stiffness and mass, and visual access to the channels.

The equivalent circuit in Figure 2.9 also includes parasitic capacitances, which deteriorate the transduction signals. Parasitic current i_0 flows through the feedthrough capacitance C_f , which models the coupling between electrical tracks, through the substrate. The portion of i_0 collected at the output terminal can be minimized via balancing readout techniques, reducing the surface of the electrical tracks, and choosing a high-resistive substrate [66]. C_{01} and C_{02} represent parasitic capacitances between actuation/detection electrode and ground, and model electrical coupling through the PZE layer. In order to limit parasitic losses, actuation and readout is performed via two different electrical tracks, and their overlap is minimized by design. In addition, they are placed on top of 1.4 μ m low stress Silicon nitride insulating substrate, which separate them from the conductive layers laying underneath. Furthermore, insulting trenches filled by Is-SiNx are defined between the electrical tracks around the sensing window, in order to limit capacitive coupling through the substrate.

Table 2.3: Motional parameters calculated for an empty 250 μ m-long SMR, assuming Q=500. Compared to the case of PZE electrodes covering the full length of the resonator, the designed devices present a motional capacitance 380 times lower, while motional capacitance and resistance are 26 times larger.

Electrodes length	Cm [fF]	Lm [H]	Rm [MΩ]
L/5	0.0426	10591	31.5
L	1.1165	405	1.2

2.5 Complete wafer overview

Figure 2.11 shows the layout of a 4-inch Silicon wafer. A single wafer contains 16 SMR chips, and each chip includes two SMR arrays.

Electrical test structures are located in different regions of the wafer, and are used to verify the insulation of AlN, as previously explained in this chapter (Figure 2.10).

Two boxes, 8 x 30 mm, are designed for X-ray Diffraction (XRD) measurements, to evaluate the crystal orientation of Aluminum Nitride [80]; these regions are defined as a stack of seed AlN, bottom Pt, active AlN and top Pt, and their dimensions are chosen accordingly to the XRD-tool requirements.

Multiple test structures, as the one shown in Figure 2.10, are included across the wafer, in order to check electrical insulation provided by AlN between the bottom (red) and top (blue) Pt layers.

In addition to the design described in this chapter (Figure 2.12(a)), other three chip configurations are comprised in the wafer layout: a simpler 4-cantilever chip, which only contains SMRs with full channel length (Figure 2.12(b)), a doubly-clamped beam chip with 2-ways fluidic channels (Figure 2.12(c)) and a doubly-clamped beam chip with 1-way fluidic channels (Figure 2.12(d)). These chips are replicated multiple times and randomly distributed across the wafer.

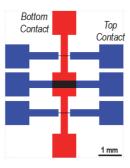


Figure 2.10: Layout of electrical test structures.

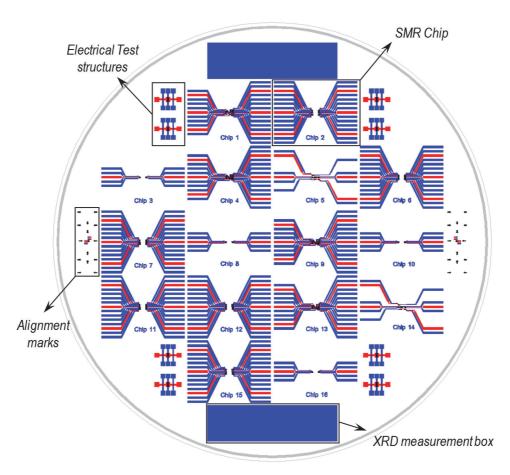


Figure 2.11: Full wafer layout.

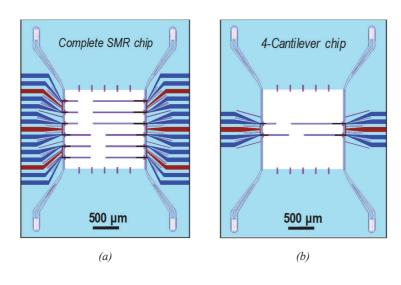
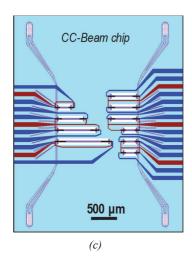
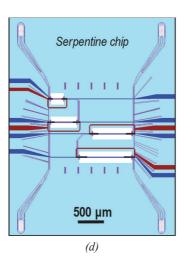


Figure 2.12: Chip designs included in the wafer. (a) Complete-chip described in this chapter. (b) 4-Cantilever chip, only containing channels as long as the resonators. This simpler design includes one 250 µm- and one 500 µm-long SMR in the left array, while a 750 µm- and a 1000 µm-long SMR constitute the right array. (c) Few chips also include doubly-clamped (CC) beams. The left array is made of four beams, from 250 µm to 1000 µm in length, containing a u-shaped channel which spans the whole length of the resonators. The right array includes three 250 µm-long and three 500 µm-long CC SMRs,





where the embedded channel extends for 25%, 60% and 100% the resonator length. (d) Serpentine chip, containing doubly-clamped beams with a 1-way embedded fluidic channel, which spans the whole resonator length. This chip contains 4 beams, one per each of the designed lengths.

2.6 Chapter conclusion

The devices developed during this thesis are hollow resonant structures containing a microfluidic channel and provided with piezoelectric electrodes near the clamp region.

Resonators are made of low stress Silicon Nitride and span a frequency range from tens of kHz to few MHz, considering the first two resonant modes.

A *fluidic network* is designed to deliver the microfluidic sample to all the resonators in the array, enabling simultaneous detection of mass and stiffness of the analyte. The cross section of the suspended fluidic channel, 6 µm x 10 µm, is chosen in order to maximize the fluidic volume and keep the analyte particle constrained in the channel, with the aim of maximizing its mass and stiffness effect on the resonance frequency shift. Fluidic inlets and outlets provide an interface with external connection, while micropillars are embedded inside the fluidic channels to improve robustness and avoid structural collapse. Channels of several lengths are designed (25%, 60% and 100% of the cantilever length). The goal is to compare the resonance frequency shift induced by the same particle at different positions along identically-designed cantilevers, and analytically decouple mass and stiffness contribution.

Electrical transduction is integrated on top of each resonator: a 300 nm-thick Aluminum Nitride layer is sandwiched between two Platinum layers to enable independent actuation and detection of devices. The length of the electrodes is chosen to be 20% of the total resonators' length, to minimize mass loading and allow visual access to the microfluidic channel during experiments, while still providing efficient transduction. In order to limit parasitic reactances, PZE tracks travel on separate paths, and the only geometrical overlap occurs on top of the SMRs. In addition, insulating trenches filled with ls-SiNx are defined between the electrical tracks around the sensing window, to limit capacitive coupling through the substrate.

Chapter 3

SIMULATIONS

This chapter summarizes the study on energy dissipation of Suspended Microchannel Resonators as a function of fluidic and geometrical properties of the devices. A 3-D eigenfrequency analysis of the fluid-structure interaction (FSI) problem is carried out. The obtained numerical results are validated through comparison with theoretical model and experimental data present in literature.

This chapter is a brief extract of the results collected during one of the Master Projects supervised by the PhD Candidate, available in [82].

3.1 Introduction

The goal of designed SMR sensors is analyzing non-newtonian fluids and their effect on resonance frequency and quality factor. In particular, devices are designed to enhance the analyte stiffness effect on resonance frequency, and disentangle it from mass contribution. Given the challenge of this application, FEM simulations are used to investigate its feasibility, and to study physical mechanisms and critical parameters involved.

At first, the ls-SiN_x resonator and the medium inside the embedded channels are both modeled as solid domains, via commercial software. Channel volume is defined as a ficticious material with density and Poisson ratio set to zero. An eigenfrequecy analysis is conducted while sweeping the Young's modulus E of the material in the channels. A responsivity equal to 4 kPa is found for a 500 μ m-long SMR, considering a E range between 100 kPa and 10 GPa and assuming a frequency noise of 10^{-8} . This result is promising in terms of biological analyses, for example Young's moduli of tumor and healthy cells differ by hundreds of Pa at 100 Hz [8]. However, the model is not a realistic representation of the problem since there is no fluid domain involved. Thus a different strategy is adopted in order to enable fluidic analyses.

Channel volume is defined as a liquid domain, and a *fluid-structure interaction* (FSI) study is conducted. A home-made computational code is implemented using an open-source software, in collaboration with Prof. François Gallaire and Dr. Andrea Fani from LFMI at EPFL. The fluid-structure interaction problem is addressed using Arbitrary Eulerian to Lagrangian (ALE) formulation, in order to solve both fluid and solid domain in a unique framework, as shown in Figure 3.1 [83]. A linearized 3-D modal analysis of the solid beam with the internal fluid is carried out. Resonance frequency and quality factor are extracted from the obtained complex eigenvalues [84].

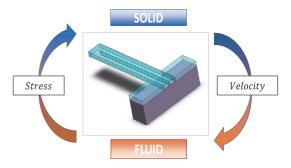


Figure 3.1: 2-way coupled fluid-structure interaction. At the fluid-solid interface, fluid stresses and solid velocities are imposed as boundary conditions to achieve full physical coupling.

FEM code results particularly complex to operate. Also, domains need to be meshed on a different software, and a third software is needed to analyze and plot the results. Fortunately, ALE analysis is found to be available in commercial software, thus the model is rebuilt in a more user-friendly configuration, maintaining the same approach.

In this chapter: a 3-D eigenvalue study in the frequency domain is conducted. A doubly-coupled fluid-structure interaction is solved by means of Finite Element Modeling (FEM). Solving an eigenvalue problem and exploiting the symmetry of the SMR allows to study frequency and energy dissipation as a function of fluidic properties. 2-way physical coupling is attained by imposing solid velocity field and fluid stresses as boundary conditions at the fluid-solid interface. The reliability of our model is demonstrated through the comparison with theoretical and experimental results present in literature. Since there are no data available for resonance frequency as a function of stiffness, the study is focused on SMR energy dissipation, which has been largely characterized in the past years as a function of geometrical and fluidic properties.

3.2 Energy dissipation in SMRs

When operating a mechanical resonator as a sensor, it is desirable to monitor and possibly limit the energy dissipated during motion, in order to have a relatively high quality factor Q. Q is defined as the ratio between energy stored and energy lost during one cycle of vibration, and determines the frequency resolution of the resonator.

Main dissipation mechanisms in MEMS resonators are i) viscous dissipation through the surrounding medium, ii) elastic losses to the substrate through the clamp and iii) dissipative mechanisms intrinsic within the resonator [71, 85].

$$\frac{1}{Q_{TOT}} = \frac{1}{Q_{environment}} + \frac{1}{Q_{clamp}} + \frac{1}{Q_{intrinsic}}$$
Eq. 3.1

Mechanical biosensors need to operate with fluidic samples, thus they are usually immersed in liquid media. The main source of energy dissipation, in this configuration, is the viscous drag induced by the fluid on the solid structure, which causes Q to drop down to few units. As demonstrated in literature [41], energy dissipated by resonators immersed in liquids monotonically increases together with dynamic viscosity of the surrounding fluid.

In case of SMRs, the liquid medium is confined to the interior of the resonator. This allows to retain quality factors in the order of 10⁴ when the device is surrounded by vacuum. In this case, a more complex dissipation mechanism is involved. Theoretical and experimental results proved that in these devices the energy dissipation is a non-monotonic function of the fluid dynamic viscosity [74]. In particular, above a certain range of viscosity, the quality factor tends to oscillate around a stable value, in contrast with conventional solid cantilevers (Q monotonically decreasing with increasing viscosity).

John Sader and coworkers have thoroughly analytically investigated in several papers this unique feature of SMRs [74, 86, 87]. Describing the details of such complex theory is beyond the purpose of this thesis, where just a brief summary of the reported theory is given. The interested reader can refer to the original paper [74] or to the master thesis work supervised by the PhD candidate [82].

The model in [74] focuses only on the dissipation within the fluid, which is analyzed using a 2-D model. Quality factor behavior as a function of fluidic viscosity stems from two competing mechanisms:

- the *shearing* of the fluid on the microchannel walls due to inertial effects of the viscous boundary layer at the fluid-solid interface; the dissipation induced by this phenomenon is minimum at very high (solid-like behavior) and very low (ultra-thin viscous boundary layers) viscosities.
- the *pumping* of the fluid in and out of the resonating channel, due to cross-sectional asymmetries (Z_0) between the microfluidic channel and the resonator.

Figure 3.2 shows the analytically-predicted behavior of the normalized quality factor $F(\beta)$, in Eq. 3.2, as a function of the Reynolds number β [88]. As shown in Eq. 2.9 and reported again below, β is inversely proportional to the fluid dynamic viscosity μ_f , and directly proportional to fluidic density ρ_f , radial resonance frequency ω and fluid thickness h_f . Multiple curves are displayed for different values of the normalized off-axis placement Z_0 . This last parameter is defined as the distance in cross section between the microfluidic channel axis and the beam neutral axis, normalized by the channel thickness.

$$F(\beta) = Q \frac{\rho_{fluid}}{\rho_{cant}} \left(\frac{h_{fluid}}{h_{cant}}\right) \left(\frac{b_{fluid}}{b_{cant}}\right) \left(\frac{h_{fluid}}{L}\right)^{2}$$

$$\beta = \frac{\rho_{f} \omega h_{f}^{2}}{\mu_{f}}$$

$$Eq. 3.2$$

In the *low viscosity regime* (higher β values) the inertial shearing mechanism dominates, and the quality factor monotonically decreases with increasing viscosity (decreasing beta).

In the *high viscosity regime* (lower β values), a competing combination of the two dissipative effects generates oscillations in the quality factor around a stable value. *Fluid compressibility* is of paramount importance in this regime: it induces local changes of fluid volume, thus reducing the shear velocity gradients, and limiting the energy dissipated through the pumping mechanism.

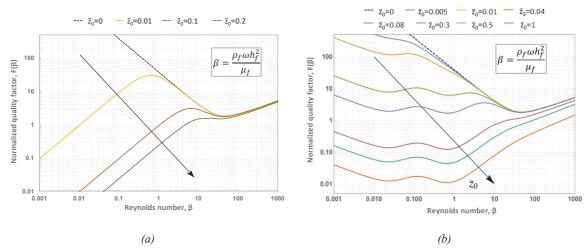


Figure 3.2: Normalized quality factor $F(\beta)$ as a function of Reynolds number β in case of incompressible (a) and compressible (b) fluid. The equation in the inset shows the dependence of β of fluidic density ρ_f , fluidic viscosity μ_f , radial resonance frequency ω and channel thickness h_f . The fluidic channel off-axis placement Z_0 strongly affects the quality factor, as it induces an in-and-out fluid pumping at the entrance of the resonating channel. The black arrow indicates increasing values of Z_0 , while the black dashed line depicts the on-axis case ($Z_0 = 0$), where no pumping effect occurs. From (a) to (b) it is possible to see the effect of fluid compressibility, which mitigates the pumping mechanism and thus the energy dissipation at low β . (Courtesy of Andrea Gerbino [82]).

Figure 3.2 highlights the strong effect of the microfluidic off-axis placement (Z_0) on the quality factor. In the on-axis case $(Z_0 = 0)$, black dashed line, the pumping mechanism does not occur. The reason is that the fluidic channel is symmetrically distributed around the resonator neutral axis. The mechanical vibration induces a symmetric shear strain (in cross section) on the fluid: no global fluidic volume-change occurs at the entrance of the vibrating channel. At low β , quality factor monotonically increases with increasing viscosity.

However, as soon as the symmetry is lost $(Z_0 \neq 0)$, the energy dissipation is enhanced: asymmetric extension and compression of the fluid causes an in-and-out pumping at the entrance of the resonant channel. Fluid compressibility reduces the volumetric flux and therefore the pumping effect on the quality factor. In this case, increasing viscosity does not improve Q.

An increasing or stable quality factor for increasing viscosities is a feature unique to SMR devices. Many other parameters are involved in the dissipation mechanism, such as fluid compressibility, solid structure Poisson

ratio and mode number, among others. This makes the analytical model extremely complex and difficult to use in practical applications [74, 86, 87].

In the following section of this chapter a numerical model developed via commercial software is proposed. The aim is to provide a more immediate and intuitive tool to be used to understand and predict experimental results. Upon validation of the proposed model with theory and data from literature, the developed tool will be employed to investigate the properties of more complex phenomena as viscoelasticity, and viscoelastic particles dispersed in newtonian fluids.

3.3 FEM modeling: Fluid Structure Interaction

3.3.1 Model geometry and mesh

In order to enable comparison with the model in literature, a very similar geometry and same material (Silicon) are investigated. In particular, device B and C described in [74] are considered because their aspect ratio is similar to the one of devices designed in this thesis. Detailed geometrical properties are shown in Table 3.1.

Table 3.1: Geometrical properties of simulated devices [74].

Description	Parameter	Device B, [µm]	Device C, [μm]
Channel height	h_f	8	15
Channel width	b_{fluid}	16	40
Channel length	L	204	315
Cantilever height	h_c	12	19
Cantilever width	b_c	33	57
Cantilever length	length	210	321
Rigid channel length	L_c	204	240
Middle wall width	b_{wall}	2	2

A middle wall defines the separation between the two ways of the microfluidic channel running through a silicon singly-clamped beam. The microfluidic channel is extended over the clamp for a length L_c , in order to simulate the fluid dynamics at the entrance of the suspended device, and to place the reference atmospheric pressure far from the resonator. Geometrical symmetry is exploited by simulating only 1-way of the microfluidic channel. As a consequence, number of nodes and computational effort are substantially reduced.

Fluid and solid domains are meshed with two different strategies. A coarser and uniform mesh is applied to the solid structure, as dissipation mechanisms in solid volumes are not considered, and the eigenfrequency analysis does not require high refinement in order to obtain stable results. On the other hand, discretization of the fluid domain is finer in order to resolve the thin viscous boundary layers at fluid-structure interface. Hence, the fluidic mesh density increases close the walls of the microfluidic channel, as well as close to free-end of the suspended structure (Figure 3.4). Element quality, aspect ratio and mesh convergence are studied in order to ensure an accurate solution and model convergence [82].

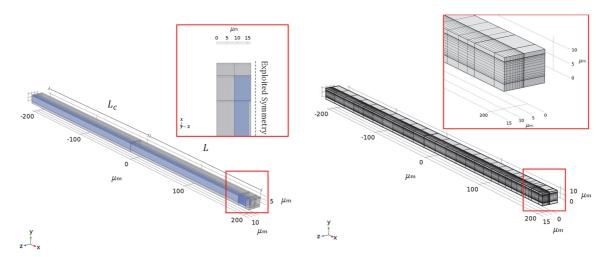


Figure 3.3: Simulated 3-D geometry. Silicon nitride is shown in grey, while the liquid is represented in blue. The resonator extends for 0 < x < L. The microfluidic channel continues over the clamp for a length L_c , in order to simulate the fluid dynamics at the entrance of the suspended device, and to place the reference atmospheric pressure P_{ref} far from the resonator. The inset shows a top view of the SMR tip: exploiting device symmetry allows to simulate only 1-way of the microfluidic channel, thus reducing computational complexity.

Figure 3.4: Mesh of solid and fluid domain. About 8000 hexahedral elements are simulated. A coarser mesh is used for the solid structure, while discretization of the fluid domain is finer in order to resolve the thin viscous boundary layers at fluid-structure interface. The inset shows the SMR tip, and the mesh refinement at the channel walls.

Differently from the analytical model, the developed FEM model needs to be built in 3-D. Simulation of the 2-D geometry results in the eigenshape shown in yellow in Figure 3.5, different from the-mode shape of a singly clamped beam in 1st resonance mode (blue line in Figure 3.5). This happens because the simulation software considers the SMR 2-D geometry as two independent beams connected at the free-end. Building the geometry in 3-D, the additional constraint given by the channel lateral walls allows to obtain the expected mode shape, as seen in Figure 3.6 [82].

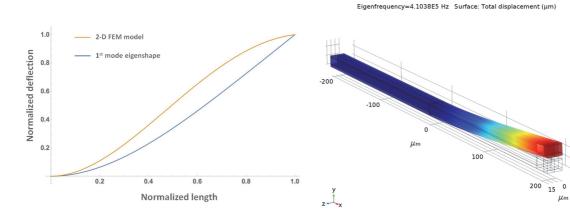


Figure 3.5: First eigenmode of a 2-D simulated geometry. The simulation software considers the 2-D geometry as two independent beams connected at the tip, therefore resulting in the mode-shape shown by the yellow line, different from the one of singly clamped beams in first mode of resonance (blue line). The issue is solved building the geometry in 3-D, where the constraint given by the lateral wall allows to obtain the expected eigenmode (blue line).

Figure 3.6: First eigenmode of 3-D simulated Device B (symmetry exploited). The resonator extends for x>0, while the structure between 0 and L_c represents the channel in the rigid substrate. Including the rigid channel is fundamental in order to study pressure mechanisms taking place inside the resonator.

3.3.2 Boundary conditions and physics

The presented model implements a 3-D eigenvalue study of the solid cantilever with internal fluid. The only energy dissipation mechanism considered is the one deriving from the fluid-structure interaction; hence, no losses in the solid structure, through the clamp or due to the surrounding medium are included.

The *solid domain* is solved using the theory of linear elasticity, assuming small deformations and linear elastic material [89].

Linearized Navier-Stokes equations for viscous, compressible fluid are applied to the *liquid domain*, under the assumption of small perturbations [90].

In order to couple the two physical phenomena and operate on a same reference system, a *multiphysical analysis* based on ALE is conducted: this allows the complex interaction between a stationary background (fluid) and an acoustic field (vibrating solid structure) in the frequency domain. In addition, it prescribes continuity in the displacement field and in the stress field across the boundaries.

Boundary conditions are applied to the solid domain as follows:

- Three-dimensional stresses generated in the fluid domain are applied as a boundary load to the solid domain, at the fluid-structure interface
- The structure placed at $-L_c < x < 0$ is fixed, no vibrations are allowed (see Figure 3.3)
- Symmetry exploited at y < 0 with respect to the yx plane (see Figure 3.3)

Boundary conditions for the fluid domain are listed below:

- Velocity field generated by the solid structure vibration is applied to the liquid domain as a prescribed velocity (no-slip)
- Reference pressure $P_{ref} = 1$ atm applied at the entrance of the rigid fluidic channel (x = 0)
- Symmetry exploited at y < 0 with respect to the yx plane (see Figure 3.3)

3.3.3 Numerical Results

The eigenfrequency analysis returns complex eigenvalues λ :

$$\lambda = \omega - i\delta$$
 Eq. 3.3

where ω is the radial resonance frequency and δ is the system attenuation.

The quality factor is extracted as [71]:

$$Q = \frac{\omega}{2\delta}$$
 Eq. 3.4

Quality factor is studied with respect to the fluid viscosity for the first two vibrational modes of the devices B and C, as shown in Figure 3.7.

In order to validate the model, numerical results are compared with theoretical and experimental values presented by Sader [74, 87]; fluid properties (density, viscosity, compressibility) and solid properties (Young Modulus, Poisson ratio) are selected to be the same of the experimental conditions. Figure 3.7 presents the results of this comparison.

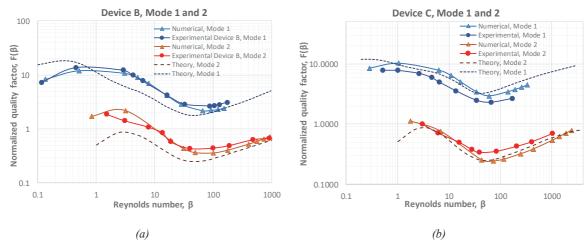


Figure 3.7: Numerical model results. Numerical, theoretical and experimental values are compared for the first two modes of resonance of Device B (a) and (C). Z_0 are estimated to be 0.06 and 0.05 for Device B and C, respectively.

The numerical model is in good agreement with experimental results, for both devices and vibrational modes. In particular for device B, FEM simulations outperform the analytical model in the prediction of experimental results. Nevertheless, the FEM model deviates from theory in the on-axis case at Reynolds numbers below 1, as presented in Figure 3.8. According to theory, in case of perfect symmetry between microfluidic channel and resonator cross section ($Z_0 = 0$), quality factor is monotonically enhanced at very high viscosities (low β) due to the solid-like behavior of the fluid. However, the developed FEM model predicts the opposite trend.

One possible reason of discrepancy between theory and simulations lies in the definition of the fluid medium at extremely high viscosities. In the proposed FEM model the increase of viscosity does not go in parallel with an increase of "fluid stiffness", as no elasticity is associated to the fluid domain. Because of this, the sole effect of increasing viscosity is an increase in energy dissipation. On the other hand, the theory in [74] describes a solid-like behavior in the very high viscosity regime, allowing the fluid to store energy as Reynold number decreases, resulting in a monotonic increase in quality factor.

Whether the medium at high viscosity has to be considered an elastic quasi-solid or an unelastic extremely viscous fluid is an interesting question to be addressed.

Unfortunately, experiments in the extremely low β range are not available to give unequivocal indication of the correct behaviour to be expected. In order to have a feeling of such low Reynolds numbers in real life, Figure 3.9 reports some examples of dynamic viscosity values for known materials as human blood or toothpaste, while Table 3.2 shows Reynolds numbers in the range of Devices B and C.

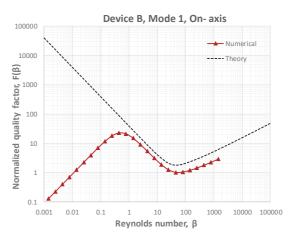


Figure 3.8: Numerical model: result for on-axis case, incompressible fluids. The model fails in predicting the $Z_0 = 0$ case, for $\beta < 1$.

a temperature of 25 C [91].						
Glycerol % in water	Density ρ_f	Viscosity μ_f	Device B, Rey	nolds number 3		, Reynolds ber β
Construction of the state of th	$[g/cm^3] \qquad [mPa \cdot s]$	[mPa·s]	I mode	II mode	I mode	II mode
0	0.998	1.005	151.67	931.15	171.30	1036.63
50	1.126	6	28.64	185.81	6.42	39.24
100	1.261	1410	0.13	0.83	0.51	3.05

Table 3.2: Fluidic properties and corresponding Reynolds numbers used for numerical simulations. In practical applications, this density and viscosity range can be obtained through different mixtures of glycerol and water. Data are given considering a temperature of 25°C [91]

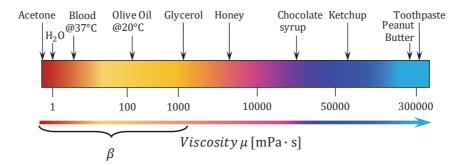


Figure 3.9: Examples of dynamic viscosity values. Biological fluids are in the order of few mPas, while pastes are in the range of 10⁴ mPas [92]. Experimental values of Reynolds numbers analyzed in this work [87] correspond to viscosities between 0.1 and 1000 mPas.

Obtaining experimental data in a lower β regime, considering devices B and C size range, would correspond to operate with fluids as viscous as honey or ketchup. Performing tests with highly viscous materials is extremely challenging: the high fluidic resistance would require enormous pressures in order to introduce the fluid into the microchannels.

Even assuming successful operation of SMRs with such viscous fluids, probing the on-axis case by experiments remains extremely difficult. In fact, achieving perfect symmetry between the bottom and top wall of the fluidic channel ($Z_0 = 0$) is nearly impossible, due to tolerances in thin film depositions or dry etching processes.

3.4 Chapter conclusion

In the presented numerical model SMR devices are simulated through a coupled fluid-structure interaction (FSI) based on linear elasticity and linearized Navier Stokes equations.

The model is well in agreement with theory and experiments presented in literature [74] for the viscositiy range of interest in case of biosensing application (see Figure 3.9). However FEM results are in contrast with theoretical model in the on-axis case at low Reynolds numbers. Unfortunately, due to difficulties in operating SMRs with highly viscous fluids, there are currently no experiments available in this configuration to give unequivocal indication of the correct behaviour to be expected.

Future work will focus on including elasticity in the fluid domain, in order to enable the study of viscoelasticity. Another goal will be to provide a large set of experimental results to be compared to FEM

simulations. In particular, finding a strategy to experimentally probe highy viscous materials with SMRs would be an enormous advantage. Also, the experimental investigation of quality factor dependence on off-axis placement Z_0 [87], would help to further understand the reason of mismatch, at low Reynolds numbers, between FEM simulations and theory proposed by J. Sader.

The interest in validating the numerical model in a wider range of Reynolds numbers is justified by the initial goal of developing a tool for studying complex fluids and different geometries. The long term objective consists in including viscoelasticity in the numerical model and studying the rheometry of complex fluids, with interest not only on biological samples but also on hydrogels and ionic liquids.

Chapter 4

FABRICATION

This chapter presents the details of the fabrication of arrays of transparent SMRs, with integrated PZE electrodes [66]. After a brief overview about the fabrication processes found in literature, the approach developed in this thesis is presented. Optimization of microchannel fabrication, piezoelectric electrodes definition and resonators release are presented, separately. Advantages and limitations of the developed process flow are discussed in each section. Detailed process flow and runcard are provided in Appendix A and B.

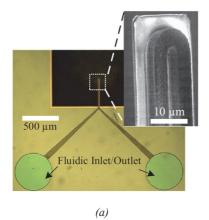
4.1 Introduction

Fabrication of suspended microchannel resonators is a complex and long process that has to meet the requirements of mechanics, microfluidics, and electronics (in case of integrated transduction), as presented in Chapter 2. Materials and geometrical dimensions need to reach both fabrication feasibility and device functionality. For instance, properties such as biocompatibility, chemical stability and hydrophilicity should be taken into account together with thermal budget, residual stress, etching selectivity and fabrication cost.

The different fabrication strategies proposed in literature in the past fifteen years, constituted an invaluable source of knowledge that served as a starting point to the process flow proposed in this thesis. Few of them are briefly described below.

4.1.1 State of the art

The first reported SMR fabrication processes rely on the *long wet etching of a sacrificial material* [49, 93]. In particular, fluidic channels are defined via deposition and patterning of a sacrificial layer (polysilicon) deposited on top of the structural material (silicon nitride) of the resonator. Channels are then sealed with a second silicon nitride deposition. Sacrificial polysilicon removal is achieved defining access holes to the channel interior and immersing the wafer in wet etchant (KOH) for several hours. Within this approach, it is fundamental to carefully choose a structural material that possesses excellent selectivity towards the chemical used to etch the sacrificial material in the channels. Silicon nitride/polysilicon as well as silicon oxide/silicon are good structural/sacrificial material options, considering long wet etching in KOH. This fabrication process allows to obtain fluidic channels extruded from the cantilever base or embedded inside the flat surface of resonators, as shown in Figure 4.1 (a) and (b), respectively. As a drawback, several hours in aggressive chemicals, like KOH, can be detrimental to the wafer integrity.



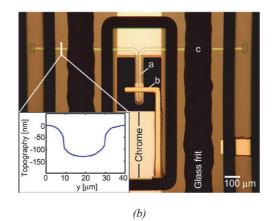
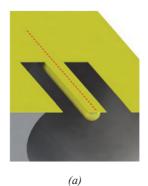


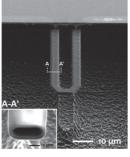
Figure 4.1: SMR sensors obtained from a process flow based on the wet etching of a sacrificial material. (a) Silicon-rich silicon nitride (SRN) cantilever, with extruded fluidic channel on top. Sacrificial polysilicon is removed via 12 hours etching in KOH at 80° C. (Figure readapted with permission from Microelectron. Eng. [93]). (b) Low stress silicon nitride (ls- SiN_x) cantilevers, containing an embedded microfluidic channel. Sacrificial polysilicon is removed via 20 hours etching in KOH at 80° C. Wafer-level packaging is achieved via wafer bonding to a glass wafer, which also provides fluidic and electrical connections. (© 2006 IEEE [94])

Wafer-level vacuum packaging of silicon and silicon nitride devices with integrated electrodes has also been reported in [62, 94]. This is achieved via wafer bonding (glass frit bonding) to a glass substrate separately patterned. Fluidic bypass channels and electrical connections for electrostatic actuation are provided by the glass wafer, while on-chip getters prevent vacuum outgassing.

Another approach to SMR fabrication consists in defining fluidic channels without the requirement of depositing a sacrificial material. Figure 4.2(a) shows a hollow cantilever fabricated defining buried cavities underneath the surface of the wafer, and sealing them with a single deposition of structural material. A first example refers to [95], where dashed apertures (in red) are opened via dry etching, in a silicon-rich silicon nitride (SRN) layer (in yellow) deposited on a silicon wafer. In this case the silicon wafer itself serves as sacrificial material: silicon is etched via isotropic dry etching in SF₆, through the defined apertures. This leads to the coalescence of the etched regions and to the formation of a continuous channel, about 10 µm in diameter. Finally, channels walls are uniformly coated with a single SRN deposition, that also seals the etch apertures. Resonators are patterned and finally released in isotropic SF₆ etching. This technique needs the engineering of dashed apertures distribution and spacing, easily achievable via simulation software or analytical modeling. In addition, it allows an easy and fast fluidic channel definition below the flat surface of the wafer, with etching times in the order of few minutes. However, it reduces the control of the dimensions and geometry of channel and resonator, compared to the previous strategy. For instance, channel dimensions are limited by the ability to control etching rate and uniformity across the wafer.

Another fabrication process that does not require a dedicated sacrificial material and is suitable for smaller scales compared to the previous one, has recently been presented. In [96] *silicon self-assembly* has been used for the fabrication of hollow microtubes within a three-step process. This process, called silicon-on-nothing (SON) is based on the dry etching of cylindrical pores in a standard silicon substrate. The wafer is then annealed at high temperature ($\sim 1000^{\circ}$ C) for about 20 minutes, under a controlled Argon atmosphere. This results in self-assembled buried cavities, with a diameter of 1.8 μ m. Access holes are defined via dry etching and the wafer is later dry oxidized in a furnace to coat channel interior. Resonators are finally released in SF₆ isotropic etching (Figure 4.2(b)). This approach allows a fine tuning of wall thickness and constitutes an easy fabrication process at few μ m size range.





(b)

Figure 4.2: Examples of SMR fabricated without the use of a deposited sacrificial material. (a) Buried channels defined through etch holes patterning and isotropic silicon dry etching of 20 minutes. Channels are coated and sealed with a single SRN deposition. (b) Hollow microtube defined via silicon self-assembly. A pre-patterned silicon wafer is annealed at high temperature under a controlled atmosphere to form self-assembled buried cavities, in about 20 minutes. (Figures are readapted from (a) [95] and (b) [96]).

4.1.2 Fabrication overview: materials and requirements

In this thesis, 250, 500, 750 and 1000 μ m long singly- and doubly-clamped SMRs are fabricated. Resonators are 30 μ m wide and 8 μ m thick, while the target cross section of the embedded channels is 6 μ m x 10 μ m. Channel dimensions are chosen in order to perform experiments with micron-sized analytes such as beads, bacteria or yeast cells. Microfluidic channels span 25%, 60% and 100% of the resonator length, to disentangle mass and stiffness effect on the device resonance frequency, as discussed in Chapter 2. Piezoelectric transduction is integrated on top of each sensor, enabling independent actuation and detection.

The fabrication is based on the etching of a sacrificial polysilicon (PolySi) layer sandwiched between two structural layers of low-stress silicon nitride (ls-SiN_x). The full process flow and runcard can be found in Appendix A and B, respectively.

As already discussed, one of the major drawbacks of fabrication processes based on sacrificial materials is the long etching time (several hours) needed to remove the sacrificial layer from the microfluidic channels. In order to make the etching in KOH faster, the PolySi is doped via POCl₃ diffusion at 1100 °C. It is in fact reported in literature that doped-PolySi has a high etching rate in KOH, twice as fast as undoped polysilicon [97]. The thickness of sacrificial PolySi defines the height of the fluidic channel. Low pressure chemical vapor deposition (LPCVD) allows the deposition of a homogeneous PolySi layer up to 3 μ m. Therefore, with two LPCVD depositions it is possible to reach a thickness of 6 μ m. Few seconds of etching in HF, after each LPCVD step, are necessary to remove the oxide layer (glaze) that is formed during the high temperature annealing in POCl₃ environment [98].

LPCVD process is also used for $ls-SiN_x$ deposition, and allows to obtain nitride layers from few tens of nm to 2 μ m, enabling fine-tuning of the thickness of channel walls. KOH etching is extremely selective to $ls-SiN_x$ allowing, in theory, safe channel emptying [97]. In addition, $ls-SiN_x$ transparency is particularly advantageous: it allows to visually verify the removal of sacrificial material from the channel interior, as well as the silicon substrate below the resonators during release. Furthermore, the choice of a low-stress structural material (~200 MPa tensile stress) is made to minimize residual stress in the fabricated structures, in particular doubly clamped beams, thus avoiding structural buckling or fracture.

The main requirement in the fabrication process is to obtain *microfluidic channels embedded below the surface of the wafer*, which should be as flat as possible in order to allow the deposition of PZE electrodes. Aluminum nitride (AlN), adopted as PZE material, can be deposited via sputtering with a low thermal budget (300°C) and can be easily processed with standard microfabrication techniques. Platinum (Pt) was demonstrated to be an optimum substrate for AlN growth [81]. Also, its processing is compatible with all the fabrication steps and the materials which constitute the device.

Additional fabrication goals are *control* and *tunability* of SMR dimensions and geometries, in order to respect design specifications and be able to investigate analytes of different sizes. Also, *reproducibility* and *high fabrication yield* are desirable to minimize the fabrication duration and cost.

In the next paragraphs, the fabrication of microchannels, PZE electrodes and resonators will be described in detail, with few highlights on the problems encountered and relative solutions.

4.2 Microfluidic channels

The definition of embedded microfluidic channels and fluidic access was the most challenging part in the fabrication of SMRs proposed in this thesis.

Transparent embedded channels are fabricated based on a *trench-technology* that allows the accurate definition of channel walls. To improve mechanical robustness of the channels, *micropillars* are defined inside the fluidic network. The removal of sacrificial polysilicon requires the definition of *fluidic openings* to access the channel interior. To do so, two different configurations are tested and compared: fluidic openings defined from the bottom or the top of the wafer. Finally, results of PolySi etching in KOH are presented, also providing a strategy to reduce the time required for *channel emptying* from few hours to few minutes.

4.2.1 Trenches technology

Figure 4.3 shows the strategy adopted to fabricate microfluidic channels embedded below the surface of the wafer. 500 nm low stress ls-SiN_x, and 6 μ m POCl₃-doped PolySi are deposited on a 4-inch silicon wafer (<100> plane) via LPCVD. Channels walls are defined via the dry etch of high aspect-ratio trenches, 0.6 μ m × 6 μ m, through the polysilicon. An additional LPCVD ls-SiN_x deposition fills the trenches and seals the microfluidic channel, filled with sacrificial material. This paragraph describes the optimization of deep trenches definition, with focus on etching parameters, and discusses fabrication constraints.

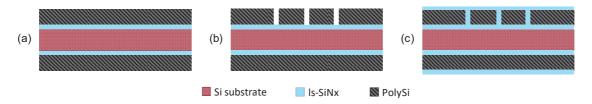


Figure 4.3 First part of SMR process flow, in cross section (not in scale). (a) The process starts from a standard 4-inch Silicon wafer, polished on both sides. The structural ls-SiN $_x$ (0.5 μ m) and the sacrificial PolySi (6 μ m) are deposited via low-pressure chemical vapor deposition (LPCVD), at high temperature (1100°C). (b) Microfluidic channels are defined via the dry etch of high aspect-ratio trenches, 0.6 μ m × 6 μ m, through the sacrificial polysilicon. (c) An additional LPCVD ls-SiN $_x$ deposition fills the trenches and seals the microfluidic channel [66].

Considering a channel thickness (PolySi layer) of 6 μ m, the goal for trenches dimensions is set to 0.6 μ m in width and 6 μ m in height. This results in an aspect ratio (thickness/width) of 10, within the range achievable with dry etching techniques available in the Center of Microtechnology (CMi) at EPFL. Since 0.6 μ m is below the resolution limit of standard photolithography (\sim 1 μ m), channel geometry is defined via e-beam lithography (Vistec EBPG5000). In order to promote resist adhesion, the wafer is subjected to 5 min O₂ plasma at 600 W, followed by wafer dehydration for 3 minutes at 183°C. The substrate is spin coated at 750 rpm for 5 min, using ZEP520A resist (diluted in Anisole with 1:1 ratio), which results 280 nm-thick. Resist is baked for 5 minutes at 183°C, and the wafer is exposed using 200 μ C/cm², 150 nA current and a beam spot size of 70 nm. The wafer is developed for 1 min in Amyl Acetate and rinsed for 1 min in a solution of MiBK:IPA (90:10). The first ebeam lithography (EBL1) defines not only channel walls, but also stiffening structures and insulating lines, shown in Figure 4.4. As described in Chapter 2, stiffening structures are included around resonator clamp to increase structural robustness after

release, while insulating lines are placed in between adjacent electrical tracks to limit electrical losses through the substrate.

EBL1 pattern is transferred to the underlying sacrificial layer via dry etching of PolySi. This step demanded significant optimization, as it requires to (i) keep the width of the obtained trench as close as possible to the designed one (0.6 μ m), (ii) reach and stop at the bottom ls-SiN_x and (iii) give a uniform result across the wafer. These are necessary requirements to ensure proper channel sealing. PolySi is etched in fluorine-based chemistry, and both continuous and pulsed etching processes are tested.

We first tried *continuous etching* in c- C_4F_8 and SF_6 environment (SF_6 40 sccm, c- C_4F_8 55 sccm, at 1500 W) with Si opto recipe at Alcatel AMS 200.

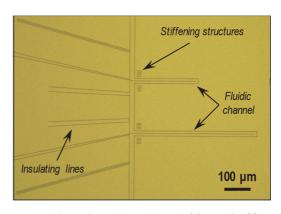


Figure 4.4: Optical microscope image of the result of first ebeam lithography (EBL1). The design is entirely made of 0.6 µm-wide lines, which define channel walls, stiffening structures and insulating lines.

The result of this process after 6'30" etching is presented in Figure 4.5(a), which shows the cross section of a cleaved wafer. Trenches present smooth walls, but the overall width is not uniform along the 6 µm depth. The top aperture is about 0.9 µm-wide, while at half etching depth it reaches a width of 1.4 µm. Also, all the results present a narrowing after an etching depth of about 4 µm, the reason of which is not clear. The trench is filled through a single ls-SiNx deposition via LPCVD, that needs to be at least half of the trench width, in order to ensure proper sealing. To be conservative and take into account etching or exposure non-uniformity across the wafer, a thickness of 700 nm is chosen (more than twice the minimum value required). Indeed, deposition of a thinner layer constitutes a high risk (time and cost), because many other steps need to be performed before having the confirmation of trench sealing all over the wafer. The only way to check trench dimensions (height and overall width) is to cleave the silicon substrate and inspect it with a scanning electron microscope (SEM). Clearly, this would destroy the wafer, and it would only provide accurate information regarding the few cross sections observed. In fact, due to rough surface of the amorphous polysilicon layer, trenches present an irregular profile along their length, as visible in Figure 4.6. The actual confirmation of trench sealing is given during channel emptying, which occurs several steps further in the process flow: if the PolySi is etched only within the channel walls, it means that ls-SiN_x trenches are well attached to bottom nitride layer and provide successful fluidic confinement. In this case, fabrication sets a constraint to the thickness of channel top wall.

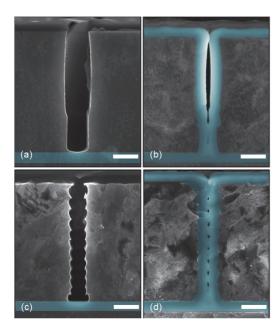
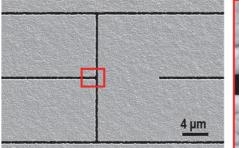


Figure 4.5: Comparison between trenches defined via continuous (top row) and pulsed dry etching (bottom row) [66].(a) Continuous etching in C_4F_8 generates trenches with smooth walls, but the initial width defined by e-beam lithography (0.6 μm) results larger (~1.2 μm). (b) After filling with 700 nm ls-Si N_x (colored in light blue), the top and bottom of the trench are closed, but a cavity runs through the structure thickness. (c) Trench defined by Bosch ® process in c- C₄F₈ and SF₆. Despite corrugated walls (scalloping), the average width results constant through the trench height and closer to the initial value set by e-beam. (d) After the deposition of ls-SiN_x (700 nm), the structure is uniformly filled from the top to the bottom edge. The residual empty volume is much lower compared to case (b) and this is assumed to provide more robustness to the trench. Scale bars are 1 μ m.

The second strategy tested was pulsed etching of polysilicon, and results are presented in Figure 4.5(c,d). In this case, trenches are defined via Bosch ® process etching, where two etching steps are repeated in cycles. A first active step in SF₆ provides isotropic etching. A second (inactive) step in c-C₄F₈ deposits an inert passivation layer, which protects the lateral walls from the next etching cycles. Number of cycles and duration of these steps are optimized according to the requirement listed above. In addition in this case, the lateral walls present corrugations (scalloping) generated by the isotropic etching in SF₆. Etching parameters are optimized in order to obtain a large number of small cycles, so that the overall width of the trench remains constant along his length, and close to 0.6 µm [99, 100]. In particular, the best results are obtained with 13 cycles of 7 s each, constituted of 5 s SF₆ (300 sccm) and 2 s c-C₄F₈ (200 sccm). The optimized results obtained via Bosch ® process etching can be seen in Figure 4.5 (c,d), while few additional details about etching optimization are shown in Figure 4.7 and Figure 4.8. Due to the isotropy of the SF₆ etching step, trench width results larger than the value defined with EBL1. However in this case, the overall width of the trench remains constant along all its length and equal to about 0.8 μm in average, thanks to the passivation layer that prevents the etching of lateral wall. After deposition of 700 nm of ls-SiN_x, the structure appears more robust and the ratio between empty and filled volume is lower compared to the previous case (continuous silicon etching). Therefore, Bosch ® process etching is chosen as strategy for highaspect ratio trenches definition.

A typical microfluidic channel after trench filling and resist strip (5 min O_2 plasma at 600 W) is shown in Figure 4.9. Channel target dimensions were set to 5 μ m \times 10 μ m in cross section, and to about 0.6 μ m for the walls. After fabrication the bottom wall is 0.5 μ m- thick, while lateral and top walls are 0.8 μ m- and 0.7 μ m-thick, respectively. The PolySi inside the channels is 9.8 μ m- wide, due to trench widening during the etching. The thickness is about 5.9 μ m, due to the deglaze in HF after each PolySi doping step, which removes the thin oxide layer generated during the doping in POCl₃ at 1100°C. In order to remove the sacrificial PolySi from the channel, fluidic access needs to be defined, as discussed in the next paragraph.



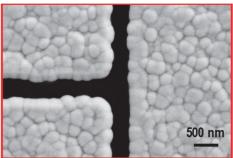


Figure 4.6: SEM image of a trench pattern etched through polysilicon (top view). Trenches width is irregular due to the grain structure of amorphous polysilicon. The inset shows a T-junction, where the overall width results larger than the one of straight patterns. This has to be taken into account to ensure complete trench sealing.

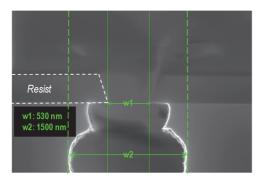


Figure 4.7: SEM image of a trench cross section before resist strip in oxygen plasma. The white dashed-line points the attention to the resist profile. Despite a minimum aperture of 530 nm (written via ebeam lithography), trench width results up to three times larger. This is given by the isotropy of SF₆ etching process and sets a limitation to the minimum thickness of channel top wall.

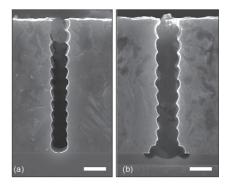


Figure 4.8: Bosch ® process optimization: example of trench underetching (a) and overetching (b). The two trenches are etched using the same number of cycles (12 cycles), but with shorter and longer SF_6 steps (4 s, in (a), 7 s in (b)). The passivation step is kept constant to 2 s. The trench in (a) does not reach the bottom nitride layer, due to insufficient number of etching cycles. In (b), the trench results wider and the bottom nitride is damaged by the overetching.

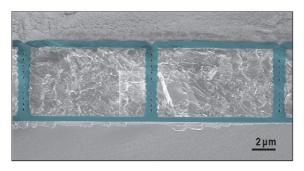
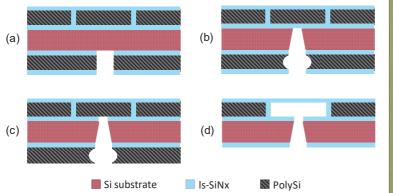


Figure 4.9: Microfluidic channel fabricated via trench technology and filled with sacrificial PolySi. Trenches are defined via Bosch ® process etching and filled with 700 nm LPCVD ls-SiN $_x$ (colored in light blue). The etching parameters have been optimized to 5 s SF $_6$ (300 sccm) and 2 s c-C $_4$ F $_8$ (200 sccm), effectively finding a tradeoff between the number of etching cycles and the surface corrugation (scalloping radius) [66, 100].

4.2.2 Opening from the bottom

The first approach adopted to provide fluidic access and achieve channel emptying consists in opening through-holes from the backside of the 380 µm-thick double sided wafer. This configuration is advantageous because it leaves the top surface of the wafer free for visual inspection and vacuum encapsulation. Also, the backside of the wafer is robust and does not contain released structures, thus simplifying and giving more freedom in assembling fluidic connections. Figure 4.10 shows the process flow of backside opening definition via a combination of dry and wet etchings, continuing the fabrication shown in the previous paragraph (Figure 4.3). The schematic in Figure 4.10 represents the cross section taken at the SMR inlet seen in Figure 4.11, that were initially designed larger than the ones presented in Chapter 2.



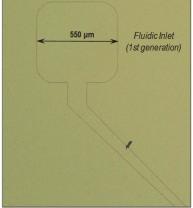


Figure 4.10: Schematic of the process flow for fluidic openings from the wafer backside (not in scale). The drawings represent a cross section of the wafer, at the fluidic inlet.

Figure 4.11: Squared 550 μ m × 550 μ m inlet, designed in the first generation of devices.

The first process step (Figure 4.10(a)) consists in the definition of 700 $\mu m \times 700$ μm squared opening in the wafer backside. The structures are defined via photolithography and aligned to the EBL1 pattern, using 5 μm -thick photoresist AZ ECI. Follows a combination of dry etching processes at Alcatel 601E to transfer the photoresist (PR) pattern to ls-SiN_x/PolySi/ls-SiN_x. In particular, ls-SiN_x is etched using a continuous C₂F₆-based program (Nitrure_1), while PolySi is etched via the same Bosch ® process etching described in the previous paragraph. Etching rates are given in Table 4.1.

Table 4.1: Etching rates and chemistry used for ls-SiNx and PolySi dry etching at Alcatel 601E. Photoresists etching rates are also given.

Material	Program	Chemistry	Etching rate [nm/min]
Polysilicon	Aniso_ADP	Bosch process (SF ₆ /C ₄ F ₈)	4500
ls-silicon nitride	Nitrure_1	C_2F_6	280-300
PR AZ ECI	Aniso_ADP	Bosch process (SF ₆ /C ₄ F ₈)	130
PR AZ ECI	Nitrure_1	C ₂ F ₆	300

The wafer is then immersed in KOH (40% by weight) at 80° C, to etch through the silicon wafer and reach the ls-SiN_x layer that defines the bottom wall of microfluidic channels (Figure 4.10(b) and Figure 4.13) [101]. An

etching rate of 90 μ m/h allows to conclude the process in less than 5 hours, followed by 2 hours in HCl for potassium decontamination. On a <100> plane-oriented silicon wafer, KOH anisotropic etching through a square mask produces pyramidal structures with a slope of 54.7°, as shown in Figure 4.13. This is due to the etch-rate difference between <100> and <111> planes [102]. Considering a 380 μ m-thick wafer and a square aperture of 700 nm, the bottom plane aperture is expected to be equal to 160 μ m, calculated as in Figure 4.12.

In order to have access to the channels, the 500 nm-thick ls- SiN_x bottom wall is removed in dry etching. The etching time is set to double the one necessary to etch 500 nm, to take into account the etching across the thickness of the wafer through narrow apertures. In this step, the nitride layer at the wafer backside is also removed (Figure 4.10 (c)). The wafer is then immersed in KOH 20% (by density) at 90° C, which results in a measured PolySi etching rate of $125 \mu m/h$. During the etching, a magnetic rod is kept in rotation in order to ensure solution recirculation, and avoid etching saturation in the microfluidic channels. Considering the length of the longest fluidic channel being about 12 mm (Complete Chip design, longer array), channel emptying is achieved in 24 h etching (Figure 4.10(d)). During the etching, a protective layer (ProTEK B3, from Brewer Science) is spin coated on the top of the wafer, to avoid damaging of the top nitride layer. In addition, a Teflon chuck specifically designed to prevent contact between KOH and substrate (top face) is used. Finally, 2 hours of decontamination in HCl and a careful rinse in water and Isopropyl Alcohol (IPA) conclude the fabrication of microchannels. ProTEK layer can be removed in oxygen plasma (10 min at 600 W).

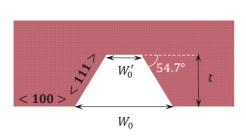


Figure 4.12: KOH etching of a <100> - oriented silicon wafer. KOH anisotropic etching through a square mask produces pyramidal structures with a slope of 54.7°[102]. The bottom aperture size can be calculated as $W_0' = W_0 - 2 \times t/\tan(54.7^\circ)$, where t is the etching depth.

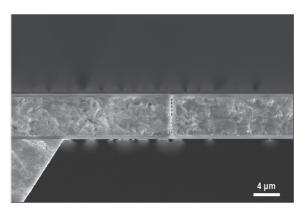


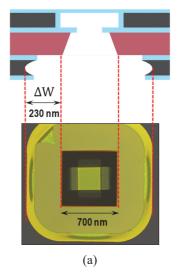
Figure 4.13: Suspended microfluidic channel filled with PolySi, after 5 hours of anisotropic etching in KOH.The Is- SiN_x , which constitutes the channel bottom wall, acts as a stop layer to KOH and needs to be removed via dry etching. On the left of the image it is possible to see the silicon <111> plane having a slope of 54.7° with respect to the wafer top surface.

This fabrication process based on backside fluidic access has two main issues, that cause the fluidic openings dimensions to be up to 2 times larger than the ones set via design.

The underetch of backside PolySi occurring during the etching in KOH (5 hours) of the silicon wafer. This causes the backside openings (before channel emptying) to result 1.5 times larger than the ones defined via dry etching, as shown in Figure 4.14. When the PolySi is etched, the lowest ls-SiN_x layer remains hanging and eventually breaks. This leaves the ls-SiN_x in contact with the silicon wafer unprotected. As a result, the dry etching that removes the channel bottom wall also removes both ls-

- SiN_x layers on the backside. Thus, the mask opening for KOH is not the one defined via photolithography, but is defined by PolySi underetching. After channel emptying, backside openings are up to 2 times larger than photolithography defined (Figure 4.14 (b)). This makes the wafer and the suspended structures very fragile. This issue was easily solved by removing the backside ls-SiN_x and PolySi via dry etching, before the photolithography of backside apertures.
- 2) Silicon <111> plane etching is 100 times slower (1.7 μ m/h) than <100> plane (90 μ m/h). However, it needs to be taken into account in the design, when performing etching of several hours. In fact, assuming an etching of 24 h, the fluidic openings will result 80 μ m larger, compared to calculations that only account for plane <100>.

Applying the corrections just discussed, it is possible to achieve successful channel emptying, as shown in Figure 4.15.





(b)

Figure 4.14:Optical image of the backside of a wafer before channel emptying. As represented in the schematic on top, the underetching of PolySi causes the overhang of the lowest ls-SiNx layer. This layers breaks and detaches, leaving the lower ls-SiNx exposed. As a collateral effect, during the nitride dry etching to access the channels, both the backside nitride layers are also removed. A much larger silicon area is left exposed to KOH compared to the one defined via photolithography and dry etching. This causes the fluidic access to result more than 2 times larger than design, making the chips more fragile (b). This problem is solved removing the backside ls-SiNx and PolySi layer before the photolithography.

Microfluidic channels were tested, without continuing the process flow, to verify that they had been emptied and to check their functionality. At first, a droplet of DI water is applied at one inlet with a pipette, and observed flowing through the channels due to capillary forces. This confirms that the ls-SiN_x is hydrophilic and that the trench technology is successfully confining the fluid inside the channel. Subsequently, a simple PDMS block with punched through holes spaced as the fluidic openings is bonded to the wafer backside, via O_2 plasma. A differential pressure between inlet and outlet is applied with a fluidic pump, starting at 10 mbars and increasing the value to verify the robustness of the ls-SiN_x. The maximum applicable pressure before the inlet membrane breaks is 160 mbar, which corresponds to a flow of $0.010 \,\mu$ l/min, considering DI water in the long array (750 μ m-and 1000 μ m-long SMRs) of a Complete Chip design.

This value is not good enough in order to perform tests with viscous samples, where larger fluidic pressures are required, due larger fluidic resistance.

The preliminary characterization of fluidic channels highlights their limitations, such as the fragility of silicon nitride membranes. Fabrication yield is very low, below 50%, due to wafer damage during the long etching in KOH at high temperature. Despite the use of ProTEK and Teflon chuck, after many hours the KOH solution enters in contact with the wafer and attacks its edges. This makes the wafer very fragile and next fabrication processes become extremely challenging. Another reason of low fabrication yield is the geometry on inlet membranes: being 550 µm-wide and 0.7 µm-thick, most of them break during the processes in wet environment. This inlet design is thus abandoned, new inlets will be presented in the next paragraph. Also, in order to simplify the process flow and reduce the number of steps, fluidic openings are opened from the top of the wafer.

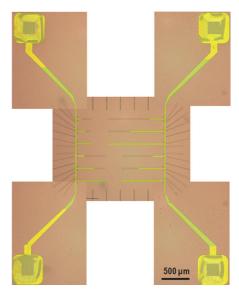


Figure 4.15: Collection of optical microscope images showing a Complete Chip design, first generation. The design of SMRs is the same presented in Chapter 2, while fluidic inlets and channels connecting inlets to resonators are considerably larger. Also, no micropillars are included in this chip. For all these reasons, the channels result extremely fragile and break applying a pressure difference between the inlets, above 160 mbar.

4.2.3 Opening from the top

One of the major drawbacks of fluidic openings from the backside is the complication in the process flow: before patterning the etch squares via photolithography, two dry etchings need to be performed (ls-SiN $_x$ /PolySi). After the photolithography, three additional etchings are required (ls-SiN $_x$ /Si wafer/ ls-SiN $_x$), and finally 24 hours etching in KOH for channel emptying. Apart from the cost of this procedure, it makes the channel definition many days long and extremely complex.

Therefore, another simpler approach is tested: opening fluidic access from the top of the wafer, with one lithography and one etching step, shown in Figure 4.16(a). Since the backside of the wafer is not processed, it is not represented in the schematic, for simplicity. This strategy simplifies and reduces fabrication steps. However, interfacing the chip with experimental setup, results more complicated, as will be discussed in Chapter 5.

Photolithography and ls-SiNx dry etching are performed as already discussed in the previous paragraph. Concerning channel emptying in KOH, one major difference within this approach, is that the top surface of the wafer cannot be protected anymore, and stays exposed to KOH for the whole duration of the etching.

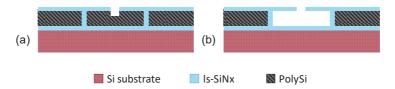


Figure 4.16: Fluidic openings from the top of the wafer can be defined with one lithographic and one dry etching step (a), followed by the long wet etching in KOH for channel emptying (b). For simplicity, the backside of the wafer is not represented.

4.2.3.1 CHANNEL EMPTYING FROM INLETS

At first, the simplest process is tested, consisting in the definition of inlet apertures, and etching in KOH 20% at 90°C for 24 hours. ProTEK B3 is manually applied only on the edges, and the wafer is clamped in the Teflon chuck, to prevent the lateral silicon etching. *Pin-holes in Is-SiN_x* start to be visible (by eye) after about 10 hours of KOH etching. This phenomenon is known from literature, where LPCVD Is-SiN_x is used as hard mask for KOH in combination with other layers like parylene or PECVD SiN, to prevent pin holes [97]. Figure 4.17 presents the picture of a wafer after 24 hours etching in KOH. The solution infiltrates through the layers and etches the sacrificial PolySi, causing nitride delamination all over the wafer.

Clearly, a protective layer is needed. A tentative is made with parylene C, 2 µm-thick, deposited via LPCVD at room temperature. A silanization step is included just before deposition, to promote film adhesion to the substrate. Parylene is a very well-known protective layer for KOH etching, that can be easily patterned via photolithography and etched via oxygen plasma [103]. Unfortunately, the result after 24 hours in KOH is still very similar to Figure 4.17. KOH penetrates from the borders of the wafer, in between parylene and substrate. This happens after about 8 hours of etching, despite the use of the Teflon chuck. Parylene slowly detaches from the substrate, and remains floating in the KOH solution, while the wafer is left unprotected.

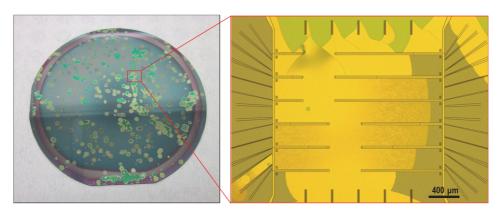


Figure 4.17: Wafer after 24 h KOH, with the top surface exposed to the etching. Pin holes in the ls-SiNx are visible after about 10 hours of etching. KOH penetrates through the pinholes, reaching the bottom PolySi and damaging the channels, as shown in the picture to the right.

Due to the numerous problems encountered during the long KOH etching at high temperature, a different strategy is adopted, in order to avoid this step, as explained in the next paragraph.

4.2.3.2 CHANNEL EMPTYING FROM ADDITIONAL APERTURES

The reason of the need of a 24 h-long etching, is that the KOH has only two access points to etch a ~12 mm-long fluidic network. The idea in this section is to provide several access points to the etching solution. While trenches delimitate channel lateral walls, a strategy similar to the one discussed in paragraph 4.1.1. (buried channels) is adopted for channel emptying. This provides tunable and accurate channel definition and, at the same time, fast sacrificial layer removal. In addition, this generation of devices includes micropillars inside the microfluidic channel, defined together with trenches via EBL1. The design of fluidic inlets is also modified, decreasing their surface and using the geometry described in Chapter 2. All these improvements contribute to the successful fabrication of embedded fluidic channels, as explained in detail below.

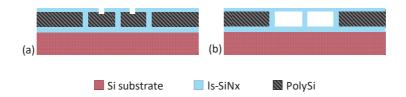


Figure 4.18: Channel emptying from the top of the wafer is achieved defining dashed-line apertures along the channel length. Channels are emptied in KOH within few minutes, and the top surface of the channels is sealed with a single LPCVD of ls- SiN_x .

The process steps adopted for the definition of discontinuous apertures is very similar to the one developed for the trench technology. A hard mask is deposited on the wafer, made of 500 nm amorphous silicon sputtered at room temperature. A second e-beam lithography (EBL2) and a C_2F_6 -based dry etching define 0.6 μ m-wide and 10 μ m-long apertures in the top ls-SiN_x (Figure 4.18(a) and Figure 4.19). After etching, apertures have an average width of 1 μ m, etching rates are given in Table 4.2.

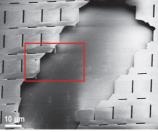
Table 4.2: Measured e	etching rates of ls-SiNx.	amorphous silicon i	(hard mask) and ZEF	Presist in Nitrure 1	etchino

Material	Program	Chemistry	Etching rate [nm/min]
Amorphous silicon	Nitrure_1	C_2F_6	150
ls-silicon nitride	Nitrure_1	C_2F_6	280-300
ZEP	Nitrure_1	C ₂ F ₆	360

Same resist and exposure parameters discussed in paragraph 4.2.1 are used. The etched apertures are 15 µm apart from each other and enable the selective access of wet etchant into the microfluidic channel. The dimensions of dashed lines are chosen as a function of the already known parameters (same width of trenches previously defined), and in order to prevent membrane rupture. As shown in Figure 4.20, placing many apertures close to each others causes the fracture of ls-SiNx membrane during channel emptying, despite micropillars supporting the structure. PolySi is quickly removed from inside the channels by immersing the wafer in an aqueous solution of KOH (40% weight) at 80°C for 25 minutes. POCl₃ doping increases the etching rate of PolySi in KOH, to about 1.5 µm/min, compared to 0.67 µm/min reported in literature for the same conditions [97]. Since KOH is completely confined by the ls-SiNx walls, the etching can be extended by few minutes in order to ensure channel emptying all over the wafer, with no risk of over-etching or wafer damage. In addition, the duration of the etching

does not depend on the channel length, enabling the simultaneous definition of multiple SMR arrays of different lengths. Figure 4.21 and Figure 4.22 show the results of channel emptying with this technique.





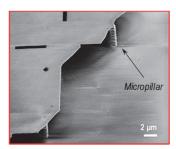


Figure 4.19: SEM image of microfluidic channel, showing the geometry of the dashed apertures, defined via the second e-beam lithography (EBL2). Lines are 0.6 µm-wide and 10 µm-long, and are placed 15 µm apart from each other.

Figure 4.20: Example of nitride membrane break due to the inefficient distribution of etch apertures. Positioning the openings too close to each other causes cracks and rupture along their profile. The inset shows a ls-SiNx micropillar, which connects bottom and top channel walls to make the structures more robust.

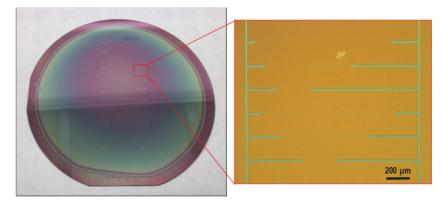
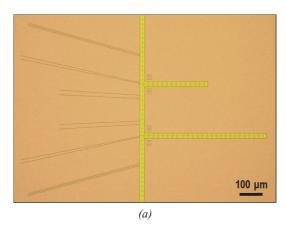


Figure 4.21: Wafer conditions after channel emptying via top apertures. Etch openings allow to reduce the etching time to 25 minutes in KOH solution (40% by weight) at 80°C. The obtained yield is larger than 95%, and the wafer does not present any damage. A Complete Chip design with empty channels, is shown to the right.



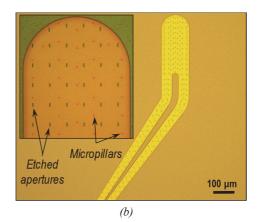


Figure 4.22: Results of channel emptying from the top through etch apertures. (a) a 250 µm- and a 500 µm-long channel are shown. Thanks to the transparency of ls-SiNx, it is possible to see a difference in color between hollow and PolySi-filled regions. (b) Inlet dimensions and shape are modified in order to increase the top membrane stiffness and prevent rupture. The inset shows micropillars and etch apertures in detail. These channels are able to withstand a pressure difference up to 2 bars between inlet and outlet.

After potassium decontamination in HCl for two hours, a final deposition of 700 nm ls-SiN_x provides sealing of the emptied fluidic channels, shown in cross section in Figure 4.23. After this step, it is important to make sure that EBL2 apertures are actually sealed, by inspecting the wafer at SEM (Figure 4.25). In fact, if apertures are not perfectly closed, this would result in a leakage during fluidic experiments.

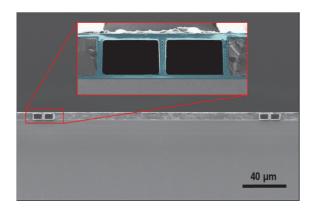


Figure 4.23: Cross section of a cleaved wafer, showing two u-shaped microfluidic channels below the flat surface of the wafer. In the inset, it is possible to see the defined trenches, which constitute the channel walls in ls-SiNx (colored in light blue).

This process flow results successful and allows to fabricate embedded microfluidic channels with a yield larger than 95% in only 25 minutes etching. The top surface of the wafer is maintained flat and the wafer does not undergo any damage. Inlet design is modified according to what presented in Chapter 2. As will be further discussed in Chapter 6, fabricated channels are able to withstand a pressure difference of more than 2 bars between inlet and outlet [66].

The major drawback of this technique is the *thickening of channel walls* during the filling of etched apertures. Before enough material to close the apertures is deposited, LPCVD provides a conformal ls-SiN_x deposition also inside the channels, as shown in Figure 4.24. The thickness of internally-deposited nitride is equal to half the aperture width. Considering an obtained width of 1 μ m, this translates into a thickening of the channel by 0.5 μ m on each wall, thus resulting in a final cross-section of 5 μ m × 9 μ m. This causes an increase by 25% in SMR mass and by 50% in SMR stiffness, with respect to the calculations presented in Chapter 2 (where a 1.4 μ m —thick top wall, but no internal nitride, was considered). In addition, the last ls-SiN_x deposition increases the thickness of the channel top wall to 1.4 μ m. Considering the two LPCVD steps and the internal nitride deposition, the top channel wall results ~2 μ m-thick, 4 times larger than the initial target. To reduce this value, EBL1 and EBL2 design can be modified, for example writing 0.3 μ m-wide lines instead of 0.6 μ m. This makes the etching slightly more difficult, because the trench aspect ratio is doubled, but not impossible. 300 nm-wide lines have been written, resulting in ~550 nm-wide apertures, filled by 300 nm ls-SiNx. However, after many attempts the conclusion is that, in order to survive KOH etching, a minimum ls-SiNx thickness of 600 nm is necessary, considering the current fluidic design. An example of channel break due to a thin nitride membrane (300 nm) is given in Figure 4.26.

Our preferred solution consists in reaching the end of the proposed channel process flow, and later thin down via dry etching the top ls-_{SiNx} wall. This wall can be safely thinned down by half the thickness of the last LPCVD ls-SiN_x (350 nm). Continuing to etch after this point could re-open the EBL2 apertures. On the other hand,

the internal nitride allows to thin down for few nm more, until reaching a total nitride thickness of \sim 1.4 μ m. The thin-down etching is performed via Ion Beam Etching (IBE) at Veeco Nexus IBE 350, using the Medium program which gives a ls-SiN_x etch rate of 36 nm/min. IBE is chosen because of its high etch uniformity across the wafer, equal to 1%. After this step, an additional SEM inspection is necessary to make sure that EBL2 apertures are still sealed, as shown in Figure 4.27. As a final remark, instead of thinning down the nitride from the whole wafer, the ideal strategy would be to add a photolithography step in order to only reduce the top channel thickness at resonator level, while the overall top membrane robustness is maintained. As will be explained in Chapter 5, fluidic connections from the top surface of the wafer require the inlet channels to be as robust as possible.

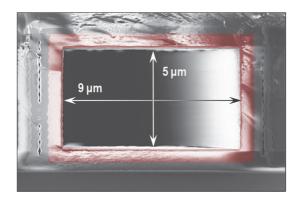


Figure 4.24: During the filling of EBL2 etch apertures via LPCVD process, ls-SiNx is also deposited in the inside of the fluidic channel. This results in an increase in SMR mass and stiffness by 25% and 50%, respectively. The internal nitride layer is shown in red.

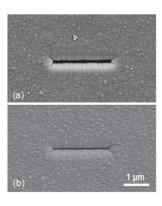


Figure 4.25: SEM inspection of EBL2 etch apertures, after ls-SiNx deposition. In (a) the opening is not well sealed and will cause fluid leakage during experiments. (b) Example of filled opening, that ensures liquid confinement inside the embedded channels.

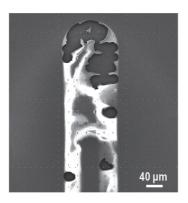


Figure 4.26: 300 nm top ls-SiNx does not confer enough robustness to the inlet membrane to survive the KOH etching. The inlet cracks and breaks apart during the wet process.

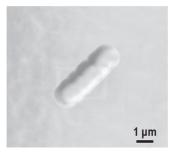


Figure 4.27: SEM inspection of a ls-SiNx filled aperture at SEM, after nitride thin-down in IBE etching. The structure results still sealed, while the PolySi surface is smoothed by the etching.

4.3 Piezoelectric electrodes

The fabricated microfluidic channels lie underneath the flat surface of the wafer and are mechanically strong, hence withstanding further microfabrication processes. The devices developed in this thesis are integrated with piezoelectric (PZE) transduction on top of each resonator. As explained in Chapter 2, PZE electrodes extend

for one fifth of the total resonator length, as a trade-off between transduction efficiency and visual access to the channels. This is achieved with the fabrication of PZE electrodes in Aluminum nitride (AIN) and Platinum (Pt), via sputter deposition, photolithography and dry etching, as shown in Figure 4.28. This section provides details about the electrode fabrication and describes the issues encountered during optimization of the process.

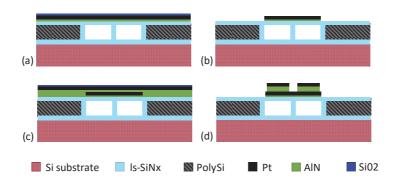


Figure 4.28: Process flow for PZE electrodes fabrication on top of embedded fluidic channels. AlN/Pt and SiO₂ layers are sputtered at 300 °C and room temperature, respectively, and patterned via photolithography and Ar-Cl₂ etching (b). The same process is repeated (c,d) to define the top stack. 300 nm AlN and 25 nm Pt constitute the PZE active layer and the top electrode, respectively. SiO₂ serves as protection to prevent PR diffusion in the Pt films. Each resonator has two independent top electrodes, one for actuation and one for readout.

The first process step for PZE electrode fabrication starts with a DC-pulsed sputter deposition of 15 nm AlN, 25 nm Pt and 20 nm silicon oxide (SiO₂), as shown in Figure 4.28(a). All material targets are cleaned before starting the depositions, using a dedicated cleaning recipe (Runcard in Appendix B). In addition, a test AlN deposition of 5 min is performed on a dummy wafer to check that the process power is all forwarded to the substrate, with no reflections. The sputtering process at 300°C includes a first step of thermalization (5 min), to stabilize the temperature of the wafer. The second step consists in 1 minute plasma etching in Ar environment to clean and prepare the wafer surface. Deposition parameters are reported in Table 4.3. The first AlN film is a seed layer and has the function to promote the c-axis oriented growth of the active AlN layer, as explained in Chapter 2.

Table 4.3: Deposition parameter at Pfeiffer Spider 600, for AlN, Pt and SiO₂.

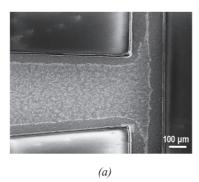
Material	Program	Temperature [°C]	Gas flows [sccm]	Power [W]	Deposition Rate [nm/min]
AlN	AlN T D-1	300	40 (N ₂)/10 (Ar)	1500	50
Pt	_Pt_T_D_Etch_D1	300	15 (Ar)	1000	270
SiO ₂	SiO2_F	RT	15 (Ar)	1000	20

The bottom stack is patterned via photolithography using 2 µm-thick AZ ECI photoresist. The wafer is exposed at Heidelberg MLA150 using a dose of 150 mJ/cm² and a laser wavelength of 405 nm. The result after development is shown in Figure 4.30. This pattern (layer n. 3) is aligned with respect to the trench pattern defined via EBL1 (layer 1) to maximize the symmetry between channels and bottom electrode. The PR pattern is transferred to the underlying layers via dry etching at the STS Multiplex ICP (Inductively Coupled Plasma), in chlorine chemistry. Etching rates are given in Table 4.4. End point detection (EPD) helps to stop the etching at the

bottom ls-SiN_x, together with visual inspection and conductivity check between adjacent tracks with a multimeter. The photoresist is removed via a combination of O₂ plasma and wet etching (UFT 1165 remover), as reported in detail in the runcard in Appendix B. SiO₂ layer is finally etched in buffered hydrofluoric acid (BHF 7:1) for 1 minute. The function of the oxide layer is to prevent the contact between photoresist and Pt layer, which would leave PR residues on the Pt that we have been unable to remove, thus compromising the growth of active AIN. Figure 4.29 shows the comparison of a photolithography on Pt, with and without using the protective oxide layer. Subsequently, the top stack is deposited: 300 nm AlN (active PZE layer), 50 nm Pt and 20 nm SiO2, using the same parameters presented in Table 4.3. A thicker layer of Pt is used as top electrode to increase the mechanical robustness in vision of the wire bonding to custom PCB, as will be explained in Chapter 5. Photolithography and dry etching of the top contact pattern, as well as PR strip and oxide etching, follows the same procedure and parameters already used for bottom definition. The result after photolithography is shown in Figure 4.30(b). In this case, the top pattern (layer 4) is aligned to the bottom electrode geometry (layer 3), to avoid short-circuit between misaligned Pt layers. Electrical insulation between electrical tracks is verified via measurements at the Süss PM8 Manual Probe station. More than 85% of the probed electrodes show a resistance between bottom and top Pt above 10 M Ω , while sweeping the applied voltage from 1 to 5 V. The crystal orientation of AlN layer is verified via XRD measurements: the film possesses a FWHM of about 3.5. The FWHM of the same PZE stack on a Si+ls-SiNx substrate shows a value equal to 2.09, which demonstrates that the rough surface of PolySi has an impact on the growth orientation of AlN. Measurements of PZE transduction efficiency will be presented in Chapter 6.

Table 4.4: Etching parameters at STS Multiplex ICP for AlN, Pt and SiO2 etching.

Material	Program	Gas	Flows [sccm]	Coil Power [W]	Etching Rate [nm/min]
AlN				_	~250
Pt	AlN_etch	Cl_2	20.0±99%	800	~25
SiO ₂		Ar	5.0±10%	_	~70



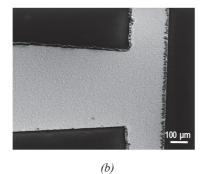
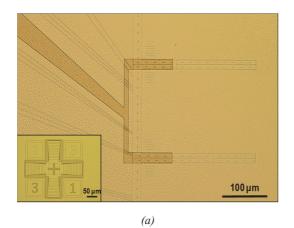


Figure 4.29: Comparison between a Pt layer patterned without (a) and with (b) the protective SiO₂ layer. Photoresist diffuses through the Pt layer during photolithography and etching, and becomes very difficult to remove. Interposing a SiO₂ layer between Pt and PR allows to obtain a clean Pt surface.

PZE electrodes are successfully fabricated, and the dielectric properties of AlN are positively verified. The main problems encountered and the relative solutions are reported below. The first generation of devices was designed as shown in Figure 4.31(a), with a overhang between bottom and top Pt layers. This caused the short

circuit of all devices in the wafer, but was easily solved by modifying the design as seen in Figure 4.31(b): a perpendicular intersection is designed at each bottom-to-top crossing.



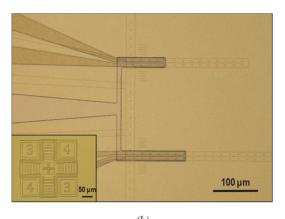
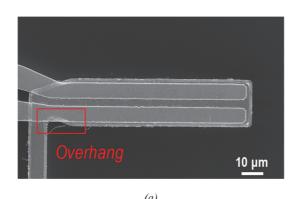


Figure 4.30: Bottom and top layers after development. (a) The bottom electrode is shared by pairs of adjacent cantilevers. It is possible to see the alignment with the underlying channel, coated with AlN/Pt. The inset shows one of the two alignment marks used to align this pattern (layer 3) to the channels defined by EBL1 (layer 1). (b) Top electrodes overlapping on top of bottom layers. Each cantilever is reached by two electrical tracks in order to provide actuation and readout. The alignment mark in the inset shows successful alignment between the top stack (layer 4) and the bottom one (layer 3).



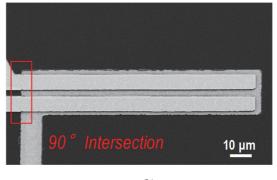


Figure 4.31: First and second generation of top and bottom electrode design. In (a), the overhang between top and bottom Pt causes the short-circuit in all the devices on the wafer. (b) The design is modified in order to only allow perpendicular crossing between electrical tracks. This solves the short circuit problem. With this pattern, a dynamic resistance above $10 \, M\Omega$ was measured between bottom and top Pt, in a voltage range between $1 \, and \, 5 \, V$.

At the 90° intersection in Figure 4.31, the active AlN and top Pt need to climb the bottom layer step (40 nm thick). An example is shown in Figure 4.32. However, the dry etching of Pt layers in chlorine chemistry often results in fences all around the pattern edge, as shown in Figure 4.33 [104]. Sonication of the wafer in IPA bath for few minutes is generally sufficient to break and remove these structures. Unfortunately, the microfluidic channels do not survive sonication, so this solution cannot be followed.

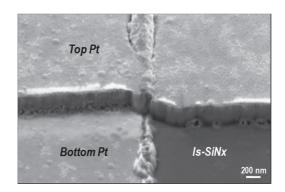


Figure 4.32: Top layers smoothly stepping on the bottom layers. This configuration results in continuous electrical conductivity across the step, and isolation between the Pt layers.

Fences are an issue mostly because they can cause short-circuit between top and bottom electrodes. Regardless of the material that constitutes the fences (resist and etched materials, including Pt) they could easily fall and short circuit PZE electrodes at any moment during the fabrication. Since we have not been able to identify the material, and it is likely that they are made of some sort of alloy or mixture of materials, we have not been able to find a method to prevent fences, nor to remove them selectively. In some cases we have seen that it is possible to remove them immersing the wafer in KOH etching. This is not the most practical solution, considering that decontamination in HCl for 2 hours needs to follow the dip in KOH. Also, KOH is very aggressive to AlN, thus it is important to limit this etching to few seconds. Figure 4.33 (b), shows deposited AlN/Pt coating a fence in a conformal fashion.

Finally, some of the wafers were processed with an additional photolithographic mask to create "polysilicon islands" below the electrical tracks, as shown in Figure 4.34. Such features serve to remove (by dry etching) the PolySi in between adjacent tracks, thus reducing electrical coupling through the substrate. The islands extend from the edge of the chip, until intersection with the insulating trenches defined via EBL1, and shown in Figure 4.34 (red frame). Indeed, this strategy decreases the impedance measured between adjacent tracks by about 20%, but the technological effort (1 more photolithographic and etching step) is considered excessive with respect to the benefit. Therefore, the PolySi-island approach is abandoned.

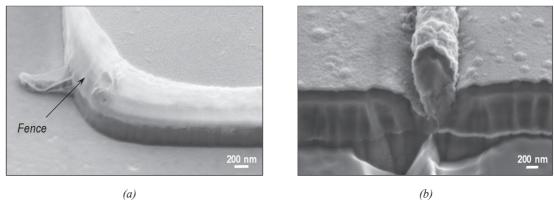


Figure 4.33: Fence resulting from Pt etching in chlorine chemistry. (a) These structures are made of photoresist and etching products, including Pt, thus can cause short circuit between bottom and top electrodes. (b) Sputtering layers on top of fences coats conformally the standing structures, resulting in irregular deposition that could cause short circuit. Fences can be removed with few seconds etching in KOH, followed by decontamination in HCl.

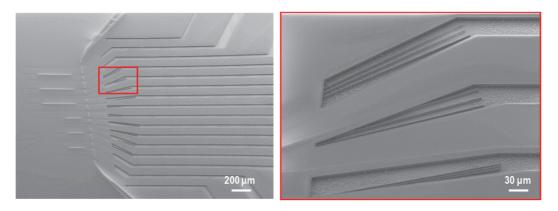


Figure 4.34: Polysilicon islands defined below adjacent tracks, to limit electrical coupling through the conductive sacrificial layer. These structures extend from the edge of the chip to the insulating trenches defined via EBL1 (in the inset).

4.4 Release

The last step of SMR fabrication is the definition of resonators and fluidic inlets. Both singly and doubly clamped beams are defined via optical lithography and a combination of dry etchings. Resonators are 30 μ m-wide and have lengths between 250 μ m and 1000 μ m. The process flow schematic is shown in Figure 4.35, while the full release process is reported in detail in Table 4.5.

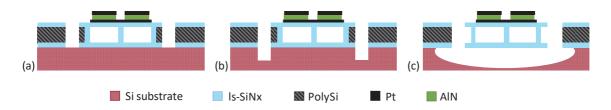
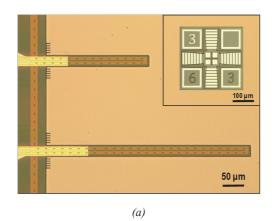


Figure 4.35: Final steps of SMR process flow to release the hollow resonators. Both singly- and doubly-clamped beams are defined via optical lithography and a combination of dry etchings.

SMR shape is defined via photolithography at Heidelberg MLA150, using 5 μ m-thick PR AZ ECI and an exposure dose of 220 mJ/cm². The pattern is then transferred down to the Si substrate via anisotropic etching of ls-SiN_x/PolySi/ls-SiN_x (steps 1-3 in Table 4.5) at AMS 200 Silicon Etcher, as shown in Figure 4.35(a). A Bosch® process step (anisotropic) allows to etch down into the Si substrate for about 15 μ m, as seen in Figure 4.35(b) and Figure 4.36(a). This makes the release faster and limits the Si underetching during the isotropic etching in SF₆ gas (Figure 4.35 and Figure 4.36(b)). Considering SMR width of 30 μ m, a target of 20 μ m (lateral) is set for the etching in SF₆, in order to ensure complete release of the structures. The transparency of ls-SiN_x helps to check the status of the release, while final confirmation is given via SEM inspection, shown in Figure 4.37.

Table 4.5: Detailed parameters for SMR release at AMS 200 SE.

Step	Material	Thickness [µm]	Program	Gas	Time	Etching rate [nm/min]	PR thickness [μm]
0	/	/	/	/	/	/	5
1	ls - SiN_x	1.4	SiO PR 1:1	C_2F_6	5'	300	~3.5
2	PolySi	6	SOI_ACC_ADP	SF ₆ /c-C ₄ F ₈	2'	4500	~3.2
3	ls - SiN_x	0.5	SiO PR 1:1	C_2F_6	2'	300	~2.6
4	Si	15	SOI_ACC_ADP	SF ₆ /c-C ₄ F ₈	2'30''	5000	~2.3
5	Si	20	Si_release	SF ₆	3'+2'	6000 (lateral)	~2



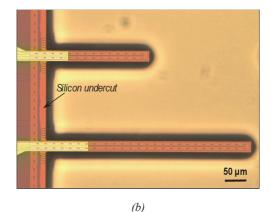


Figure 4.36: Optical images of devices at two different stages of the release process. In (a), cantilever pattern is transferred to the bottom substrate via dry etching of ls- SiN_x -PolySi/ls- SiN_x . Resonators are cut 4 μ m apart from the channel walls, to account for alignment tolerances and trench being larger than design. The inset shows an alignment mark between layer 6 (resonators, counting PolySi island mask) and layer 3 (bottom electrode). Image (b) shows the cantilevers released after isotropic etching in SF₆. This last step creates an undercut region in the Silicon, as shown by the arrow.

This last photolithography (layer 6, counting the PolySi islands mask) also defines fluidic openings to the channel inlets. Due to the isotropic etching and the fact that the sacrificial PolySi has already been removed from the channels, this process causes the creation of a cavity (80 µm deep) below the fluidic inlets, as shown in Figure 4.38. Initially this feature was not considered problematic and was thought to act as reservoir at channel entrance. Instead, as will be explained in Chapter 6, it seems to be an issue for the detection of particles.

SMR release is a relatively simple step, compared to the rest of the fabrication described in this chapter. The most important requirement is to use a photoresist that is thick enough to protect the structures through the five etching steps. To be conservative and take into account possible issues that may arise during the long process, a thickness of 5 μ m is chosen. In the best case scenario (correct machine operation and straightforward material removal), at the end of the process there would be 2 μ m of PR left, as shown in Table 4.5. However, the resist usually burns at the tip of the longest singly-clamped resonators (750 μ m and 1000 μ m) during the last minutes of release in SF₆ gas.

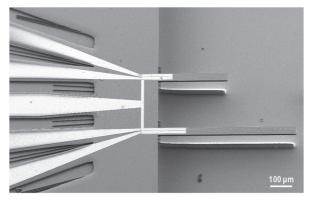
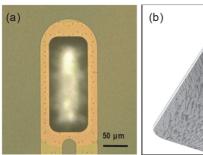
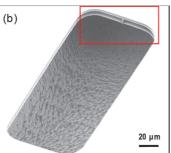


Figure 4.37: SEM image of two released cantilevers, 250 µm-and 500 µm-long. This inspection confirms that the release etching is complete. The image also shows PZE electrodes running on PolySi islands, separated by Is-SiNx insulating trenches.

The reason is that, once the connection with the Si substrate is interrupted, the heat generated during the etching can only escape through the clamp of the resonators. In case of longer cantilevers heat dissipation from tip to clamp is too slow and causes the burn of PR and the increase of its etching rate. This is not an issue, as long as the PR is thick enough. To mitigate this effect, the total release time of 5 minutes is divided in two steps, of 3 and 2 minutes each.





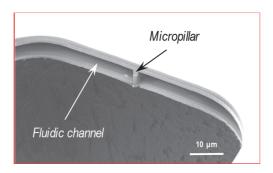
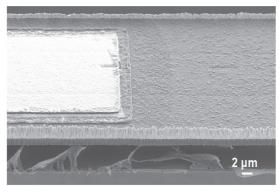


Figure 4.38: Fluidic inlets opened during the release process. (a) Optical image showing the top view of a fluidic inlet. The lighter color around the aperture indicates the Si undercut, created during SF₆ etching.(b) SEM image of an inlet and the cavity obtained below, due to isotropic silicon etching. This cavity is about 80 μ m deep and is thought to act as a liquid reservoir during experiments. The inset shows the 5 μ m-thick fluidic channel, suspended above the inlet cavity.

After PR strip all the structures are intact and successfully suspended. However, etching residues are left at the edges of the resonators, as visible in Figure 4.39. We believe that this may be due to the passivation layer, accumulated during the long Bosch® process. This layer can be removed by immersing the wafer for few seconds in KOH, followed by decontamination in HCl and careful rinse in water and Isopropyl Alcohol (IPA). The released structures survive well to wet processes, if these are performed gently and no stirring is applied. To avoid stiction, SMRs are transferred from bath to bath without allowing them to dry. Also, the last rinse is performed in IPA, which has a lower surface tension with respect to water and helps preventing stiction of the resonator to the substrate, during drying under air laminar flow. In addition, stiffening structures are distributed around the SMR clamp, where the isotropic release in SF₆ causes an underetching of Si substrate (seen in Figure 4.36(b)). The purpose of these structures is to limit the effect of the undercut region on the mechanical properties of the resonator.

Figure 4.40 and Figure 4.41 show two examples of fabricated SMR arrays, singly and doubly clamped, with lengths between 250 and 1000 μm . The final process includes 5 masks: 2 e-beam lithographies and 3 photolithographies, and has a yield larger than 90%. Wafers are finally cleaved into chips 1.5 by 2 cm is dimensions, ready to be tested. Fluidic and electrical connections that enable the characterization of fabricated devices are described in the next Chapter.



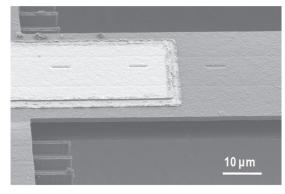
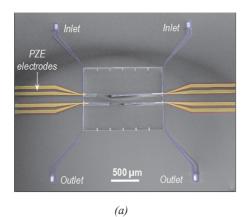


Figure 4.39: Residues of passivation layer on the sides of a resonator, after release and resist strip. This layer is accumulated during the long Bosch® process to etch through the Si substrate (a). It can be removed with few seconds of KOH etching (b).



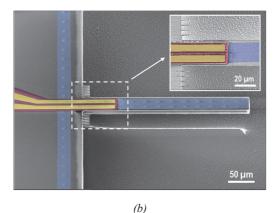


Figure 4.40: Fabricated SMRs with integrated PZE transduction. (a) SEM image of two SMR arrays (top view). The path of the embedded microfluidic channel goes from inlet to outlet (purple color). (b) Zoom-in on a 250 µm-long SMR. Traces of dashed apertures sealed by nitride are visible along the channel. PZE electrodes extend for one fifth of the total resonator length, as a trade-off between transduction efficiency and visual access to the channels (bottom and top electrodes are shown in red and yellow, respectively). The inset shows nitride stiffening structures distributed around the SMR clamp, in order to limit the effect of the undercut region (which results from isotropic release in SF₆ gas) in the mechanical properties of the SMR.

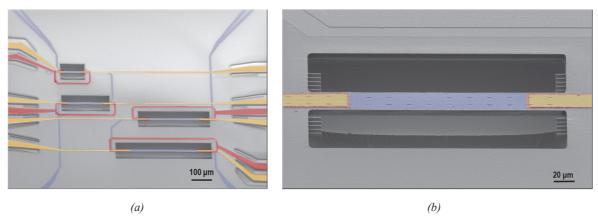


Figure 4.41: Fabricated doubly-clamped SMRs with integrated PZE transduction. (a) shows a chip design with beams 250, 500, 750 and 1000 µm-long beams. All geometries are successfully fabricated, and no buckling or fracture is observed after resonator release. (b) shows a zoom-in of a 500 µm-long doubly-clamped SMR.

4.5 Chapter conclusion

The fabrication of transparent and PZE-transduced suspended microchannel resonators is achieved via a 6-mask process flow of 28 steps (full process in Appendix A and B). 250, 500, 750 and 1000 μ m long singly- and doubly-clamped SMRs are fabricated.

The fabrication is based on the etching of a *sacrificial polysilicon* (PolySi) layer sandwiched between two structural layers of low-stress silicon nitride (ls-SiN_x). Microchannel walls are constituted by high-aspect ratio trenches, defined via Bosch ® process etching and filled with LPCVD ls-SiN_x. The etching parameters have been optimized to (i) keep the width of the obtained trench as close as possible to the designed one (0.6 μ m), (ii) reach and stop at the bottom ls-SiN_x and (iii) give a uniform result across the wafer. This first step also defines *stiffening structures* around resonator clamp, *micropillars* inside the embedded channels and *insulating trenches*.

Discontinuous etch apertures are defined on top of the buried channel and provide selective access to the KOH solution, that removes PolySi from channel interior. Since KOH is completely confined by the ls-SiN_x walls (negligible etch rate), the etching can be extended by few minutes in order to ensure *channel emptying* all over the wafer, with no risk of over-etching or structure damage. In addition, the duration of the etching does not depend on the channel length, simultaneously enabling the definition of arrays of multiple SMRs with different lengths. Channels are emptied in 25 minutes with a yield larger than 95%. Etch openings are filled with a single LPCVD ls-SiN_x deposition, which seals the channels, but is also deposited on their internal walls. This results in an increase in SMR mass and stiffness by 25% and 50%, respectively. However, it is possible to thin down the top nitride via dry etching, paying attention to not reopen the top surface of the channels. Fabricated channels span 25%, 60% and 100% of the resonator length, and are able to withstand a pressure difference up to 2 bars between inlet and outlet.

The fabricated microfluidic channels lie underneath the flat surface of the wafer and are mechanically strong, hence withstanding further microfabrication processes. *Piezoelectric transduction* is integrated on top of the sensors, in order to enable independent actuation and readout of each resonator. PZE electrodes in Aluminum nitride (AlN) and Platinum (Pt) are fabricated via sputter deposition, photolithography and dry etching. Bottom and top tracks are patterned with two different masks. During these lithographies, it was found that photoresist diffuses through the Pt layer and generates residues, which degrade the growth of AlN active layer. The issue is solved interposing a SiO_2 layer between Pt and PR, that ensures a clean Pt surface. To avoid short circuit across the AlN, the crossing between bottom and top electrodes is minimized, and is only allowed via perpendicular intersection of the tracks. *Fences* formed during dry etching of Pt in chlorine chemistry are another potential cause of short circuit. They can be removed in few seconds of KOH etching. Applying these steps and corrections allows to obtain good electrical insulation between the electrodes: more than 85% of the probed pads show a dynamic resistance between bottom and top Pt above $10 \, \mathrm{M}\Omega$, in a voltage range between 1 and 5 V.

An additional photolithography defines "polysilicon islands" below the electrical tracks. These features serve to remove (by dry etching) the PolySi in between adjacent tracks, thus reducing electrical coupling through the substrate. Indeed, impedance between electrical pads decreases by 20% but the technological effort is considered excessive with respect to the benefit. Therefore, further fabrication runs do not include this mask.

Resonator release and fluidic inlets are defined via optical lithography and a combination of dry etching steps. Resonators are defined cut 4 μ m apart from the channel walls, to account for alignment tolerances and trench being larger than design. Release is achieved via few minutes of isotropic etching in SF₆ gas. Thanks to the transparency of ls-SiNx, it is possible to see a difference in color between hollow and PolySi-filled regions, thus having immediate confirmation of release conclusion. The isotropic etching of silicon causes the creation of a cavity below the fluidic inlets. This cavity is about 80 μ m deep and is thought to act as a liquid reservoir during experiments.

All geometries are successfully fabricated, and no buckling or fracture is observed after resonator release. This fabrication is versatile: different channel aspect ratios and wall thicknesses can be easily achieved by modulating the sacrificial PolySi thickness and the e-beam trench design. 32 SMR arrays on each wafer are fabricated with a yield higher than 95%.

Chapter 5

EXPERIMENTAL SETUP

This chapter presents a brief introduction to MEMS packaging. Follows the description of the developed experimental platform which includes fluidic interface, temperature control and electrical connection. Measurement setup is also presented.

5.1 Introduction

The characterization of SMRs necessitates of a reliable experimental platform where "world-to-chip" connections allow to control fluidic, electronic and thermal phenomena. Fabricated wafers are cleaved into chips, 1.5 by 2 cm in dimensions, which integrate on their top surface fluidic openings, as well as electrical tracks.

This chapter presents a brief overview about SMR packaging developed in literature. Later, the strategies and platform developed in this thesis are discussed. Finally, an overview on the measurement setup is presented.

5.1.1 SMR packaging in literature

Packaging and interfacing of MEMS is a fundamental step to characterize sensor devices. Microfluidic and electrical interconnections need to be planned together with the design of MEMS, in order to take into account size-limitations, material compatibilities and geometrical configurations [105]. For instance, microfluidics does not scale together with microelectronic miniaturization, which makes fluidic delivery and control a challenge at the nano and microscale. In addition, packaging cannot be standardized as it depends on the specific application of the sensor to characterize. Hence custom experimental platforms need to be engineered to support efficient operation of devices.

The methods seen in literature for SMR packaging are based on two main approaches:

- Wafer-level packaging, where vacuum encapsulation, fluidic delivery and electrical connections are provided via glass-frit bonding of a glass wafer to the SMR substrate [94].
- 2) Chip-level plug-and-play configuration, that allows to reversibly encapsulate the chip in a modular platform, where fluidic connections and vacuum sealing are provided, together with temperature control [63].

Both strategies demonstrated optimal control and reliability. While the second approach requires more manual handling and plugging by the operator, the wafer-level packaging constitutes an elegant and permanent solution. However, additional process steps are required, further complicating the process flow and increasing the fabrication costs.

5.1.2 Packaging strategy

In this project, device packaging is based on a modular approach, similar to the one reported in [63] by Khan and coworkers. The focus is on *fluidic delivery*, *electrical connections* and *temperature control*, while vacuum encapsulation on-chip is a second order priority at this stage of the project. The general requirements for the packaging of fabricated chips are:

Visual access to the sensing window, where the SMR sensors are distributed, in order to allow visual inspection during experiments.

- Reversibility, in order to allow chip disassembling and exchange, cleaning or SEM inspection. Also, using the same interconnections for several chips would contain costs.
- Isolation between fluidic and electrical connections, to prevent short circuit on chip.

These needs are satisfied by sandwiching the chip between a custom chip-holder and a 3-D printed *fluidic connector*, both designed and developed during one of the master projects supervised by the PhD candidate [106]. The connector is aligned to the four fluidic inlets on the SMR chip and screwed into the holder. O-rings between connector and chip ensure fluidic sealing, while a central opening enables visual inspection and optical detection of the sensor.

To provide *electrical connections*, a simple PCB layout is developed. The custom PCB is screwed to the chip-holder and wire-bonded to the PZE electrodes, independently of fluidic connections.

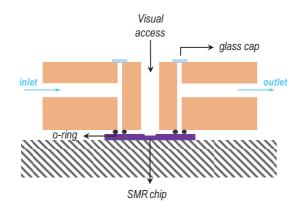
Temperature compensation is achieved using a Peltier cell is in contact with the bottom face of a Copper metal plate, used as chip support. A thermistor sensor is encased in the metal plate and provides real-time feedback to the PID control loop, set on a temperature controller.

These three elements operate independent of each other and guarantee quick chip loading and exchange. Details about materials, design and functionality will be given in the next paragraphs.

5.2 Fluidic interface

A fluidic connector is specifically designed to deliver liquid samples from commercial tubings to the inlets of the SMR chip. Design criteria for the connector are (i) allow visual access to the SMR sensors; (ii) be removable and reusable; (iii) have minimal dead volume; (iv) be reliable at high pressures (≤ 2 bar); (v) be fabricated via simple and low-cost techniques; (vi) be chemically stable with a wide range of liquid samples.

The strategy for liquid delivery, shown in Figure 5.1, consists in sandwiching the SMR chip between a chip holder and the fluidic connector, which is fixed to the holder with two screws. The connector, seen in Figure 5.2, is fabricated via stereolithography at the Additive Manufacturing Workshop (AFA) at EPFL, using a thermoresistant and opaque polymer (RC-70, 3D printing resin from Envisiontec). The connector contains two Tshaped channels which connect inlet tubes (1.59 mm diameter) to the chip inlet (0.5 mm). Since RC-70 is the only material available at AFA for printing at the resolution required (0.5 mm), it is not possible to fabricate a transparent connector. In order to align the T-shaped channels to the SMR inlet, through-holes are defined in the connector. These alignment holes are in communication with the fluidic channels, as shown in Figure 5.1, thus two glass caps are glued with epoxy glue (DP100NS, from 3M) to confine the fluidic volume. A central opening in the connector provides visual access to the resonators. Nitrile o-rings (A. Aubry AG) are glued with epoxy at the outside of the T-shaped channels to ensure fluidic sealing when the connector is screwed to the substrate The interface can be manually aligned to the SMR chip, and provides successful fluidic delivery. When performing fluidic experiments, it is important to make sure of material compatibilities. For instance, RC70 is compatible with IPA and ethanol, while it dissolves in acetone. Nitrile o-rings instead are a good choice for operation with waterbased solutions and oils, while they are not solvent-compatible. Experiments with solvents should use a different o-ring material like EPDM (Ethylene-Propylene Diene Monomer).



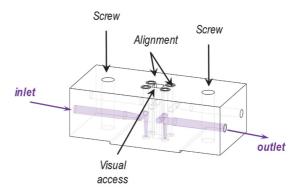


Figure 5.1: Schematic of the fluidic interface. The chip is sandwiched between a fluidic connector and a substrate. T-shaped fluidic channels are aligned to the chip inlets. Nitrile o-rings provide leak-free fluid delivery.

Figure 5.2: 3-D drawing of developed fluidic connector [106]. The fluidic path towards one SMR array is colored in purple. Through-holes enable the alignment to SMR inlets, while a central opening provides visual access to the channels.

Liquids are pushed into the channels using an automated syringe pump (neMESYS, Cetoni GmbH, gear 29:1), and setting the desired fluidic flows via software (QmixElements, Cetoni). A membrane-based sensors monitor the fluidic pressure between the automated pump and the SMR chip, as shown in Figure 5.6. Depending on the volume of the syringe used to push the liquid, different values of fluidic volumes can be achieved. Table 5.1 shows the minimum pulsation-free fluidic flows for three different syringe volumes, together with the equivalent traveling time through a 250 μm-long SMR.

Table 5.1: Minimum pulsation-free flows achievable with different syringes operated by neMESYS fluidic pump. Speed and time to flow through a 250 µm-long SMR are also presented.

Syringe volume	Min pulsation-free flow [μl/min]	Speed [mm/s]	Traveling time in SMR-250 [s]
2.5 ml	1.26	420	0.0012
500 μl	0.25	83.6	0.006
100 μl	0.05	16.7	0.029

The fluidic resistance of tubes and connector can be calculated as shown in Chapter 2. Assuming a 20 cm-long tube with an internal diameter of 0.5 mm, the fluidic resistance from syringe outlet to SMR inlet is calculated to be $\sim 3 \times 10^{10}$ [mPa s/m³], which is 6 orders of magnitudes lower than the fluidic resistance of SMR network.

Even though the developed connector allows the introduction of liquids into the SMRs, fluidic loading and exchange is extremely time-consuming (sample pushing overnight). This is due to the fact that the whole liquid sample needs to flow through the SMR chip. The embedded channels have in fact a fluidic volume of 2 nl from inlet to outlet, while the internal fluidic volume of the connector is $26 \,\mu$ l.

To solve this issue and speed up the experiments, a new version of the connector is created: *bypass channels* are added to the connector design, enabling quick exchange of fluidic samples, within few minutes. In particular, the volume of fluid to be pushed through the SMR chip for fluidic exchange is 95% lower than the previous version of the connector. Details about the fluidic connector geometry are provided in Appendix D, while the optimization of dimensions and materials can be found in the Master Thesis project in reference [106].

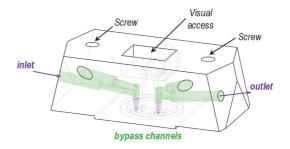


Figure 5.3: Fluidic connector with bypass channels. The volume of fluid to be pushed through the SMR chip for fluidic exchange (in purple) is 95% lower than the previous version of the connector. The volume colored in green represents the bypass path, which takes advantage of the difference in fluidic resistance between the fluidic network on chip and the 3D printed connector.

5.3 Electrical connection

The SMR chip is integrated PZE electrodes for device actuation and readout. It is thus necessary to provide electrical connections to the pads.

Electrical tracks have been designed to be interfaced with commercial flip-lock connectors, like the ones shown in Figure 5.4 (Hirose (HRS), FH12 Series). This configuration was compatible with fluidic openings from the wafer backside, presented in Chapter 4. However, it is rather difficult to integrate them with the fluidic connector described in the previous chapter. The reason is that flip-lock connectors need to clamp the chip edge in order to make electrical connection.



Figure 5.4: Flip-lock connectors from Hirose (HRS, FH12 Series).

At the same time, the fluidic connector needs to exert a uniform pressure on the chip surface, to achieve liquid delivery without breaking the chip. To simplify the interface, a printed circuit board

(PCB) layout is designed and sent for outside fabrication (EuroCircuits). The PCB comprehends five pads connected to ground, and three pads to SMA connectors, as seen in Figure 5.5. The C-shape allows to fix the PCB to the chip holder, while getting as close as possible to the chip edge. PZE electrodes are wirebonded to the PCB, using an Al wire, 33 μ m in diameter.

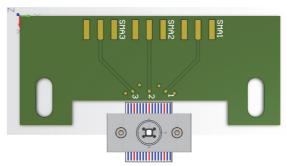


Figure 5.5: Schematic drawing of a chip assembled with fluidic connector and custom PCB (top view).

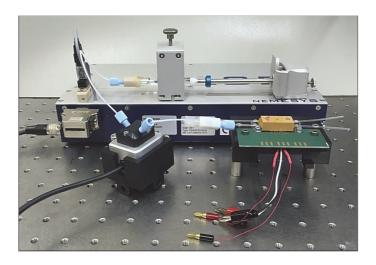


Figure 5.6: Picture of the experimental platform integrating fluidic and electrical connections. A pressure sensor is mounted between the automated syringe pump and the assembled SMR chip.

5.4 Temperature control

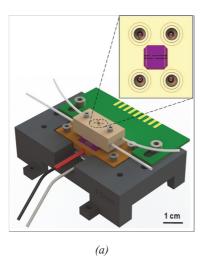
Viscosity is strongly dependent on temperature. For instance, glycerol viscosity decreases by 60% when temperature increases from 20°C to 30°C [89]. As will be discussed in Chapter 6, temperature variations also affect resonance frequency. Thus, it is important to guarantee stable thermal conditions during experiments, in order to ensure reliability and reproducibility.

A temperature control system is implemented using a Peltier module, a thermistor, and a Laser Diode Temperature Controller (LDT-5910C, Newport Corporation). As shown in Figure 5.7, the SMR chip is attached to a metal plate in copper, micromachined at EPFL Mechanical workshop. A square, ~5 mm side, of standard double side tape is applied in the center of chip backside, to attach it to the metal plate. This provides robust clamp and allows fast chip exchange. Using a uniform layer of tape would make impossible the chip detachment from metal plate, damaging the SMRs. No substantial difference was observed on the frequency responsivity to temperature (discussed in Chapter 6), when thermal tape was used instead of standard tape.

The metal plate is screwed to the 3-D printed chip-holder, and its bottom face is in contact with a Peltier module (RC3-4, Marlow Industries Inc.). The Peltier element is placed in a dedicated slot in the chip-holder, and thermal paste is applied to its top face to ensure good thermal conductivity with the copper plate. As visible in Figure 5.7 (b), the Peltier support in the chip-holder is frame-shaped in order to let the bottom (hot) face of the Peltier free to dissipate heat. Also, a fan is connected to the TEC and placed below the holder, to promote heat evacuation from the Peltier module. A thermistor (PR103J2, U.S. Sensor Corp.) is encased inside a dedicated cavity in the metal plate, filled with thermal paste (Type126-4, from Wakefield Solutions Inc.). A target temperature is set via thermoelectric controller (TEC), which builds a PID control system: the temperature measured by the thermistor inside the metal is compared to the setpoint value at the TEC, which calculates the error and modulates the temperature imposed by the Peltier module (via voltage control).

Figure 5.7 presents the developed experimental platform, which integrates temperature, fluidic and electrical control in a modular approach: each control can be independently operated, assembled or removed during

experiments. The PID feedback system allows to control temperature between 20°C and 60°C with an accuracy of 0.01°C. The temperature of the SMR chip is assumed equal to the one measured by the thermistor in the metal plate. The fluidic connector ensures liquid confinement with an external pressure below 10⁻² mbar and a fluidic pressure inside channels up to 2 bar (pressure difference across the SMR chip). Since vacuum encapsulation is not addressed at this stage of the project, measurements with liquid in vacuum are performed by filling the SMR chip and fluidic tubes with fluid, and placing the assembled platform in a vacuum chamber. To provide liquid confinement, the extremities of the tubes are clogged with epoxy glue. The central opening of the fluidic connector is sealed with a glass cap, using epoxy and a nitrile o-ring, visible in Figure 5.7 (a).



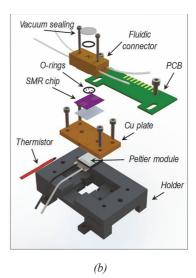


Figure 5.7. Complete experimental platform including fluidic interface, electrical connection and temperature control [107]. (a) SMR chip sandwiched between chip-holder and fluidic connector. The inset shows the connector aligned to the four inlets of the SMR chip, while resonators are visible from the central opening. A PCB is independently attached to the chip holder, while a thermistor and a Peltier module are integrated inside and below the copper metal plate, respectively. (b) exploded view of the assembly (Courtesy of Damien Maillard).

5.5 Measurement setup

The developed experimental platform is integrated in the measurement setup. The main elements of this setup are listed below:

- Automated fluidic syringe pump (neMESYS, Cetoni GmbH, gear 29:1), already discussed
- Thermoelectric controller (LDT-5910C, Newport Corporation), just described
- Lock-in amplifier (UHFLI, Zurich Instruments)
- Laser-Doppler Vibrometer (OFV-551, Polytec GmbH)

The *lock-in amplifier* generates the drive voltage signal sent to the PCB for SMR actuation, and is able to provide a maximum signal of 1.5 V. This tool also allows to build a phase lock loop (PLL) to monitor resonance frequency over time with very large bandwidths, as will be shown in Chapter 6. The readout of SMR deflection can be performed both electrically, via PZE electrodes, and optically, via LDV (next paragraph). In case of electrical detection, the PZE signal is collected by the PCB and sent as an input to the lock-in amplifier.

The laser Doppler Vibrometer allows non-contact detection of resonator displacement and velocity. A laser, with a spot size of $\sim 2~\mu m$, is focused on the surface of the SMR using optical fibers and a optical microscope. The back-scattered light is subjected to Doppler shift, induced by and proportional to the resonator velocity, that is converted into a voltage signal and fed to the lock-in amplifier. The conversion factor for the deflection of the resonator that was used for the measurements presented in this thesis is equal to 50 nm/V, set via Auxiliary decoder. The LDV operates in a linear regime for detected signals up to 800 mV, while above this value the signals are distorted and measurements cannot be performed.

Figure 5.8 shows a SMR chip integrated in the experimental platform and measurements setup, for characterization in air environment.

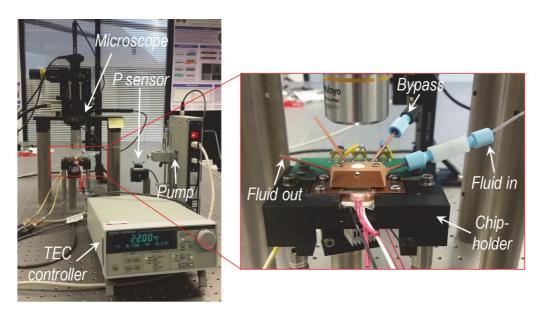


Figure 5.8: Measuement setup for SMR characterization in air. The SMR chip is mounted on the developed experimental platform. An automated syringe pump imposes a fluidic flow, the resulting pressure is monitored by a pressure sensor placed between pump and SMR chip. Peltier module and thermistor are connected to a thermoelectric controller, which builds a PLL for temperature stabilization. A microscope is used to focus the LDV laser spot on top of resonators and provide optical readout. The lock-in amplifier is not shown in the picture.

5.6 Chapter conclusion

The development of an experimental platform is fundamental to enable the characterization of fabricated SMRs. In this thesis, a modular approach is implemented to provide independent fluidic and electrical connection as well as temperature control of the fabricated SMR chip.

The chip is sandwiched between a *chip-holder* and a *fluidic connector*, both developed during a master project supervised by the PhD candidate. The fluidic connector is fabricated via 3-D printing and contains T-shaped fluidic channels that directly interface external tubings to SMR inlets. Nitrile o-rings ensure leak-free flow when the connector is screwed to the holder, in a pressure range between 5×10^{-3} mbar and 2 bar across the SMR. Bypass channels enable quick exchange of fluidic samples, within few minutes.

Electrical connections are provided wirebonding the SMR chip to a custom PCB, which is screwed to the chip holder and interface to a lock-in amplifier.

Temperature control is achieved using a Peltier cell in contact with the bottom face of a Copper metal plate, used as chip support. A thermistor sensor is encased in the metal plate and provides real-time feedback to the PID control loop, set on a temperature controller.

The *measurement setup* enables device actuation via PZE electrodes, and both PZE and optical readout (LDV).

Chapter 6

CHARACTERIZATION

This chapter presents the characterization of fabricated SMRs, performed during the last months of this thesis. Major focus is given to singly-clamped beams, 250 and 500 µm-long, SMRs, with full-length microfluidic channels. Responsivity to mass and temperature is presented, together with characterization of PZE transduction efficiency and fluidic resistance. Frequency stability of the system is studied in different experimental conditions, in order to estimate sensing capabilities of the devices.

6.1 Piezoelectric Transduction

As it has been already discussed, our fabrication was optimized with the target of integrating piezoelectric electrodes on each mechanical device, both for actuation and detection. As it will be shown in this chapter, most of the experiments have been conducted using optical detection, but within this paragraph the proof of principle for fully piezoelectric transduction is presented.

Piezoelectric transduction is tested considering actuation and readout separately.

At first, SMRs are actuated via PZE electrodes, while readout is performed optically via LDV. *Piezoelectric actuation* represents a remarkable improvement with respect to the actuation performed with a standard piezoceramic crystal (piezoshaker) attached to the chip via double side tape, as shown in Figure 6.1. Both the amplitude and the quality of the resonance peak are considerably enhanced.

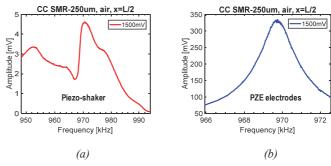


Figure 6.1: Comparison between actuation via piezo-shaker (a) and PZE electrodes (b) for a doubly-clamped SMR, empty in air, for 1.5 V driving voltage.

Figure 6.2(a, b) presents the mechanical response, in air environment, of a 250 µm-long singly-clamped SMR as a function of the actuation voltage, considering empty channels. As expected from theory and shown in Figure 6.2(c), a linear relation between cantilever deflection and driving voltage is found.

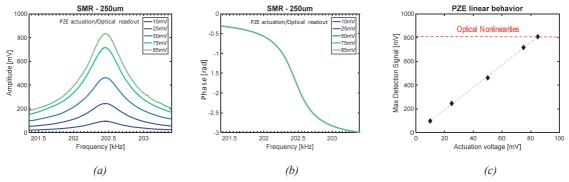


Figure 6.2: Mechanical response of a 250 µm-long SMR, in air environment. Channels are empty (air-filled), actuation is performed via the integrated PZE electrodes, while detection is achieved via optical readout, focusing the laser at the tip of the cantilever. The figure presents the amplitude (a) and the phase (b) of the first mode of resonance, for several actuation voltages. The maximum amplitude of the readout signal depends linearly on the driving voltage (c), as expected in the optical linear regime.

As explained in Chapter 5, the maximum detectable signal with the LDV is limited to $\sim\!800$ mV, due to nonlinearities of the interferometric system. The largest amplitude peak in Figure 6.2(a) (250 μ m- long SMR) is given by an actuation voltage of 90 mV, which corresponds to 834 mV amplitude peak (RMS) and about 59 nm deflection at tip, in air. In vacuum, 4 mV driving voltage results in 756 mV (RMS) at tip and about 53 nm deflection. Quality factor is 430 and 8500 in air and vacuum, respectively.

Piezoelectric actuation efficiency can be calculated from the readout signal (in RMS voltage) by taking into account the LDV conversion factor (50 nm/V). The resulting cantilever deflection in nm can then be divided

by the applied voltage and by the quality factor, in order to obtain the DC actuation efficiency. Results from measurements in air and vacuum environment are compared and found in good agreement with FEM Simulations, as shown in Table 6.1. In particular, two devices are considered: singly clamped 250 µm- and 500 µm-long SMRs, with empty channels. Thus, the same medium is contained into the channels and around the resonators (air or vacuum).

Table 6.1: Comparison l	between measured ai	nd simulated PZ	ZE actuation efj	ficiencies in DC.

	SMR-250 μm		SMR-500 μm	
Environment	Experimental [nm/V]	FEM model [nm/V]	Experimental [nm/V]	FEM model [nm/V]
Air	1.52	1.55	4.64	6.1
Vacuum	1.54	1.55	4.18	6.1

The FEM model shown in Figure 6.3(a) is built via commercial simulation software, and takes into account SMR geometry and materials defined by design. PZE properties are assigned to seed and active AlN layers. Only one of the two fingers is considered for the actuation of the resonator, because the second electrode will be used for readout. In particular, ground signal is applied to the bottom Pt electrode, while 1V voltage is applied to the top Pt. The resulting cantilever static deflection is evaluated, as shown in Figure 6.3(b), under the assumption that it can be approximated to the cantilever mode shape. No damping mechanism is considered in the model.

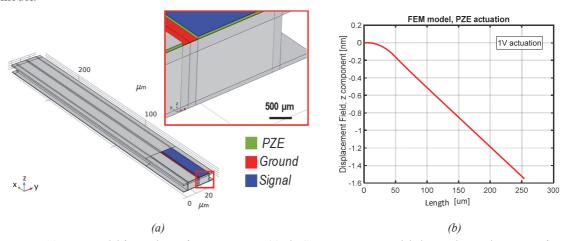


Figure 6.3: FEM model for analysis of PZE actuation. (a) The SMR structure is modeled according to design specifications. The channel interior is left empty, only the solid structure and PZE electrodes are considered. In this particular example results refer to a 250 µm-long SMR. (b) Solid mechanics and electrostatic phenomena are coupled, in order to obtain the static cantilever deflection when IV driving voltage (signal) is applied across the active AlN layer. The model is based on the assumption that the induced static deflection can be approximated to the cantilever eigenshape.

While PZE actuation efficiency results are successful, PZE detection efficiency is rather limited. The main reason for it, as discussed in Chapter 2, is the design of the long metal tracks, which eventually leads to huge parasitics. In order to compensate for this parasitic reactances and make the motion visible electrically, we implemented a carefully balanced bridging technique, schematically shown in Figure 6.4, with the help of a lockin amplifier (Zurich instruments) [108]. Two voltage signals $V_1(\omega)$ and $V_2(\omega)$ are sent to two SMRs close to each other, having common bottom electrode but different resonance frequencies. At first, $V_1(\omega)$ and $V_2(\omega)$ are carefully adjusted and shifted in phase by 180° in order to create a virtual ground at the output terminal $V_{out}(\omega)$

(common bottom electrode). This operation is performed around the resonance frequency but far away from the resonance peak ($i_m \sim 0$, $\omega \sim \omega_r$) and has the purpose to cancel the background created by the parasitic reactances. Subsequently, devices are excited at resonance frequency of the SMR to be detected. As shown in the equivalent circuit of Figure 6.4, the output current is expressed as $i_m + \delta i_0$, where ideally $\delta i_0 = 0$.

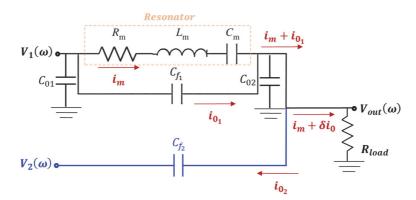


Figure 6.4: Equivalent circuit representing the balanced bridging technique (blue branch), implemented to balance parasitic reactances.

Balancing the parasitics allows to lower the background level of almost 1 order of magnitude and see the mechanical response of the device. Figure 6.5 presents the mechanical response of a fully PZE-transduced (both in actuation and detection) $500 \, \mu \text{m}$ -long SMR, before and after balancing the parasitics.

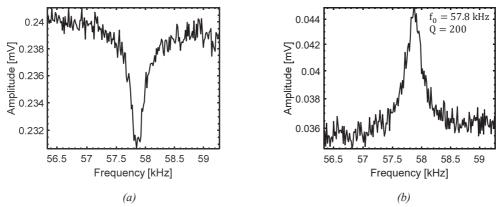


Figure 6.5: Measurement of a fully PZE-transduced 500 µm-long SMR before (a) and after (b) balancing the parasitic current, in air. 100 mV actuation voltage is applied. Balancing the parasitics allows to reduce the background level by almost 1 order of magnitude, thus making the resonance peak visible.

The signal-to-noise ratio (SNR) is determined by the motional parameters of the resonator, calculated in Chapter 2. The SNR could be improved performing the measurements in vacuum, which would increase the value of quality factor and thus improve motional parameters. Crosstalk between electrical tracks could also be a cause of such low detected signal, and should be limited in future by modifying the electrodes design. Because of the low PZE-detected signals (low SNR), the next experimental measurements presented in this thesis have been achieved via PZE actuation and optical readout.

To understand the source of existing parasitics and the difficulty of the balancing technique, the feedthrough capacitance C_f and parasitic capacitance C_0 are estimated.

 C_0 and C_f can be analytically calculated, taking into account electrodes geometry and AlN dielectric properties, as shown in Eq. 6.1 and Eq. 6.2. In particular, C_0 is a parasitic capacitance that models electrical coupling to ground, through the PZE layer of thickness t_{PZE} . As explained in chapter 2.4, C_0 originates from the actuation/detection fingers overlap, with surface $A_{overlap}$ shown in Figure 6.6 (inset). The feedthrough capacitance C_f originates from the electrical coupling between electrical tracks through the substrate. The area of the full electric track A_{full_track} is taken into account for C_f calculation (Figure 6.6), from chip edge to SMR sensor.

$$C_{0} = \epsilon_{33} \frac{A_{overlap}}{t_{PZE}}$$
 Eq. 6.1
$$C_{f} = \epsilon_{33} \frac{A_{full_track}}{t_{global}}$$
 Eq. 6.2

 t_{global} is the distance between the top Pt and the first conductive material encountered when moving towards the substrate (in our case POCl₃-doped polysilicon).

Table 6.2: Calculated feedthrough capacitance C_f and parasitic capacitance C_0 (single finger), with relative electrode areas.(left) In case of C_0 , only the overlap surface of bottom and top electrodes is relevant. C_0 values for the shortest and longest SMRs are given. (right) C_f is calculated considering the full electrical track surface. Given the chip geometry shown in Figure 6.6, C_f value is given for the longest and shortest tracks.

	$A_{overlap} \ [\mu m^2]$	C_0 [pF]
SMR-250	9.9×10^{-10}	0.53
SMR-1000	23.4×10^{-10}	1.24

	$A_{full_track}[\mu m^2]$	C_f [pF]	
Longest track	4.03×10^{-6}	205.83	_
Shortest track	2.57×10^{-6}	131.24	

As shown in Table 6.2, the designed devices have C_0 between 0.53 pF and 1.24 pF, considering 250 µm- to 1000 µm-long SMRs. In this case, the choice of electrodes length being only one fifth of the total resonator length, is actually contributing to reduce the electrical losses due to the parasitic capacitance. C_f values are calculated considering the largest and shortest electrical tracks on chip, and are equal to 205 and 131 pF, respectively. The fact that the feedthrough capacitance C_f is more than 2 orders of magnitude larger than the parasitic capacitance C_0 , and that the motional capacitance of the resonators C_m is in the order of 0.04×10^{-3} pF, shows that electrical detection is limited by parasitic losses through the substrate.

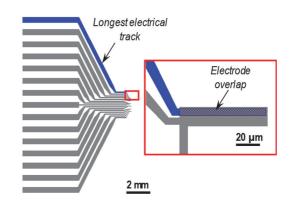


Figure 6.6: Electrical tracks on chip. The area of the track from the chip edge to the device (blue) is about 4 orders of magnitude larger than the electrodes overlap (blue grid, in the inset).

This is due to two main factors:

• the large *electrical tracks area*, as visible in Figure 6.6 (A_{full_track} in Eq. 6.2)

• the conductive polysilicon layer below the ls-SiN_x (which determines t_{global} in Eq. 6.2)

PZE detection can be improved in future fabrication runs, by *reducing the surface of electrical tracks*. As explained in Chapter 5.3, the tracks were designed in order to interface the chip to commercial electrical connectors. However, due to setup constraints, electrical connections are currently made via wire bonding to a custom PCB. Thus, electrodes geometry can be modified in order to minimize parasitic losses.

An additional significant improvement can be achieved by using an *undoped polysilicon* sacrificial layer and a *high-resistive Silicon wafer*. LPCVD polysilicon was doped with POCL₃ in order to increase its etching rate in KOH (by a factor of 2) and empty the microfluidic channels faster, as explained in Chapter 4. This is due to the fact that the initial method used for channel emptying took several days of etching. However, the final fabrication process developed in this thesis allows to empty the channels in 25', therefore the polysilicon doping is no longer necessary (as an etching time of 50' is still reasonable and does not affect the integrity of the wafer). The highly doped polysilicon film is a conductive layer, and constitutes a capacitor together with the ls-SiN_x/AlN (dielectrics), and the top Pt electrode. In this condition, the electrical properties of the Silicon wafer are not relevant to the C_f : even using a high-resistive wafer, the bottom face of the feedthrough capacitor (first conductive layer encountered) would still be polysilicon. Thus, the first modification is to get rid of the conductive polysilicon layer, either by avoiding the doping (upon verification of the electrical properties of the undoped layer), or by finding an alternative sacrificial material with insulating properties.

6.2 Mass Responsivity

In order to determine the mass responsivity of our SMRs, we measure the resonance frequency of our devices for different media contained in the microfluidic channel. As stated in the previous section, throughout this section and the rest of the chapter, actuation is performed using the integrated PZE electrodes. Detection is performed optically using the laser-Doppler vibrometer from Polytec GmbH, using the Auxiliary decoder and a transduction factor of 50 nm/V. Frequency sweeps around resonance are performed using a lock-in amplifier (Zurich Instruments). Experimentally obtained peaks are fitted to a Lorentzian curve to extract both resonance frequency and quality factor [66]. The custom 3D-printed fluidic interface described in Chapter 5.2 is used to deliver fluids to the microfluidic channels [107]. Fluidic flow is controlled via the automated syringe pump.

At first, devices are measured empty (no liquid in the channels), and their response is detected at ambient pressure and in mild vacuum (between 5×10^{-3} and 5×10^{-4} mbar), to investigate the effect of *viscous dissipation* induced by the air surrounding the resonators. Table 6.3 shows resonance frequencies f_r and quality factors Q of the first two modes of vibration, in air and in vacuum environment. Only full channel lengths are considered and experiments are conducted at ambient temperature. These results are collected from the measurement of 4 chips and show the average values of f_r and Q. SMRs with identical design but belonging to different chips present resonance frequency variation below 0.5%, while Q shows variation up to 20%. These differences are attributed to fabrication tolerances.

Compared to f_r values obtained via FEM simulations, using actual dimensions obtained after fabrication, the measurements are well in agreement with FEM model.

Table 6.3: Average values of measured resonance frequencies and quality factors of empty SMRs, full-channel length, in air
and in vacuum environment. After testing 4 chips, variations below 0.5% and 20% are found for f_r and Q , respectively,
considering devices with same design.

Environment	Cantilever Dimensions [µm]	Resonance frequency [kHz]		Quality Factor	
2. Transment	(width x thickness x length)	1st mode	2nd mode	1st mode	2nd mode
	30 x 7.9 x 250	203.2	1167.6	400	580
	<i>30 x 7.9 x 500</i>	57.3	345.5	200	550
Air	30 x 7.9 x 750	26.0	158.2	100	350
_	30 x 7.9 x 1000	15.8	97.9	55	220
	30 x 7.9 x 250	203.9	1170.1	7500	3200
**	30 x 7.9 x 500	57.6	346.3	10000	9600
Vacuum	30 x 7.9 x 750	26.2	159.6	11000	12500
	30 x 7.9 x 1000	15.9	98.1	9800	11500

After testing the resonators empty (filled with air), they are then filled with DI (deionized) water and IPA (Isopropyl Alcohol), and their performances are characterized in air environment. The results of resonance measurements for a 250 μ m- and a 500 μ m- long SMR, empty and filled with liquids, are presented in Figure 6.7.

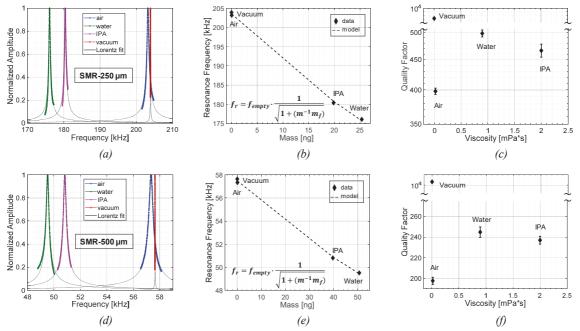


Figure 6.7: 250 μ m-long SMR (a,b,c) and 500 μ m-long SMR (d,e,f) characterization with different fluids. The empty resonators are tested in air and vacuum, actuated via PZE electrodes and detected via an optical interferometer. Measurements with DI water and isopropyl alcohol (IPA) in the channels are performed in air environment (a,d). Figures (b) and (e) show the measured resonance frequencies (first mode) as a function of the mass of the medium inside the channel, for SMR-250 μ m and SMR-500 μ m, respectively. Frequency shifts fit well to the analytical model described by the equation in the inset (dashed line), where f_{empty} and m are fitting parameters. Measured quality factors as a function of fluid viscosities are shown in (c) and (f). Energy dissipation is strongly affected by the medium surrounding the resonator, as can be seen from the drop in quality factor (Q) from vacuum to air environment. However, in the viscosity range under study, Q lies in the same order of magnitude and shows a non-monotonic behavior, when different media are introduced in the channels.

Figure 6.7 (b,e) presents the resonance frequencies as a function of the fluid mass, along with the measurement of the empty device in vacuum. The resonance frequency is expected to be dependent on the density of the fluid, according to Eq. 6.3:

$$f_r = \frac{1}{2\pi} \sqrt{\frac{k}{m + m_f}} = f_{empty} \cdot 1 / \sqrt{1 + \frac{m_f}{m}}$$
 Eq. 6.3

where m_f is the fluid effective mass, and $f_{empty} = \frac{1}{2\pi} \sqrt{\frac{k}{m}}$. The dashed line in Figure 6.7(b,e) represents the fit of experimental data to Eq. 6.3, where f_{empty} and m are fitting parameters. The responsivity to the fluid added mass can be extracted from the slope of the fit in Figure 6.7 (b,e). Mass responsivity depends on the resonator mass and frequency, as explained in Chapter 1, and ranges from a maximum of $\Delta f_r/\Delta m = 1120$ mHz/pg for 250 μ m-long SMRs, to a lower value of $\Delta f_r/\Delta m = 26$ mHz/pg in case of 1000 μ m-long SMRs (Table 6.4). The obtained responsivities are in line with the ones found in literature for resonators in the same frequency and mass range, used in mass sensing applications [49, 93, 109].

Figure 6.7 (c,f) also shows the expected *quality factor* non-monotonic dependence on fluidic viscosity, in agreement with what is thoroughly described by J. Sader and coworkers in previous studies [74]. Measured quality factors confirm that the surrounding medium dramatically affects the device energy dissipation. Nevertheless, the liquid embedded in the channel does not have the same degrading effect. As water is introduced in the SMRs, quality factor shows an increase of around 25% with respect to air-filled devices (both of them in air environment). Substituting water with IPA, the Q decreases by 6%. The reason of this behavior relies in two competing phenomena affecting the energy dissipation of SMRs, namely shear losses due to velocity gradients, and induced in-and-out pumping of fluid within the resonators, as discussed in Chapter 3.

Table 6.4: Measured mass responsivities of SMR devices. For each device type (resonator length), two SMRs from two different chips are tested.

Device	Mass Responsivity [mHz/pg]
SMR-250 μm	1120.45 ± 0.04
SMR-500 μm	159.83 ± 0.005
SMR-750 μm	61.77 ± 0.012
SMR-1000 μm	26.56 ± 0.005

6.3 Fluidic parameters

Fluidic experiments are conducted applying a flow of 0.1 μ l/min with a neMESYS syringe pump, while the pressure is let increase until a maximum P_{max} of about 2 bar across the SMR device. When P_{max} is reached, the syringe pump is switched off and pressure is allowed to relax while experiments are performed. This enables a quick sample delivery and prevents damage of the pressure sensor, which can sustain a maximum pressure of 2 bars for a limited period of time.

Even though the simple water-IPA experiments described in this paragraph do not require careful control of fluidic flow, it is important to investigate the *flow influence on the mechanical response of resonators*. To do so, a PID control loop is set through the QmixElements software by Cetoni to control the neMESYS syringe pump. The software allows to set a constant desired pressure value, while the syringe pump continuously adjusts the delivered flow. After a transient period of about 5 minutes, the pressure reaches a stable value and the mechanical response of the SMR is measured, at room temperature and ambient pressure. Figure 6.8 shows the responses of a 250 μm- and a 500 μm- long SMR filled with DI water in air, as a function of applied pressure. Error bars indicate the standard deviation relative to 6 consecutive measurements on the same device and with same conditions. Despite some of the measured points exhibit large error bars, it is not possible to identify a clear trend as a function of fluidic flow. This leads to believe that applied flow does not have major impact on resonator mechanical behavior, at room temperature; however, further experiments need to be run in future to consolidate this conclusion.

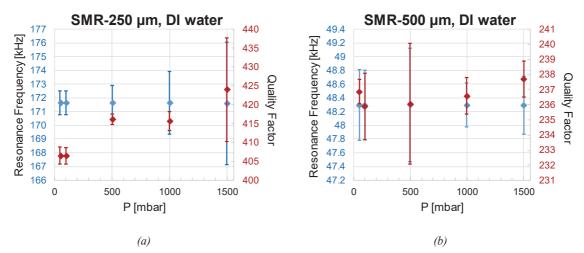


Figure 6.8: Resonance frequency and quality factor as a function of applied fluidic flow for SMR-250 µm and SMR-500 µm, filled with DI water, at room temperature and ambient pressure. Error bars indicate the standard deviation relative to 6 consecutive measurements on the same device and with same conditions.

The steady fluidic flow corresponding to the software-imposed pressure depends on the fluidic resistance across the SMR chip. The *fluidic resistance* R_f of SMR devices was calculated in Chapter 2 using Eq. 2.10, according to designed geometries. Using the dimensions obtained after fabrication (thicker channel walls) R_f is analytically found to be 3.11×10^{16} [$Pa \ s/m^3$] for DI water at 25°C, considering the shortest (left) side of a 4-Cantilever Chip (Figure 2.12(b)). R_f experimental value can be found operating a PID control loop as just discussed, applying a constant differential pressure between inlet and outlet of the SMRs, and measuring the resulting steady flow, as shown in Figure 6.9. Experiments are conducted at ambient pressure and using temperature control system, with setpoint at 25°C. Measured values are presented in Table 6.5, and compared to the one obtained via anlytical calculations.

The estimated value of R_f in Chapter 2 is found fairly in agreement with experimental value of $\sim 2 \times 10^{16}$ [Pa s/m³] (different by a factor of 2). The main possible reasons for this mismatch could be: (i) non-accurate channel dimensions, (ii) non-accurate modellization of the fluid, which is considered incompressible and with a

viscosity calculated at 25°C. For the latter point, we consider that the flow measured by the pressure sensor before the 3-D printed connector, is the same across the SMR network, which is only true when considering incompressible liquids. In addition, the value used for water dynamic viscosity is assumed considering the setpoint temperature on thermoelectric controller (25°C).

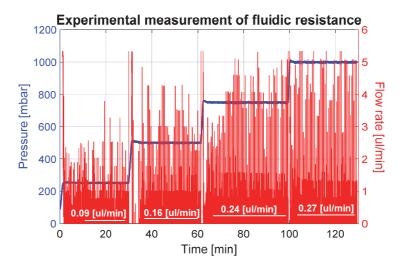


Figure 6.9: Experimental fluidic resistance R_f of a 4-Cantilever chip (short side) filled with water at 25°C, at ambient pressure. R_f is calculated as the ratio between applied pressure difference between SMR inlet and outlet (blue line), and mean flow rate at steady state (red line, with mean values in white text). After imposing a target pressure value, fluidic flow is observed for 30 minutes, in order to reach steady state condition.

Table 6.5: Experimental and analytical values of fluidic resistance of a 4-Cantilever chip, filled with water at 25°C.

Pressure [mbar]	Mean flow rate [μl/min]	Experimental Fluidic Resistance [Pa s/m³]	Analytical calculation [Pa s/m³]
250	0.0936	1.615×10^{16}	
500	0.1574	$I.909\times10^{16}$	4.5
750	0.2432	1.852×10^{16}	3.11×10^{16}
1000	0.2660	2.257×10^{16}	

6.4 Temperature Responsivity

Mechanical resonators have been used in several *temperature-related applications*. High-sensitivity microfluidic calorimeters [110], string-based temperature sensors [10, 111] and hollow resonant beams [112] are just few of the multiple examples that can be found in literature. M-NEMS allow to analyze the thermodynamics of chemical processes or reactions of nanoliter-scale sample volume, without the need of labeling or immobilizing the analyte. Furthermore, hollow resonators may enable the study of chemical reactions involving potentially toxic or inflammable reagents under relatively safe conditions.

The working principle of a temperature sensor based on resonant cantilever is the resonance frequency shift induced by a change in temperature. *Relative temperature responsivity* of the resonance frequency of singly-

clamped beams is given in Eq. 6.4 [20, 113], and is due to thermal expansion and material properties variation as a function of temperature T.

$$\frac{1}{f}\frac{\partial f}{\partial T} = \frac{1}{2E}\frac{\partial E}{\partial T} - \frac{2}{L}\frac{\partial L}{\partial T} + \frac{1}{t}\frac{\partial t}{\partial T} - \frac{1}{2(\rho_s A_s + \rho_f A_f)}\left(\frac{\partial \rho_s}{\partial T}A_s + \frac{\partial \rho_f}{\partial T}A_f\right) = \frac{1}{2}(\beta_E + \alpha_s + \alpha_f)$$

$$Eq. 6.4$$

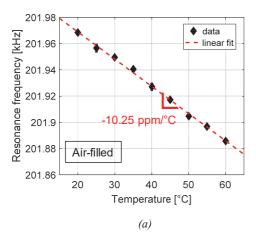
where β_E is the temperature coefficient of Is-SiN_x Young's modulus, while α_S and α_f are the temperature expansion coefficients of solid and fluid, respectively. The major thermal effect in the solid structure is the Young's modulus variation: silicon nitride presents a softening in the Young's modulus with increasing temperature equal to $\beta_E = \frac{1}{E} \frac{\partial E}{\partial T} \approx -30$ ppm/°C, which is roughly one order of magnitude larger than its thermal expansion effect, $\alpha_S \approx 1.2$ ppm/°C [70, 111]. The major temperature-induced effect in fluid is density variation: water thermal expansion coefficient α_f decreases as $-\frac{A_f}{(\rho_S A_S + \rho_f A_f)} \frac{\Delta \rho_f}{\Delta T} \sim 90$ ppm/°C, when considering a temperature range between 20°C and 60°C [114]. An additional phenomenon that could be considered is temperature-induced stress. However, this component is negligible in singly-clamped beams (and in general in stress-released structures) because the induced strain is free to relax, unless the geometry presents very large aspect ratios (which is not the case of this thesis) [71].

In this paragraph, a preliminary study of SMRs mechanical response as a function of temperature is presented. The chip is assembled in the experimental setup described in Chapter 5, where a Peltier cell is in contact with the bottom face of the Copper metal plate used as chip support. A thermistor sensor is encased in the metal plate and provides real-time feedback to the PID control loop, set on the temperature controller (Newport Corporation, LDT-5910C). A temperature range between 20° C and 60° C is investigated under the assumption that the temperature T of SMR devices is the same measured in the metal plate. After setting the target T, the frequency is monitored over time and the SMR mechanical response is measured only upon frequency stabilization (about 5 minutes after T setting).

Results are presented for a 250 µm-long SMR empty (Figure 6.10) and filled with DI water (Figure 6.11), in air environment. When devices are empty (channels filled with air), they show a linear response of –10.25 [ppm/°C] between 20°C and 60°C. Repeating the same experiment while water is flowing in the fluidic channels (0.1 µl/min) allows to find a temperature dependence with linear behavior but opposite slope, equal to +27.76 [ppm/°C] between 20°C and 50°C. The reason of this result is that when the resonator is filled with air, ls-SiN_x Young's modulus is the dominant temperature-dependent factor, while the air in the channel has negligible effect. The linear response is explained by the softening of the Young's modulus which lowers the resonance frequency when increasing the temperature (Figure 6.10(a)). When water is flowing in the channel, frequency response shows the opposite trend compared the empty devices. This is because the temperature dependence of water density is the dominant physical phenomenon in this case, and it increases the resonance frequency as temperature is increased (Figure 6.11(a)).In both cases, quality factor does not show a dependence on temperature, as visible in Figure 6.10(b) and Figure 6.11(b).

These preliminary experiments demonstrate that SMRs can be used to analyze the thermal behavior of a liquid solution inside the microchannels. Larger responsivities are expected from doubly clamped SMRs.

Clamped-clamped beams constitute in fact a more advantageous configuration, since they are highly responsive to changes in stress that is directly related to temperature variations [71].



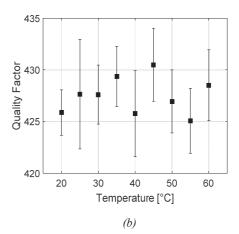
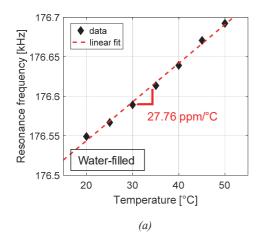


Figure 6.10: Frequency and quality factor as a function of temperature, for an empty 250 µm-long SMR, in air. (a) Increasing temperature, the softening of ls-SiNx Young's modulus lowers the SMR resonance frequency. Experimental data (black diamonds) are fitted to a line (red dashes) having a slope equal to -10.25 ppm/°C (-2.1 Hz/°C), which is the device temperature responsivity. (b) Quality factor does not show dependence on temperature variation.



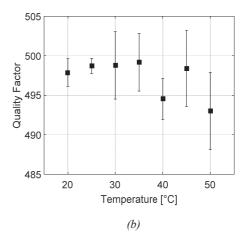


Figure 6.11: Frequency and quality factor as a function of temperature, for a water-filled 250 μ m-long SMR, in air. (a) Resonance frequency dependence presents a linear behavior with increasing temperature, but the slope is inverted compared to the air-filled case. The water density dependence on temperature is the dominant physical phenomenon, and results in a responsivity equal to +27.76 ppm/°C (+4.9 Hz/°C). (b) As in the air-filled case, quality factor does not show a temperature dependence.

6.5 Study of frequency stability

As explained above, our strategy to achieve single-particle characterization consists in monitoring SMR resonance frequency over time, while the analyte flows through the hollow resonator (flow-through detection), as schematically represented in Figure 6.12. Mass and stiffness responsivities (\Re_m and \Re_k) quantify the relative shift in resonance frequency induced by mass and stiffness of the analyte, respectively. Frequency noise δf defines the width of the distribution of resonance frequency as a function of time and is related to the sensitivity of fabricated sensors. The expression of mass sensitivity δm and stiffness sensitivity δk are given in Eq. 6.5:

$$\delta m = \mathfrak{R}_m^{-1} \, \delta f, \qquad \delta k = \mathfrak{R}_k^{-1} \, \delta f$$
Eq. 6.5

As can be seen in Figure 6.12, if δf is larger than the mass- and stiffness-induced frequency shifts, the device response would be totally hidden below the frequency noise level. Therefore, quantification of frequency noise is fundamental to predict the sensing performances of fabricated devices. In particular, the magnitude which is usually analyzed is the relative frequency noise $\delta f/f$ (or $\delta \omega/\omega$), defined as relative frequency stability.

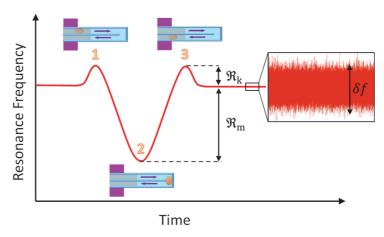


Figure 6.12: Responsivity and frequency noise contributions to the monitored frequency signal. If the frequency noise δf is larger than the mass- and stiffness-induced frequency shifts (\Re_m and \Re_k), the device response would be totally hidden below the noise level.

6.5.1 Allan variance

The universally recognized magnitude to characterize frequency stability in time domain is *Allan variance* $\sigma_A^2(\tau)$, or its square root called *Allan Deviation* $\sigma_A(\tau)$ [115].

In the particular case of resonance-based sensors, $\sigma_A^2(\tau)$ is defined as the statistical variance of N measured normalized frequency values y(t), as shown in Eq. 6.6 [71]. Each measurement is averaged for a time τ , with zero dead-time between two adjacent samples.

$$\sigma_A^2(\tau) = \frac{1}{2} \langle (\Delta y)^2 \rangle = \frac{1}{2(N+1)} \sum_{i=1}^N (y_{i+1,\tau} - y_{i,\tau})^2$$
Eq. 6.6

where y(t) is defined as:

$$y(t) = \frac{\omega(t) - \omega_n}{\omega_n}$$
 Eq. 6.7

Allan variance presents a number of advantages compared to other types of variances introduced since the early 1960's, as statistical instruments for oscillator characterization, in time domain [116]. $\sigma_A^2(\tau)$ converges for most of the commonly encountered types of noise, while the classical variance does not always converge to a finite value. In addition, it shows different behavior for different types of noise. For instance, in presence of white noise $\sigma_A^2(\tau)$ decreases with increasing τ . The common strategy to measure frequency stability of NEMS sensors is to generate a close feedback loop that allows to track resonance frequency in real time. The *phase locked loop* (PLL) configuration established for SMRs is shown in Figure 6.13.

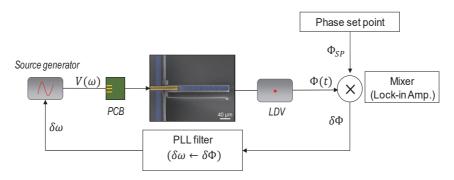


Figure 6.13: Schematic of the Phase locked loop (PLL) for measurement of SMR frequency stability.

A lock-in amplifier generates a voltage signal $V(\omega)$ that is split into two branches: (i) a reference arm, and (ii) a measurement arm, which goes to the SMR chip and actuates the device at resonance frequency ω . The motion of the device is captured by the LDV and compared to the reference arm, thus generating a phase shift $\Phi(t)$. This phase is compared to a phase set point Φ_{SP} that is equal to the phase value measured originally on resonance. The two phase signals are compared and their difference $\delta\Phi$ is converted into a frequency difference $\delta\omega$ by a filter in the feedback loop. $\delta\omega$ is applied as a correction to $V(\omega)$, closing the loop. The PLL needs an accurate determination of the phase to be used as loop set point, in order to have a good estimation of the frequency. Hence, the phase value at resonance is evaluated via frequency sweep, before starting the loop.

Allan deviation $\sigma_A(\tau)$ (square root of variance) of the PLL frequency output can be calculated and plotted as a function of the integration time τ . Figure 6.14 shows a typical Allan Deviation plot, obtained from an empty 250 µm-long SMR, measured in air environment. Three main features can be distinguished from the plot, which can be associated to three different noise sources: (i) a left asymptote, representing the white noise contribution, e.g. thermomechanical noise (TMN), which translates into a $\sigma_A(\tau)$ that decreases as the square root of the integration time. (ii) A right asymptote, originating from the contribution of drift in the system, where $\sigma_A(\tau)$ increases with the integration time, typically with exponential power between 0.5 and 1. (iii) A minimum in the plot is given by the contribution of 1/f noise level. Knowing the different noise contributions as a function of integration time allows to operate devices and perform experiments close to the minimum frequency noise level (20 ppb at 200 ms for the example given in Figure 6.14). This results in the best sensing performances a device can attain. Allan Deviation $\frac{\delta f}{f}$ is in fact directly related to the limit of detection of resonant sensors, as can be seen in Eq. 6.8, in case of sensitivity to mass δm :

$$\delta m = -2m_{eff} \frac{\delta f}{f}$$
 Eq. 6.8

However, operating at integration times corresponding to minimum $\sigma_A(\tau)$ is not necessarily the best configuration when considering a sensor. In the particular case of SMRs, flow-through detection requires in fact a particle residence time in the resonator that is tradeoff between frequency stability and experimental throughput (number of particles analyzed per unit of time) [58]. Particle flow rate is set by the minimum averaging time necessary to obtain a detectable signal above the noise floor. At the same time, the flow should be fast enough to avoid thermal drift of the system and maximize experimental throughput. Finally, the higher obtainable flow rate depends on the maximum pressure drop the channels are able to sustain, before structural damage.

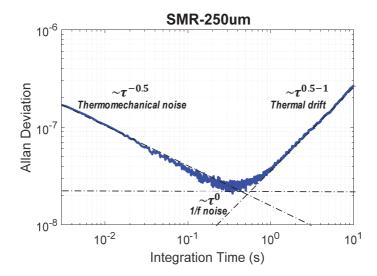


Figure 6.14: Example of Allan deviation plot as a function of the integration time (blue solid line). Three main contributions can be seen: white noise (thermomechanical in the specific case of this thesis) dominates the left part of the plot, where $\sigma_A(\tau)$ is inversely proportional to $\sqrt{\tau}$; 1/f noise gives a flat contribution $\sim \tau^0$. Thermal drift of the system generates an asymptotic behavior on the right part of the plot, where $\sigma_A(\tau)$ is proportional to τ^α , with $0.5 \le \alpha \le 1$. This particular example is a measurement of an empty 250 μ m-long SMR, in air environment. Device is actuated via PZE electrodes and detected via LDV, with laser focused at the tip of the cantilever and a detected signal of 800 mV (RMS value). PLL bandwidth is set to 1kHz with a sampling rate of 858 Sa/s.

6.5.2 Experimental parameters

Frequency stability is related to device and experimental system parameters. As shown in Eq. 6.9, large quality factor, large signal-to-noise ratio (SNR) and small measurement bandwidth are desirable to minimize frequency noise [58].

$$\sigma_{A}(\tau) = \frac{1}{20} \frac{Noise}{Signal} \sqrt{BW}$$
Eq. 6.9

BW is the measurement bandwidth, defined as $1/\tau$.

Noise is the square root of noise power spectral density in $[V/\sqrt{Hz}]$. Its expression for the developed SMR devices is given in Eq. 6.10. In our system, the two main contributions are the background level due to optical and electronic components in the experimental system, and thermomechanical fluctuations.

$$Noise = \sqrt{R_{opt}^2 S_{x,TMN} \phi^2(x) + S_{system}}$$
 Eq. 6.10

- R_{opt} , in [V/m], is the optical transduction factor set by LDV;
- $\phi(x)$, dimensionless, is the resonator normalized mode shape;
- S_{system}, in [V²/Hz], is the power spectral density of background noise, due to the experimental
 instrumentation;
- $S_{x,TMN}$, in [m²/Hz], is the power spectral density of thermomechanical noise.

The Signal in [V], detected by the LDV and generated by SMR vibration, can be expressed as in Eq. 6.11. In our system, the maximum achievable signal can be determined by three factors: mechanical nonlinearities, optical nonlinearities or actuation efficiency. For a singly-clamped SMR sensor of length L, the maximum amplitude at the onset of mechanical nonlinearity is calculated as $x_{nonlin} = 5.46 L/\sqrt{Q}$ [117]. Considering SMR-

250 in vacuum, mechanical nonlinearities are reached for a deflection at tip of 14 μ m. Assuming R_{opt} of 50 nm/V, this corresponds to a detected signal of almost 300 V. Nonlinearities of the available optical setup, set 800 mV as the maximum detectable signal, thus several orders of magnitudes below the mechanical nonlinearity limit. Concerning actuation efficiency, PZE transduction has been studied in paragraph 6.1.

$$Signal[V] = R_{opt}R_{SMR}\phi(x)V_{drive}$$
 Eq. 6.11

- R_{SMR} , in [m/V] is given by the PZE actuation efficiency (values in Table 6.1);
- V_{drive} , in [V], is the actuation voltage.

The fundamental limit of detection depends on the factor limiting frequency stability, which, in our case, is found to be the *Noise/Signal* ratio. A general expression can be given as follows:

$$\frac{Noise}{Signal} = \frac{\sqrt{S_{x,TMN}\phi^{2}(x) + S_{system}/R_{opt}^{2}}}{R_{SMR}\phi(x)V_{drive}}$$
 Eq. 6.12

In our case, *Noise* is generally limited by thermomechanical noise. TMN power spectral density can be expressed

$$S_{x,TMN}(f_r) = \frac{k_B T Q}{4\pi^3 f_r^3 m_{eff}}$$
 Eq. 6.13

where k_B is the Boltzmann constant and T is the device temperature, in Kelvin [71].

Three cases limiting the signal can be discussed:

1. Signal limited by mechanical nonlinearities

This represents the ultimate detection limit, as the measurements would be able to span the full resonator dynamic range, from TMN to mechanical nonlinearities. The ratio *Noise/Signal* can be rewritten as:

$$\frac{Noise}{Signal} = \sqrt{\frac{S_{x,TMN}}{x_{nonlin}^2} + \frac{S_{system}}{\phi^2(x)R_{opt}^2x_{nonlin}^2}}$$
 Eq. 6.14

The best performances would be achieved by (i) maximizing $\phi(x)$, thus focusing the LDV laser spot at the resonator tip (x = L). (ii) set largest available transduction factor R_{opt} at LDV.

2. Signal limited by optical nonlinearities

In case the factor limiting the signal is the detection system, the device dynamic range would be reduced between TMN and onset of optical nonlinearities. The ratio *Noise/Signal* can be expressed as:

$$\frac{Noise}{Signal} = \frac{\sqrt{R_{opt}^2 S_{x,TMN} \phi^2(x) + S_{system}}}{800 \text{ [mV]}}$$
 Eq. 6.15

where 800 mV is the maximum detectable signal in the linear range of the LDV.

The best frequency stability would be obtained by minimizing $\phi(x)$, thus focusing the LDV laser at the resonator clamp (x = 0). In this configuration, optical transduction R_{opt} should be set as low as possible.

3. Signal limited by actuation

In case device performances are limited by the actuation capabilities, the maximum driving voltage the lock-in amplifier is able to provide (1.5 V) would not be sufficient to reach mechanical nonlinearities. The ratio *Noise/Signal* can be written as:

$$\frac{Noise}{Signal} = \frac{\sqrt{S_{x,_{TMN}} \phi^2(x) + S_{system}/R_{opt}^2}}{R_{SMR} \phi(x) \times 1.5 \text{ [V]}}$$
 Eq. 6.16

The best performances would be achieved using a large optical transduction factor R_{opt} , and maximizing the detection signal, thus focusing LDV laser at resonator tip (x = L).

6.5.3 Experimental results

Frequency stability is measured for 250 and 500 μ m-long SMR, to evaluate the limit of detection of our devices. Figure 6.15 presents the results of Allan Deviation measured in air environment, for air-filled and water-filled SMRs. The laser spot is focused at the free end of the cantilevers, resulting into ~800 mV detected signals (onset of optical nonlinearities). The best values found are about 30 ppb for 250 μ m-long SMR at 400 ms, and about 220 ppb for the 500 μ m-long SMR at 200 ms integration time.

Given Eq. 6.9, $\sigma_A(\tau)$ is expected to improve with increasing quality factor. Therefore, Q effect is investigated in order to achieve the best frequency resolution of our system. This effect cannot be seen in air environment, probably due to the fact that quality factors from air-filled to water-filled case, range in the same order of magnitude.

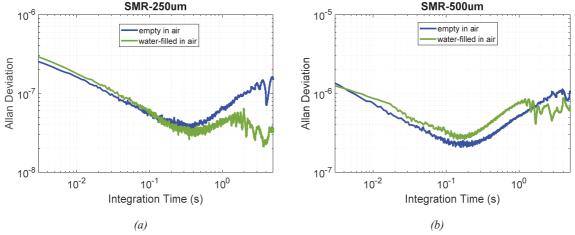


Figure 6.15: Frequency stability of 250 µm-long (a) and 500 µm-long (b) SMR, in air environment.Air-filled and water-filled channels are considered. Devices are actuated via PZE electrodes and detected via LDV, with laser focused at the tip of the cantilevers and a detected signal of 800 mV (RMS value). PLL bandwidth is set to 1kHz with a sampling rate of 858 Sa/s.

As discussed in paragraph 6.2, surrounding environment conditions are the major factor affecting SMRs quality factor. In fact, when reducing external pressure from atmospheric (1000 mbar) to below 10^{-2} mbar, Q increases up to 60 times, as shown in Figure 6.16 (air-filled devices). However, considering a SMR-250, despite a Q variation from 500 to 5600 from air to vacuum environment, the frequency stability remains almost unaffected, as seen in Figure 6.19. This suggests that quality factor is not a limiting factor in sensing performances of SMR devices.

Precisely, $\sigma_A(\tau)$ at 400 ms integration time varies from 30 ppb to 25 ppb from air to vacuum, for the 250 µmlong SMR filled with DI water. These values are very close to the ones presented by Cermak and coworkers in Nature Biotechnology 2016, for arrays of SMRs encapsulated in vacuum, and having dimensions similar to the ones designed in this thesis [62]. Considering that vacuum-encapsulation is routinely implemented for SMR sensors, and causes enormous complexity in experimental setup, compared to operating devices in air [63, 94, 96], a deeper analysis is conducted: frequency stability of 250 µm- and 500 µm-long SMR is collected, with devices empty and filled with DI water, both in air and vacuum environment (Figure 6.19 and Figure 6.21). Tests with liquids in air are performed by imposing 1 µl/min fluidic flow. In contrast, and due to the characteristic of our current fluidic connector, measurements in vacuum are achieved in static conditions, with no flow (as seen in Chapter 5). Furthermore, frequency stability dependence on Q is also embedded in the thermomechanical noise (Eq. 6.13). Thermomechanical and system noise are thus characterized for the same experimental conditions (Table 6.6). $\sigma_A(\tau)$ results are then compared to quality factor and noise variations (Figure 6.18 and Figure 6.20). Noise measurements are performed with the lock-in amplifier from Zurich Instruments, taking the FFT (Fast Fourier Transform) of the optically detected signal, when no driving voltage is applied and laser is focused at resonator tip..

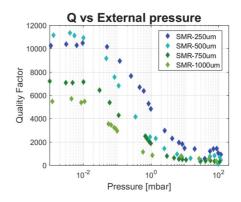


Figure 6.16: Quality factor extracted from the first resonant mode of four empty SMR sensors as a function of external pressure. Typical sigmoidal shape is found, showing stable Q values below ~10⁻² mbar [118].

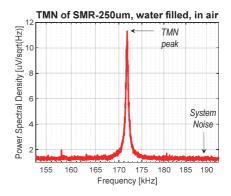


Figure 6.17: Example of noise (PSD) measurement obtained from a 250 μ m-long SMR, water-filled in air. LDV laser is focused at the resonator tip, no driving voltage is applied. TMN peak is about 10 times larger than system background, considering $R_{opt}^{-1} = 50 \text{ nm/V}$.

An example is shown in Figure 6.17. System noise is found to be constant in air and vacuum environment, and independent of readout coordinate x. Measured values oscillate between 0.7 and 1.4 [μ V/ $\sqrt{\text{Hz}}$]. TMN peak at tip is expressed as $\sqrt{R_{opt}^2 S_{x,TMN} \phi^2(L)}$ in [μ V/ $\sqrt{\text{Hz}}$] and varies in the four cases considered as a function of \sqrt{Q} , as presented in Table 6.6

The left part of Allan Deviation curves can be easily estimated from noise measurements applying Eq. 6.9. Dashed lines in Figure 6.19 and Figure 6.21 show the theoretical TMN limit. For both devices considered, $\sigma_A(\tau)$ in air is very close to the TMN limit. However, in vacuum, measured frequency stability results are between 3 to 4 times above TMN prediction. This can be seen more clearly in Figure 6.18 and Figure 6.20, which present the relative variations (with respect to the case of empty devices in air) of TMN, frequency stability and quality factor. TMN peak changes according to \sqrt{Q} , as expected. $\sigma_A(\tau)$ considering 200 ms integration time, on the other hand, follows TMN variations only in air environment, but not in vacuum.

Table 6.6: Noise characterization and quality factors of a 250 µm- and a 500 µm-long SMR, for four different experimental conditions. Noise is characterized focusing the LDV laser at the tip of the resonators, while no driving voltage is applied. In all cases considered TMN is larger than system noise.

Experiment conditions	System Noise $[\mu V/\sqrt{Hz}]$	TMN peak SMR- $250\mu m$ [$\mu V/\sqrt{Hz}$]	Q SMR-250μm	TMN peak SMR- 500µm [µV/√Hz]	Q SMR-500μm
Empty in air	_	8.72	430	30.48	220
Water-filled in air		10.74	500	38.27	260
Empty in vacuum	0.7 - 1.4	32.19	8500	196.99	9800
Water-filled in vacuum	· ·	32.26	5600	183.85	7800

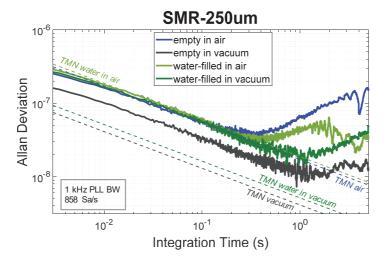


Figure 6.19: Frequency stability (solid lines) of a 250 μ m-long SMR measured at x = L, resulting from ~800 mV detected signals. Dashed lines show the TMN limit, in good agreement with measurement in air. In vacuum, $\sigma_A(\tau)$ is between 3 and 4 times larger with respect to TMN prediction, suggesting the existence of a different limiting mechanism.

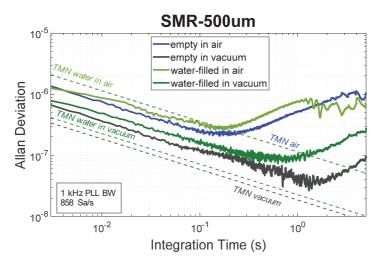


Figure 6.21: Frequency stability (solid lines) of a 500 μ m-long SMR measured at x=L, resulting from ~800 mV detected signals. Dashed lines show the TMN limit, in good agreement with measurement in air. In vacuum, $\sigma_A(\tau)$ is between 3 and 4 times larger with respect to TMN prediction, suggesting the existence of a different limiting mechanism.

Relative TMN, Q and AD variation

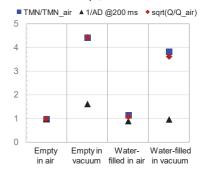


Figure 6.18: Relative variations of TMN peak, frequency stability at 200 ms (inverse) and quality factor (square root), with respect to the case of empty devices in air, for the 250 μ m-long SMR of Figure 6.19. $\sigma_A(\tau)$, follows TMN and \sqrt{Q} variations only in air environment, but not in vacuum.

Relative TMN, Q and AD variation

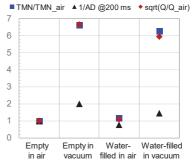


Figure 6.20: Relative variations of TMN peak, frequency stability at 200 ms (inverse) and quality factor (square root), with respect to the case of empty devices in air, for the 500 μ m-long SMR of Figure 6.21. $\sigma_A(\tau)$, follows TMN and \sqrt{Q} variations only in air environment, but not in vacuum.

The reason of this result is not clear, and more experiments need to be performed in order to understand what is the limiting factor to frequency stability in vacuum environment. Nevertheless, noise measurements have been performed on a different chip with respect to the frequency stability measurements. Due to the dependence of both $\sigma_A(\tau)$ and TMN on the eigenshape $\phi(x)$, this could be a major reason of mismatch: the laser is manually positioned at the tip of resonator, therefore a variation of x of few microns should be expected between $\sigma_A(\tau)$ and noise measurements. Future experiments should include noise characterization immediately before each Allan Deviation measurement. Also, a study of $\sigma_A(\tau)$ and noise as a function of external pressure could help elucidate the reason why no significant improvement is found when devices are placed from air to vacuum environment.

After probing the best frequency stability achievable with fabricated devices, a study on measurement parameters is conducted. The goal is to improve our understanding of the frequency noise limitation, and verify the model presented in paragraph 6.5.2.

The effect of the readout coordinate x and the actuation voltage V_{drive} on frequency stability can be seen in the experimental results presented in Figure 6.23. Allan Deviation of a 250 μ m long-SMR, excited in first resonance mode and filled with DI water is presented, both in air (Figure 6.23(a)) and mild vacuum (Figure 6.23(b)) environment (between 5×10^{-3} and 5×10^{-4} mbar). PLL bandwidth is set at 1 kHz, with a sampling rate of 858 Sa/s. The proposed plot shows different $\sigma_A(\tau)$ curves, obtained focusing LDV laser at resonator clamp (x = L/10, in blue), half length (x = L/2, in red) and tip (x = L/2, in orange), as shown in Figure 6.22.

As shown in Eq. 6.10 and Eq. 6.11, both *Noise* and *Signal* depend on the *readout coordinate* x. The magnitudes expected to increase moving along x are mode shape $\phi(x)$ and thermomechanical noise $S_{x,TMN}\phi^2(x)$. Driving voltage is adjusted along x, in order to keep constant the detected signal in volts. Assuming a constant LDV transduction factor $R_{opt}^{-1} = 50 \text{ nm/V}$, this translates into constant values of resonator deflection. Solid lines in Figure 6.23 represent ~750 mV signals, just below optical nonlinearities (corresponding to actuation voltages of ~80 mV in air and ~8 mV in vacuum).

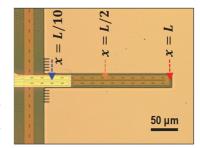


Figure 6.22: Allan Deviation is measured focusing the LDV laser on three different spots along the resonator length.

Moving from clamp to tip (solid-blue line to solid-orange line), $\sigma_A(\tau)$ decreases by a factor of 2.5 and 3.5 in air and vacuum environment, respectively. Thus, the minimum frequency stability is found at SMR tip, considering integration times below ~500 ms in air, and ~1000 ms in vacuum. Above these values of τ , thermal drift dominates and these conclusions are no longer valid.

This result is in contrast with what shown in Eq. 6.9. In fact, moving along the cantilever length and maintaining the detected signal constant to 800 mV, the only magnitude changing is thermomechanical noise. However, TMN increases along x, thus $\sigma_A(\tau)$ should deteriorate moving from clamp to tip. The reason of the opposite trend found between theory and measurements is not understood at the moment, and could have the same explanation of the mismatch between quality factor and $\sigma_A(\tau)$.

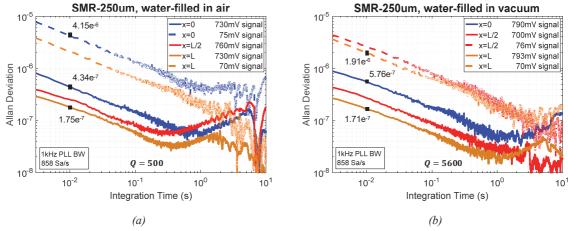


Figure 6.23: Allan deviation dependence on laser position along cantilever x and driving voltage V_{drive} , for a water-filled 250 μ m long-SMR, in air (a) and vacuum (b) environment. Measurements are performed at 1 kHz bandwidth in the PLL, collecting 858 samples per second. Solid lines show $\sigma_A(\tau)$ curves resulting from ~750 mV signals, moving the LDV laser along the resonator length (clamp in blue, half-length in red, tip in orange). Dashed lines present the same experiment repeated for detected signals 10 times lower in amplitude (~75 mV), obtained reducing the driving voltage by a factor of 10. In both air and vacuum environment, the minimum frequency stability is found at SMR tip and for larger detection signals, meaning that signal-to-noise ratio increases along x and with increasing V_{drive} . The device presents a quality factor of 500 in air, and 5600 in vacuum.

Figure 6.23 contains an additional information: dashed lines present $\sigma_A(\tau)$ curves obtained from signals 10 times lower in amplitude (~75 mV), compared to the solid lines. Thanks to the linearity of PZE transduction, this can be easily achieved reducing the *actuation voltage* by a factor of 10. As shown in Eq. 6.11, *Signal* is directly proportional to V_{drive} , while the only component of *Noise* that could show a dependence on the driving voltage is the system noise S_{system} . Experimental results show that a decrease by a factor of 10 in the signal corresponds to an increase of approximately the same factor in Allan Deviation. As can be seen in Figure 6.23 (a), at 10 ms integration time $\sigma_A(\tau)$ at clamp (in blue) increases from 4.34×10^{-7} to 4.15×10^{-6} , when the detected signal decreases from 730 mV to 75 mV. The same behavior can be observed in vacuum environment. Figure 6.23 (b) shows numerical values of $\sigma_A(\tau)$ at x = L (in orange) at 10 ms integration time, equal to 1.71×10^{-7} for 793 mV signal and 1.91×10^{-6} for 70 mV signal. These results confirm that, for the specific integration time considered (below ~500 ms in air, and ~1000 ms in vacuum) SNR scales linearly with V_{drive} . Furthermore, dashed lines show that, even for a ~75 mV signal, frequency stability improves when moving towards the tip, confirming the result previously obtained for larger readout signals.

In conclusion, SMR devices exhibit frequency stability in agreement with state-of-the-art. Currently, thermomechanical noise constitutes the lower limit of device dynamic range, while the upper limit is given by optical nonlinearities: at 800 mV detected signal, cantilevers are not yet in their mechanical non linear regime. This means that there still is room for improvement in $\sigma_A(\tau)$, which is a significant motivation to improve electronic readout, in order to be able to apply larger driving voltages and reach the onset of mechanical nonlinearities.

Quality factor does not affect frequency stability as predicted from theory. The reason of this result needs to be further investigated performing additional experiments. Also, $\sigma_A(\tau)$ is found to improve along the resonator length, when the signal is kept constant, which is in contrast with the model discussed in paragraph 6.5.2. We do not have an explanation for this phenomenon, but it is possible that the unexpected results for x and Q originate

from the same cause. Finally, it is demonstrated that $\sigma_A(\tau)$ scales linearly with the driving voltages, as predicted from theory.

6.5.4 Beads

Mass sensitivity can be directly estimated from Eq. 6.8, knowing frequency stability and device mass. The minimum frequency stability found for a water-filled 250 μ m-long SMR at 400 ms, in air, is equal to 35 ppb. Considering an effective mass ($m_{solid+liquid}/4$) of 2.55×10^{-11} kg, the expected mass limit of detection is \sim 2 femtograms.

To calibrate SMR sensors and provide a proof-of-concept of single particle detection, an experiment with polystyrene beads is designed. Beads are purchased from from Polysciences Inc., have a diameter of 3 μ m and a density of 1.05 g/cm^3 . The buoyant mass in water is calculated as in Eq. 6.17 and is equal to 706 fg, thus largely within the mass sensitivity of fabricated devices. Given mass responsivity of 1120 mHz/pg found in Paragraph 6.2, a single bead at device tip should induce a resonance frequency drop of about 800 mHz.

$$m_{buoyant} = V_{bead}(\rho_{polystyrene} - \rho_{water})$$
 Eq. 6.17

Beads are diluted in DI water as 10^7 particles/ml. Considering that the fluidic volume of 250 μ m-long SMR is 25 pl, this dilution corresponds to 0.25 particles per device. Bead solution is sonicated for 5 minutes right before experiment, to avoid particle agglomeration. 1 nl/min constant flow is applied using a 500 μ l syringe, resulting in 1.5 s for the bead to flow through the whole suspended channel length at a speed of 333 μ m/s.

The particle residence time at tip is about 100 ms, considering a trajectory of about 50 μ m length, as shown by the white arrow in Figure 6.24. Frequency stability at 100 ms integration time is 70 ppb, which can be translated into a mass sensitivity of ~4 fg, well below the buoyant mass of polystyrene beads.

Frequency is monitored over time focusing LDV laser at resonator tip for the maximum detectable signal (800 mV). An optical microscope enables visual access to devices during the experiment. Few minutes after starting to flow the bead solution, resonance frequency shifts from empty device to water-filled value.

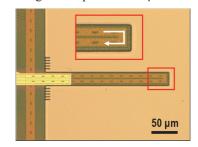


Figure 6.24: To estimate particle residence time at tip, a channel length of 50 μ m is considered, shown by the white arrow in the inset.

Unfortunately, no further shift in frequency occurs in the next few hours and it is not possible to see beads flowing through the channel during the experiment. One possible reason could be that the channels are clogged by beads agglomeration. However, in case of clog, pressure sensors should detect an increase of pressure over time. Instead, P remains stable around \sim 10 mbar during the test. Therefore, the chip is disassembled from experimental setup and carefully analyzed. Optical microscope shows an accumulation of particles at the fluidic inlet, while no bead is found at the chip outlet or inside the microchannels. Further investigation at SEM confirms particle accumulation at channel entrance, as visible in Figure 6.25.

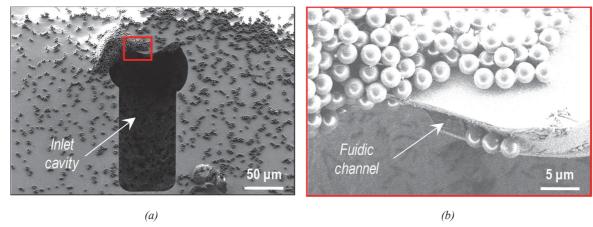


Figure 6.25: SEM image of SMR inlet, after pushing beads into the embedded channel. (a) Particles are accumulated around and at the bottom of the inlet cavity. (b) Zoom-in at the entry of fluidic channel, surrounded by agglomerated polystyrene beads.

The reason of this issue can be attributed to the inlet configuration: as discussed in Chapter 4, after release via isotropic dry etching, fluidic openings result in a cavity about 80 µm deep Figure 6.26. This first attempt at measuring beads in solution seems to demonstrate that particles are being pushed at the bottom of the inlet cavity instead of entering the 5 µm-thick embedded channel, when a fluidic pressure is applied. This may be due to the large fluidic resistance of the channel, with respect to the surrounding cavity which acts as a reservoir. In order to allow particle detection with SMR arrays, inlet definition should be modified in future fabrication runs. A possible solution could be opening fluidic access from the wafer backside as discussed in Paragraph 4.2.2, while keeping the channel emptying from the top as in the last process flow proposed (Figure 6.27). Pillars and rims should be thoroughly included in order to prevent membrane rupture. Microfluidic and structural FEM simulation can help predicting the trajectory of diluted particles and the value of maximum applicable pressure, as a function of nitride membrane aspect ratio.

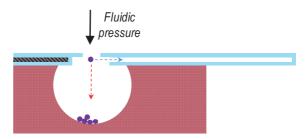


Figure 6.26: Schematic of current fluidic inlet configuration, in cross section (side view). Fluidic access is opened from the top of the wafer, resulting in a 80 µm-deep cavity after isotropic release of resonators. When applying fluidic pressure, particles are pushed at the bottom of the cavity and do not enter the embedded channel.

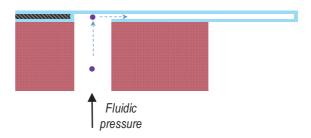


Figure 6.27: Proposed inlet configuration for particle detection via SMRs, in cross section (side view). Opening fluidic access from the backside of the wafer would allow a continuous way to the embedded channels, enabling particles to flow into the hollow resonators.

6.6 Chapter Conclusion

A preliminary characterization on SMR sensors gives an insight on their electrical and mechanical performances, and allows to individuate improvements and modifications to be implemented in future.

Piezoelectric transduction demonstrates efficient actuation, in line with what expected from FEM simulations, in the order of 1.5 nm/V and 6 nm/V for 250 μm- and 500 μm-long SMR in air, respectively. However, due to large parasitic losses, electronic detection is rather limited. PZE detection can be improved in future fabrication runs by reducing the surface of electrical tracks, using an undoped polysilicon sacrificial layer and a high-resistive Silicon wafer. Due to low PZE-detected signals, next experimental measurements are performed via PZE actuation and optical readout.

Fluidic flow in the microchannels is found to not have a major impact on resonator frequency and quality factor, at room temperature. Fluidic resistance is experimentally extracted and found equal to 2×10^{16} [Pa s/m³], in the same order of magnitude of analytical calculations.

Mass responsivity is obtained measuring the resonance frequency variation when different media are introduced in the channels (air, water and IPA). It ranges from a maximum of $\Delta f_r/\Delta m=1120$ mHz/pg for 250 μ m-long SMRs, to a lower value of $\Delta f_r/\Delta m=26$ mHz/pg in case of 1000 μ m-long SMRs. The obtained values are in line with the ones found in literature for resonators in the same frequency and mass range, used in mass sensing applications.

Measured *quality factors* of empty SMRs in air and vacuum environment present a variation of up to two orders of magnitudes. Nevertheless, when liquids are introduced in the embedded channels, Q lies in the same magnitude range and exhibits non-monotonic behavior as a function of fluidic viscosity, as expected from theory.

Temperature responsivity is obtained monitoring resonance frequency of empty and water-filled SMRs in air, at different temperature values. Empty devices show a linear response of –10.25 [ppm/°C] between 20°C and 60°C. Frequency decreases with temperature due to the softening of ls-SiN_x Young's modulus. Water-filled SMRs exhibit a linear frequency response to temperature, opposite in sign compared to the previous case and equal to +27.76 [ppm/°C] between 20°C and 50°C. The water density decrease with increasing temperature is the dominant physical phenomenon, and causes an increase in resonance frequency.

Frequency stability of fabricated sensors is studied in order to estimate their sensing performances and characterize their physical limitations. Allan deviation of resonance frequency is measured in close loop configuration and used to estimate frequency noise. The best frequency stability is found focusing the LDV laser at the tip of cantilevers and actuating until the onset of optical nonlinearities. 250 µm-long SMRs filled with DI water exhibit a frequency stability of 30 ppb at 400 ms integration time, in air, in agreement with values found in literature for SMRs. Frequency stability remains almost unchanged in vacuum reaching a value of 25 ppb at 400 ms, upon quality factor increase of 11 times. In case of empty devices, frequency stability from air to vacuum decreases by a factor of 1.8, while Q increases by a factor of 20. This suggests that quality factor is not the main limiting factor in sensing performances of SMR devices. Thermomechanical and background (system) noise are thus characterized, in air and in vacuum, to individuate the major contributions to frequency noise. Currently, thermomechanical noise constitutes the lower limit of device dynamic range, while the upper limit is given by optical nonlinearities: at 800 mV detected signal, cantilevers are not yet in their mechanical non linear regime.

This means that there still is room for improvement in $\sigma_A(\tau)$, which is a significant motivation to improve electronic readout, in order to be able to apply larger driving voltages and reach the onset of mechanical nonlinearities.

Measured values of frequency stability translate in an estimated mass sensitivity of few femtograms. To calibrate SMR sensors and provide a proof-of-concept of single particle detection, an experiment with polystyrene beads (buoyant mass of 700 fg) is performed. However, particles are not able to enter the embedded channels. The reason of this problem is attributed to the current inlet configuration: after isotropic release of resonators, a 80 µm-deep cavity is created underneath the fluidic access. When applying fluidic pressure, particles are pushed at the bottom of the cavity and do not enter the embedded channel. This issue can be solved in next fabrication runs by opening fluidic access from the bottom of the wafer, thus defining a continuous path to the embedded channels, preventing particle trapping.

Chapter 7

CONCLUSIONS AND OUTLOOK

This chapter summarizes the achievements of this PhD thesis and compares them with the initial project goal. In the second part, future possible developments are discussed.

7.1 Conclusions

This work focused on the development of mechanical resonators with embedded microfluidic channels and integrated piezoelectric (PZE) transduction. The ultimate goal of the project was to use these sensors to study mass and stiffness of biological samples, disentangling their contribution on the measured resonance frequency.

The project started with considerations on design, geometries and materials to be implemented for the fabrication of the sensors. Suspended microchannel resonators (SMRs) were designed in order to minimize the thickness of channel walls and maximize the fluid-to-solid volume ratio, thus achieving high responsivity to mass and stiffness. 250, 500, 750 and 1000 μ m long singly- and doubly-clamped SMRs were fabricated. Resonators are 30 μ m wide and 8 μ m thick, while the target cross section of the embedded channels is 6 μ m x 10 μ m. Channel dimensions are chosen in order to perform experiments with micron-sized analytes such as beads, bacteria or yeast cells.

The strategy adopted to decouple inertial and elastic effects from the mechanical response of SMRs, is based on the dependence of mass and stiffness on the analyte position along the resonator. For this purpose, arrays of identical beams with different channel lengths were *designed* (25%, 60% and 100% of the resonator length). This allows to collect resonance frequency shifts due to the same particle travelling through different channel depths, and analytically decouple the two contributions.

In order to verify that the considerations made in the design phase are correct, *finite element modeling* (FEM) of SMR arrays was conducted. A 3-D fluid-structure interaction of the resonators with embedded fluids is solved using linear mechanics and linearized Navier-Stokes equations. Double coupling is achieved via boundary conditions, imposing fluid stresses and solid velocities at the fluid-solid interface. The model relies on the Eulerian-to-Lagrangian (ALE) formulation to solve both solid and fluid domains in a unique framework. Since no results are reported in literature concerning the stiffness effect on resonance frequency, simulations focused on the energy dissipation of SMRs as a function of fluidic and geometrical properties. This problem is in fact largely studied in literature, as SMR sensors present a unique dissipative mechanism, compared to classic cantilevers immersed in fluids: a combination of shearing and pumping of the fluid inside the microchannels induces a non-monotonic energy dissipation with increasing fluidic viscosity. The developed FEM model demonstrated good agreement with theory and experiments presented in literature. This provides with an easy-to-use and simplified tool to predict SMR physical behavior

More than half of this project duration was focused on the *fabrication* of SMR devices. The complexity of the system requires the simultaneous integration and optimization of mechanics, fluidics and electronics. After several configurations attempted, microfabrication was successfully completed. A 6-mask process flow is optimized, based on the etching of a sacrificial polysilicon (PolySi) layer sandwiched between two structural layers of low-stress silicon nitride (ls-SiN_x). A trench technology is developed to define microfluidic channel walls, while the sacrificial material is removed from the channels via the definition of etch apertures. This enables channel emptying in about 25 minutes with a yield larger than 95%. This result constitutes an enormous improvement with respect to the first strategy attempted, where channel emptying required more than 24 hours and the resulting yield was lower than 50%. Etch openings are filled with a single LPCVD ls-SiN_x deposition, which seals the channels, but is also deposited on their internal walls. This results in an increase in SMR mass and stiffness by 25% and

50%, respectively. However, it is possible to thin down the top nitride via dry etching, paying attention to not reopen the top surface of the channels. Fabricated channels are transparent, biocompatible and mechanically strong to withstand a pressure difference of 2 bars, between inlet and outlet.

Microfluidic channels are embedded below the flat surface of the substrate, thus enabling further fabrication processing. Piezoelectric electrodes are defined via sputtering deposition, photolithography and dry etching, using two different masks for bottom and top contacts. After design optimization and removal of etching residues (fences), good electrical insulation between the electrodes is achieved in more than 85% of the pads on a wafer. Resonators are finally released, and cleaved in chips.

In order to be able to perform experiments with SMRs, chip *packaging and interfacing* was developed. A plug-and-play modular approach allows to separately provide fluidic interfacing, electrical connections and temperature control. At this stage of the project, vacuum encapsulation was not considered, because the priority was to develop a simple experimental setup, to have a feedback about the functionality of the devices. A 3-D printed connector interfaces the chip with the fluidic syringe pump. The connector is aligned directly on top of the chip and screwed to the substrate (chip holder). A central opening allows visual access to the resonators. Nitrile orings between chip and fluidic connector ensure leak-free liquid delivery up to 2 bar pressure difference between chip inlet and outlet. A PCB is screwed to the same chip substrate and provides electrical connection to the PZE electrodes, through wire-bonding. Finally, a PID temperature control loop is built using a Peltier cell and a thermistor in close contact to the chip, together with a thermoelectric controller. A temperature accuracy of 0.01°C can be achieved in a range between 20°C and 60°C.

The last months of this PhD project were dedicated to the *characterization* of fabricated SMR sensors, with focus on singly-clamped (cantilever) devices. At first, a piezoshaker was attached to the substrate to provide actuation, while readout was performed via laser-doppler vibrometer (LDV). This allowed the mechanical characterization of devices (resonance frequency and quality factors). A considerable improvement was obtained via the use of piezoelectric electrodes: larger and cleaner deflection signals can be obtained with driving voltages more than 10 times lower. PZE readout is also demonstrated. However, due to parasitic losses and large electrode surface, the detected signal is difficult to extract from the background noise. After balancing the parasitics, signal amplitude results orders of magnitude lower than the signal detected via LDV. Therefore, detection is performed optically.

Mass and temperature responsivity of fabricated SMRs were measured in different environment and tested with different fluids. Results are in agreement with SMR sensors within same frequency and mass range, reported in literature. In particular, mass responsivity ranges from a maximum of $\Delta f_r/\Delta m=1120$ mHz/pg for 250 μ m-long SMRs, to a lower value of $\Delta f_r/\Delta m=26$ mHz/pg in case of 1000 μ m-long SMRs. Empty 250 μ m-long SMRs devices show a linear response to temperature of -10.25 [ppm/°C] between 20°C and 60°C, while water-filled SMRs exhibit a temperature responsivity of +27.76 [ppm/°C] between 20°C and 50°C.

Frequency stability of fabricated sensors was studied in order to estimate their sensing performances and characterize their physical limitations. Allan deviation of resonance frequency is measured in close loop configuration and used to estimate frequency noise. The best frequency stability is found focusing the LDV laser at the tip of cantilevers and actuating until the onset of optical nonlinearities. 250 µm-long SMRs filled with DI water exhibit a minimum frequency stability of 30 ppb at 400 ms integration time, in air, in agreement with values

found in literature for SMRs. Interestingly, it was found that frequency stability remains almost unchanged in vacuum reaching a value of 25 ppb at 400 ms, upon quality factor increase of 11 times. In case of empty devices, frequency stability from air to vacuum decreases by a factor of 1.8, while Q increases by a factor of 20. This suggests that quality factor is not the main limiting factor in sensing performances of SMR devices. Currently, thermomechanical noise constitutes the lower limit of device dynamic range, while the upper limit is given by optical nonlinearities. This means that there still is room for improvement in frequency stability, which is a significant motivation to improve electronic readout, in order to be able to apply larger driving voltages and reach the onset of mechanical nonlinearities. Measured values of frequency stability translate in an estimated mass sensitivity of few femtograms.

Finally, in order to calibrate SMR sensors and provide a proof-of-concept of single particle detection, an experiment with polystyrene beads (buoyant mass of 700 fg) was attempted. However, particles were not able to enter the embedded channels, probably due to the current inlet configuration. During isotropic release of resonators, a 80 µm-deep cavity is created underneath the fluidic inlets. This feature was initially thought to act as a liquid reservoir. Instead, beads were found to accumulate around the edges and at the bottom of this cavity, when applying fluidic pressure. This opening is thus trapping the particles, preventing them from flowing inside the SMR network.

7.2 Future development

The fabrication and characterization of SMR devices highlighted different limitations and possibility of improvement to be addressed in future work.

Most importantly, the current inlet configuration prevents the introduction of particles in the embedded channels. This issue can be solved *opening fluidic inlets from the backside of the wafer*, thus providing a continuous path to the embedded channel, preventing particle trapping. Fluidic inlets can be fabricated defining apertures through the whole thickness of the wafer, with a combination of dry and wet etching, as reported in Paragraph 4.2.2. This approach would allow to stop at the bottom wall of the channel, and continue the optimized fabrication developed in this thesis, keeping channel interior clean. The bottom nitride could be removed by dry etching just before resonator release, even though the survival of the top nitride membranes should be investigated.

Another improvement would be *reducing the thickness of fluidic channel walls*. This can be achieved by defining narrower trenches and etch apertures via e-beam lithography, which would also limit the internal nitride redeposition. However, it is strongly advised to deposit a minimum thickness of 700 nm ls-SiNx to fill the trenches defined with the first e-beam lithography, independently of their width. This is necessary to ensure the survival of nitride membrane during channel emptying in KOH. This layer can be easily thinned down via dry etching in a further stage. There are instead no constraints for the nitride deposition which serves to fill etch apertures (second e-beam lithography).

This project provided for the first time in SMR arrays, independent integrated transduction of each resonator. Actuation efficiencies of few nm/V are found, reaching the maximum optically-detectable signal with few mV driving voltage. However, the large area of electrical tracks induces *parasitic losses and crosstalk* between

the pads, thus the electrically detected signals are very low in amplitude (low signal-to-noise ratio). PZE readout can be improved by *reducing the surface of electrical tracks*. mm-long electrodes were designed in order to interface the chip to commercial electrical connectors. However, due to setup constraints, electrical connections are currently made via wire bonding to a custom PCB. Thus, electrodes geometry can be modified in order to minimize parasitic reactances. An additional significant improvement can be achieved by *using an undoped polysilicon sacrificial layer and a high-resistive Silicon wafer*. LPCVD polysilicon was doped with POCl₃ in order to increase its etching rate in KOH (by a factor of 2) and empty the microfluidic channels faster. This is due to the fact that the initial method used for channel emptying took several days of etching. However, the final fabrication process developed in this thesis allows to empty the channels in 25', therefore the polysilicon doping is no longer necessary (as an etching time of 50' is still reasonable and does not affect the integrity of the wafer). However, the first modification is to get rid of the conductive polysilicon layer, either by avoiding the doping (upon verification of the electrical properties of the undoped layer), or by finding an alternative sacrificial material with insulating properties. Currently, the highly doped polysilicon film is a conductive layer, and constitutes a capacitor together with the ls-SiN_x/AlN (dielectrics), and the top Pt electrode. Therefore, as long as the conductive PolySi layer is used, the electrical properties of the Silicon wafer are not relevant to the parasitic reactances.

During this project, a reliable tool that models the complex fluid-structure interaction within SMR devices was developed. The FEM model allowed the study of energy dissipation as a function of fluidic viscosity, finding good agreement with analytical and experimental results reported in literature. The next step consists in coming back to the initial goal of the project: investigate the stiffness effect on the resonance frequency. To do so, elasticity should be included in the fluidic domain, in order to *enable the simulation of viscoelastic fluids*.

Finally, the experimental setup developed in this project enables quick and leak-free fluidic delivery in a large pressure range, as well as electrical connections and fluidic control. This platform could be further improved by *providing vacuum encapsulation on-chip*. This could be achieved sealing the central opening of the fluidic connector, by gluing glass cap and top o-ring with a permanent vacuum-compatible epoxy. Access to the central opening should be defined for providing connection to a vacuum pump. This would enable flow-through characterization of liquid samples, while only the central cavity is encapsulated in vacuum.

Appendix A

Full Fabrication Process Flow

Technologies used

LPCVD, E-beam lithography, Dry etching, Wet etching, Thin Film Sputtering Deposition, Photolithography, SEM

Photolithography masks						
Mask #	Critical Dimension	Critical Alignment	Remarks			
1	0.6 um	First Mask	Microfluidic channel: lateral walls definition			
2	0.6 um	5 um	Dashed apertures definition (provide access to the sacrificial material inside the microfluidic channels)			
3	2 um	2 um	Bottom Contact definition			
4	2 um	2 um	PZE layer and Top Contact Definition			
5	5 um	2 um	Resonators definition			

Substrate Type

Silicon <100>, Ø100mm, 525um thick, Single Side polished, Prime, p type, 0.1-0.5 Ohm.cm

Step	Process description	Cross-section after process*
Step		(not in scale)

01	Substrate: Si test	
02	 LPCVD Silicon nitride deposition (microfluidic channel floor) Material: ls-SiN_x Thickness: 500 nm Machine: Centrotherm 	
03	 LPCVD Sacrificial material deposition (I part) Material: POCl₃-doped PolySi Thickness: 3 um Machine: Centrotherm 	
04	WET ETCHING PolySi deglaze in HF bath Etched Material: oxide Machine: Acid Wet Bench Etching Depth: few nm	
05	LPCVD Sacrificial material deposition (II part) • Material: POCl ₃ -doped PolySi • Thickness: 3 um • Machine: Centrotherm	
06	WET ETCHING PolySi deglaze in HF bath Etched Material: oxide Machine: Acid Wet Bench Etching Depth: few nm	
07	E-BEAM LITHOGRAPHY (Mask 1) Patterning of microfluidic channel lateral walls • Machine: Vistec EBPG5000 • Resist: ZEP (280 nm thick) • Critical Dimension: 600 nm	

08	DRY ETCHING High-aspect ratio trenches definition Etched Material: PolySi Machine: A601 Etching Depth: 6 um + Resist strip	
09	 LPCVD Trench filling via silicon nitride deposition Material: Is-SiN_x Thickness: 700 nm Machine: Centrotherm 	
10	 LPCVD Hard mask deposition Material: PolySi Thickness: 500 nm Machine: Centrotherm 	
11	E-BEAM LITHOGRAPHY (Mask 2) Dashed lines patterning Machine: Vistec EBPG5000 Resist: ZEP (280 nm thick) Critical Dimension: 600 nm	
12	DRY ETCHING Dashed apertures definition via Bosch process and c- C ₄ F ₈ • Etched Material: PolySi/ ls-SiN _x • Machine: A601 • Etching Depth: 500/700 nm	
13	 WET ETCHING Channel emptying in KOH Etched Material: PolySi Machine: Wet Bench Base Depth: 50 nm/300 nm 	

14	NEUTRALIZATION Potassium decontamination in HCl • Machine: Wet Bench Acid	
15	 LPCVD Channel sealing via silicon nitride deposition Material: Is-SiN_x Thickness: 700 nm Machine: Centrotherm 	
16	SPUTTER DEPOSITION Seed PZE layer and bottom metal deposition Material: AlN/Pt Thickness: 15/25 nm Machine: Pfeiffer Spider	
17	SPUTTER DEPOSITION Protective oxide deposition Material: SiO ₂ Thickness: 20 nm Machine: Pfeiffer Spider	
18	PHOTOLITHOGRAPHY (mask 3) Seed PZE layer and bottom electrode definition • Machine: MLA150 • PR: AZ ECI (2 um thick) • Critical Dimension: 2 um	
19	DRY ETCHING Seed PZE layer and bottom metal definition in chlorine chemistry • Etched Material: SiO ₂ /Pt/AlN • Machine: STS • Etching Depth: 20/25/15 nm + Resist strip	

20	WET ETCHING Protective oxide removal in BHF • Etched Material: SiO ₂ • Machine: Wet Bench Acid • Depth: 20nm	
21	SPUTTER DEPOSITION PZE layer and top metal deposition Material: AIN/Pt Thickness: 300/25 nm Machine: Pfeiffer Spider	
22	PHOTOLITHOGRAPHY (mask 4) PZE layer and top electrode definition • Machine: MLA150 • PR: AZ ECI (2 um thick) • Critical Dimension: 2 um	
23	DRY ETCHING PZE layer and top electrode definition in chlorine chemistry • Etched Material: Pt/AIN • Machine: STS • Etching Depth: 25/300 nm + Resist strip	
24	PHOTOLITHOGRAPHY (mask 5) Resonator definition Machine: MLA150 PR: AZ ECI (5 um thick) Critical Dimension: 2 um	
25	 DRY ETCHING Resonator shape definition via Bosch process and c-C₄F₈ Etched Material: ls-SiN_x/PolySi/ ls-SiN_x Machine: AMS200 Etching Depth: 1.4/6/0.5 um 	

26	DRY ETCHING Resonator shape definition through Silicon via Bosch process • Etched Material: Si • Machine: AMS200 • Etching Depth: about 10 um	
27	DRY ETCHING Resonator release in SF ₆ isotropic etching • Etched Material: Si • Machine: AMS200 • Etching Depth: 20 um (lateral) • + Resist strip	
28	CLEAVAGE Wafer manual cleavage in chips	

*the wafer backside is not represented for simplicity

Appendix B

Fabrication Run Card

Step N°	Description	Equipement	Program / Parameters	Target	Remarks
1	WAFER PREPARA	TION		•	
1.1	Stock out				
1.2	Check				
2	LOW STRESS SIL	ICON NITRIDE LPCV	D		
2.1	RCA clean	Z3/WB_PreOx_Cle an	H2O:NH4OH:H2 O2 (5:1:1)	15min 75°C	Cmi staff
2.2	LPCVD	Z3/CT_1- 2_LPCVD_SiN	Low stress SiN	500nm	Cmi staff
3	POLYSILICON DE	POSITION	<u> </u>	•	
3.1	LPCVD	Z3/CT_1- 1_LPCVD_Poly	LPCVD Poly	3um	Cmi staff
3.2	POCI3 Doping	Z3/CT_1-4_Doping	POCL3 Doping		
4	Deglaze				
4.1	Deglaze	Z3/Wet_Bench	HF, 10"		Oxide removal. Dip it few times until the color changes from blue to silver.
4.2	Rinse	SRD (washing + drying)			
5	POLYSILICON DE	POSITION			
5.1	LPCVD	Z3/CT_1- 1_LPCVD_Poly	LPCVD Poly	3um	Cmi staff
5.2	POCI3 Doping	Z3/CT_1-4_Doping	POCL3 Doping		
6	Deglaze	·	<u> </u>		
6.1	Deglaze	Z3/Plade Wet Bench Reclaim	Few seconds until I see the wafers changing	few nm of oxide	

			color from blue to		
			silver. Follow		
			rinse and SRD		
			(wash+dry)		
		SRD (washing +	(wasii aiy)		
6.2	Rinse				
7	EREAM LITHOGR	drying) APHY - Mask 1_Cha	and leteral wells		
1	EBEAW LITHOGRA		innei lateral walls	T	T
7.1	Oxygen Plasma	Z2/Tepla GigaBatch	Strip_High , 5 min		
7.2	Dehydration	Hot plate/Z7	3min@183°C		
7.3	ZEP 50% 280 nm coating	Z7/Spin Coater	750 rpm	280 nm thick (5 min)	Clean the backside of the wafer with a tissue stick and some IPA. Pay attention to not spill IPA on ZEP!
7.4	Resist bake	Hot plate/Z7	Soft Bake 5min @183°C		
7.5	Exposure	Z7/Vistec EBPG5000	150na, 300um beam aperture, 143nA, 70nm spot size	CD= 600 nm	25 min (+ 20' for the vacuum and loading)
7.6	Development	Z7/Wet Bench	1min Amyl Acetate, 1min ZEP Rinse		
7.7	Inspection	Z7/uScope			
8	POLYSILICON DR	Y ETCHING: Trench	es_Definition		
8.1	PolySilicon Dry Etch	Z2/ A601E	Aniso_ADP (1'38")	6 um	Bosch process: 5" SF6 (300 sccm) + 2" C4F8 (200 sccm). RF1= 1800, RF2= 90. ER_ZEP=130nm/min. ER_PolySi=4.5um/mi n (ER_IsSiNx=50 nm/min.)
8.2	Inspection	Z6/uScope			I must see green smooth silicon nitride inside the alignment squares.
8.3	Resist strip	Z2/Tepla	Plasma O2 clean: Strip_High , 5 min		
I					

9	LOW STRESS SILICON NITRIDE LPCVD - Trenches Filling					
9.1	RCA clean	Z3/WB_PreOx_Cle	H2O:NH4OH:H2	15min 75°C	Cmi staff	
9.1	RCA clean	an	O2 (5:1:1)	15min 75°C 700 nm 500 nm	Cilli Stall	
9.2	LPCVD	Z3/CT_1- 2_LPCVD_SiN	Low stress SiN	700 nm	Trenches need to be filled! We need AT LEAST 700 nm nitride in order to avoid breaking of the channels during the KOH, and in order to fill the trenches (assuming trench aperture between 0.9 ans 1.1 um). The nitride layer can eventually be thinned down at the end of the microchannel fabrication.	
10	POLYSILICON DEI	POSITION				
		Z3/CT 1-			Hard mask for the	
9.3	LPCVD	1_LPCVD_PolySi		500 nm	next etching	
9.4	Inspection	Z6/uScope	Resolution			
11	EBEAM LITHOGRA	APHY - Mask 2_apert	ures to the channe	els		
11.1	Oxygen Plasma	Z2/Tepla GigaBatch	Strip_High , 5 min			
11.2	Dehydration	Hot plate/Z7	3min@183°C			
11.3	ZEP 50% 280 nm coating	Z7/Spin Coater	750 rpm	-	Clean the backside of the wafer with a tissue stick and some IPA. Pay attention to not spill IPA on ZEP!	
11.4	Resist bake	Hot plate/Z7	Soft Bake 5min @183°C			
11.5	Exposure with Alignment	Z7/Vistec EBPG5000	150na, 300um beam aperture, 143nA, 70nm spot size	CD= 600 nm	~15 min (+ 20' for the vacuum and loading). During alignment: target the centre of the square, not a corner. Do not use continuous SEM, but use SEM shots.	

			1min Amyl		
11.6	Development	Z7/Wet Bench	Acetate, 1min		
			ZEP Rinse		
11.7	Inspection	Z7/uScope			
12	POLYSILICON DR	Y ETCHING: Access	to the channels		
12.1	PolySilicon Dry Etch	Z2/ A601E	Aniso_ADP (20"), ER = 4.5 um/min (POCI3 doped case)	500 nm	Bosch process : 5" SF6 (300 sccm) + 2" C4F8 (200 sccm). RF1= 1800, RF2= 90.
12.2	Silicon Nitride Dry Etch	Z2/ A601E	Nitrure_1 (3'), ER = 300 nm/min	700 nm	ER_zep=130nm/min ER_zep=360nm/min
12.3	Inspection	Z6/uScope			I must see green smooth silicon nitride inside the alignment squares.
13	KOH ETCHING: CI	nannel Emptying			
13.1	Set hot plate for solution warm up	Z14/ Base Wet Bench	set point=85°C for having stable T= 80°C	80°C	Teflon holder + hot plate + thermometer + magnetic rod (gentle spin).
13.2	KOH Etching	Z14/Base Wet Bench	40% KOH @ 80°C, 25min (ER_dopedPolySi : 1 um/min)	around 20 um, 25'	During the etching, I can see air bubbles columns coming out of the apertures. When the etching is done (around 22-23 minutes), I don't see bubbles anymore. We wait few minutes more to clear out the channels completely. If I keep seeing air bubbles even after 25' it is very likely KOH is going out of trenches.
13.3	Rinse	Z14/Base Wet Bench			Rinse very gently at least 3 times. NEVER LEAVE THE WAFER DRYING OUTSIDE WATER! (Two minutes are fine to check at the

					microscope, but
					without drying it.)
14	NEUTRALIZATION				
					Neutralization of
					potassium in HCl, to
					avoid the growth of K
					crystals. Go from the
		Z14/Acid Wet			last water bath to the
14.1	Neutralization	Bench	HCl 37%, 2h		HCl bath directly,
					drying only the
					backside of the wafer
					to avoid too much
					dilution of HCI.
					Rinse very gently at
					least 3 times. NEVER
					LEAVE THE WAFER
		Z14/Base Wet			OUTSIDE WATER!
14.2	Rinse	Bench			(Two minutes are fine
					to check at the
					microscope, but
					without drying it.)
					Go from water to IPA
14.3	IPA Rinse	Z14/Solvent wet	3min		directly, dry only the
		bench			backside of the wafer.
444		70/0514			Check apertures
14.4	Inspection	Z6/SEM			width.
15	LOW STRESS SILI	CON NITRIDE LPCV	D - Channel sealing	g	
					Specify "fragile wafer"
		72/MP ProOv Clo	H3O-NH4OH-H3		and "membranes on
15.1	RCA clean	Z3/WB_PreOx_Cle	H2O:NH4OH:H2	15min 75°C	wafer" in the RCA
		an	O2 (5:1:1)		request. Ask for RCA
					without SRD.
					Trenches need to be
					filled! We need AT
					LEAST <u>700 nm</u> in
					order to fill trenches
15.0	L DCVD	Z3/CT_1-	Low otroca CiN	700 nm	of 0.9-0.1um width.
15.2	LPCVD	2_LPCVD_SiN	Low stress SiN	700 nm	The nitride layer can
					eventually be thinned
					down at the end of
					the microchannel
					fabrication.
<u> </u>	<u>I</u>	<u>I</u>	<u>I</u>	<u>l</u>	1

15.3	Inspection	Z6/SEM			Check that apertures are closed.
16	ALUMINUM NITRIE	L DE/PLATINUM SPUT	TER DEPOSITION		
16.1	Aluminum Nitride_Deposition	Z4/ Spider600	15 nm AIN (19" deposition)	DR: 50 nm/min, T=300°C, 40sccmN2/10scc m Ar, 1500 W plasma, 6W setpoint	Put a dummy wafer per each material, for target cleaning. Check that reflected power for dummy AIN is 0W over a 5' test deposition
16.2	Platinum_Depositi	Z4/Spider600	25 nm Pt (6" deposition)	DR= 270nm/min, T=300°C, 1000 W plasma	Use the program AIN_T_D_Pt_T_D_Et ch
17	SILICON OXIDE SE	PUTTER DEPOSITION	N		
17.1	Silicon Oxide_Deposition	Z4/Spider600	20 nm SiO2 (1' deposition)	DR= 20nm/min, T=room T, 1000 W	Use the program SiO2_F. Protective layer to prevent contact (and diffusion) between PR and Pt. This deposition rate is highly unstable from day to day. Put a Silicon test wafer and check the oxide thickness after 1'. Then proceed with the deposition on real wafers according to the result.
17.2	Condictivity check	Multimeter	Check that R= OL		Check the deposition of the oxide
17.3	Inspection	Z6/uScope			
18	PHOTOLITHOGRA	PHY- Mask 3_Bottor	n_Contact		
18.1	Dehydratation	Z1/Yes III HMDS	30' @ 125°C		
18.2	AZ ECI coating EBR PR Bake	Z1/Rite_track or ACS	C_AZ_ECI_2um or ACS program 326 (HMDS included)	2 um	CD= 5 um (markers). EBR
18.3	PR exposure	Z5/MLA150	150 mJ/cm^2, defocus -3		Align layer 1 to 3 (bottom to channels)
18.4	PR development PR PostBake	Z1/Rite_track or ACS	Dev_AZ_ECI_2u m or program 926		

18.5	Inspection	Z6/uScope	Resolution and		
10.5	Inspection	Z0/u3cope	alignment		
19	OXIDE/ALUMINUM	NITRIDE/PLATINUM	DRY ETCHING		
19.1	Silicon Oxide/Aluminum Nitride/Platinum Dry Etching	Z2/ STS Multiplex ICP	AIN_etch, around 55".	70 nm. Help yourself with end-point detection. Start with 50" and then proceed with 10" steps. From when I see the peak of the Pt I should wait 50".	ER_Pt=about 25 nm/min. ER_AIN=about 250 nm/min. ER_SiO2=about 20 nm/min. ETCHING RATES CAN BE VERY UNSTABLE.Check that the wafer is not vibrating during the etching, otherwise we get burned PR and uncontrollable etching rate! (I am not using IBE because of Pt redeposition, causing short circuits all over the wafer)
19.2	Contacts isolation check	Multimeter			Check: substrate not conductive.
19.3	PR strip	Z2/Tepla	Strip_High , 5 min		
19.4	Remover 1165	Z2/WB_PR_Strip	Bath 1 : main remover	5min, 70°C	
19.5	Remover 1165	Z2/WB_PR_Strip	Bain 2 : clean remover	5min, 70°C	
19.6	Gentle rinse (bath 4)	Z2/WB_PR_Strip	DI Rinse (bath 4)	x 3 times	Avoid the fast rinsing to not break the microchannels
19.7	IPA Rinse	Z2/WB_PR_Strip	Petri dish		
19.8	Gentle Drying	Z2/WB_PR_Strip	10' laminar flow		Dry with N2 gun only the wafer backside. Avoid any direct flux on microchannels.
20	SILICON OXIDE ST	TRIP			
20.1	SiO2 wet etching	Z14/Acid wet bench	BHF 7:1, 1 min	20nm SiO2	ER=70 nm/min
20.2	Gentle rinse	Z14/Acid wet bench	DI Rinse x3		
20.3	IPA Rinse	Z14/Solvent wet bench	IPA bath for 1 min		

	T	T	T	T	Day could NO succe and c
					Dry with N2 gun only
		Z14/Solvent wet	Drying under		the wafer backside.
20.4	Gentle drying	bench	laminar flow		Avoid any direct flux
			(about 5')		on top of
					microchannels.
20.5	Conductivity check	Multimeter	Check resistance	R=about 10 ohm	
	·		of bottom pads		
20.6	Inspection	Z6/uScope			
20.7	Profile check	Z4/ Dektat			Check for fences and
					their height.
					Look for fences.
20.8	Inspection	Z6/SEM			Check if there are any
					seed AIN residues
					(little columns).
21	ALUMINUM NITRIE	DE/PLATINUM SPUT	TER DEPOSITION	I =	
				DR: 50 nm/min,	
				T=300°C,	
21.1	Aluminum Nitride	Z4/ Spider600	300 nm (6'	40sccmN2/10scc	DR=50nm/min
	Deposition		deposition)	m Ar, 1500 W	
				plasma, 6W	
				setpoint	
	Platinum		25 nm (6"	DR= 270nm/min,	
21.2	Deposition		deposition)	T=300°C, 1000	DR=50nm/min
				W plasma	
					Use the program
	Silicon				SiO2_F. Protective
	Oxide_Deposition				layer to prevent
	(THIS STEP IS				contact (and
	NOT STRICTLY				resisues) between PR
	NECESSARY AS			DR= around	and Pt. This
	WE ARE LESS		20 nm SiO2 (1'	20nm/min	deposition rate is
21.3	CONCERNED	Z4/Spider600	deposition)	(UNSTABLE!!),	highly unstable. Put a
	ABOUT THE			T=room T, 1000	Silicon test wafer and
	CLEANLINESS			W	check the oxide
	OF THE				thickness after 1'.
	SURFACE OF				Then proceed with
	TOP METAL)				the deposition on real
	TOP METAL)				wafers according to
					the result.
22	PHOTOLITHOGRA	PHY- Mask 4_Top_C	ontact		
22.1	Dehydratation	Z1/Yes III HMDS	30' @ 125°C		
	AZ ECI coating	Z1/Rite_track or	C_AZ_ECI_2um		
22.2	EBR	ACS	or ACS program	2 um	CD= 2 um. EBR
	PR Bake	700	or AOS program		
	1	•		•	

	I		326 (HMDS		
			included)		
00.0	DD average	75/841 8450	150 mJ/cm^2,		Align layer 4 to 3 (top
22.3	PR exposure	Z5/MLA150	defocus -3		to bottom)
22.4	PR development	Z1/Rite_track or	Dev_AZ_ECI_2u		
	PR PostBake	ACS	m or program 926		
22.5	Inspection	Z6/uScope	Resolution and		
00	OVIDE/ALLIMANUM		alignment		
23	OXIDE/ALUMINUM	I NITRIDE/PLATINUN	DRYEICHING	T .	ED Dt-shout 25
23.1	Silicon Oxide/Aluminum Nitride/Platinum Dry Etching	Z2/ STS Multiplex ICP	AIN_etch (about 2'15")	20 nm SiO2+ 300 nm AlN + 25 nm Pt. Help yourself with end-point detection. Start with 2' and then proceed with 10" steps.	ER_Pt=about 25 nm/min. ER_AIN=about 250 nm/min. ER_SiO2=about 20 nm/min. ETCHING RATES CAN BE VERY UNSTABLE. Start with 2' and proceed in steps. Wafer exchange: wait for the machine to load the wafer before starting the new process, otherwise "gate error"). Check EPD: when we are in the AIN, we see a sinusoidal trend.
23.2	Inspection	Z6/uScope	Resolution and alignment		
23.3	Contact isolation check	Multimeter			
23.4	Plasma O2 clean	Z2/Tepla	Strip_High , 5 min		
23.5	Remover 1165	Z2/WB_PR_Strip	Bath 1 : main remover	5min, 70°C	
23.6	Remover 1165	Z2/WB_PR_Strip	Bain 2 : clean remover	5min, 70°C	
23.7	Gentle rinse (bath 4)	Z2/WB_PR_Strip	DI Rinse (bath 4)	x 3 times	Avoid the fast rinsing to not break the microchannels
23.8	Gentle Drying	Z2/WB_PR_Strip	10' laminar flow		Dry with N2 gun only the wafer backside. Avoid any direct flux

					on top of
					microchannels.
23.9	Inspection	Z6/uScope			
23_b	SILICON OXIDE ST	TRIP			
23_b	SiO2 wet etching	Z14/Acid wet bench	BHF 7:1, 1 min	20nm SiO2	
23_b.					Avoid the fast rinsing
25_b. 1	Gentle rinse	Z14/Acid wet bench	DI Rinse x3		to not break the
'					microchannels
23_b.	IPA Rinse	Z14/Solvent wet	IPA bath for 1		
2	IF A MIISE	bench	min		
					Dry with N2 gun only
23_b.		Z14/Solvent wet	Drying under		the wafer backside.
3	Gentle drying	bench	laminar flow		Avoid any direct flux
3		Delicii	(about 5')		on top of
					microchannels.
23_b.	Quick Conductivity		Check resistance		Check if the etching
25_b. 4	check	Multimeter	of bottom pads	R=about 10 ohm	reached the bottom
7	CHECK		or bottom pads		pads.
23_b.	Inspection	Z6/uScope			Check alignment and
5	mspection	Zo/uocope			dimensions.
			Check isolation		
			between bottom		
23_b.			and top contacts		To check: BC'-BC',
23_b.	Conductivity check	Z16/PM8	(R>MΩ). Check	R=about 10 ohm	BC'-BC", TC'-TC',
0			also isolation		TC'-TC", BC'-TC'.
			between different		
			bottoms.		
23_b.	Profile check	Z4/ Dektat			Check for fences and
7	T TOTILE CITEOR	Z4/ Dentat			their height.
			No tilt for		Check how the step
23_b.	Inspection	Z6/SEM	dimension check.		looks like (top contact
8	mapeodon	ZO/OLIVI	Tilt 45° to check		going on top of the
			the step.		bottom contact)
24	PHOTOLITHOGRA	PHY-Mask 5_Reson	ators+Inlets		
24.1	HDMS	Z1/Yes III HMDS	30' @ 125°C		
					I put 5um of PR (3um
			C_AZ_ECI_5um		would be enough)
	AZ ECI coating	Z1/Rite_track or	or ACS program		because the release
24.2	EBR	ACS	0329 (HMDS		is going to involve
	PR Bake		included)		many etching steps. If
			oiddod)		something goes
					wrong and I need to

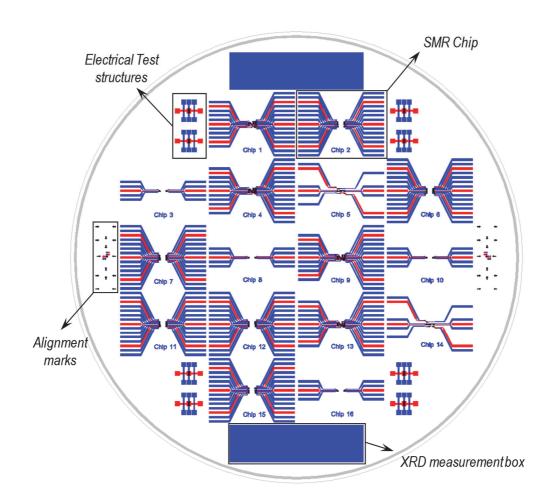
ı	1	1		I	repeat some of them,
					I am safe.
					i aiii saic.
					Alian lavan E ta lavan
			220mJ/cm^2, -3,		Align layer 5 to layer
24.3	PR exposure	MLA	high quality		3 (resonators to
					bottom contact)
	PR development	Z1/Rite_track or	Dev_AZ_ECI_5u		
24.4	PR PostBake	ACS	m or ACS		
			program 0929		
			Resolution and		
24.5	Inspection	Z6/uScope	alignment		
25	LOW STRESS SIL	ICON NITRIDE DRY	ETCHING		
			"SiO2 PR 1:1",		ED 000 / :
			ER=300nm/min,		ER_ _{PR} =300nm/min.
	Silicon Nitride Dry		5min (check		ER_ls-SiNx=280-
25.1	Etch	Z2/ AMS	deposited nitride		300nm/min. PR
			thickness from		remaining after 5'=3.5
			wafer history)		um.
					I should be able to
25.2	Inspection	Z6/uScope	Resolution and		see the silver color of
20.2	mopeodon	20/4000pc	alignment		PolySi, rough texture.
25_b	POLYSILICON DR	V ETCHING			1 olyol, lought texture.
25_0	POLISILICON DR	TEICHING	T	T	FD =420mms/msim
	Dala Oiliana Dana		HOOL AGG ADDII		ER_ _{PR} =130nm/min.
25.3	PolySilicon Dry	Z2/ AMS	"SOI ACC ADP",	6 um	ER_Polysi=4.5 um/min.
	Etch		2min		PR remaining=3.2
					um.
					I should see the
25.4	Inspection	Z6/uScope	Resolution and		green color of silicon
	'		alignment		nitride, smooth
					texture.
25_c	LOW STRESS SIL	ICON NITRIDE DRY	ETCHING		
					ER_ _{PR} =300nm/min.
25.5	Silicon Nitride Dry	Z2/ AMS	"C:O2 DD 4.4" 2	500 nm	ER_ls-SiNx=280-
25.5	Etch	ZZ/ AIVIS	"SiO2 PR 1:1", 2'	500 nm	300nm/min. PR
					remaining=2.6 um.
05.0		70/ 0	Resolution and		I should see the silver
25.6	Inspection	Z6/uScope	alignment		color of the silicon.
26	SILICON ANISOTE	ROPIC ETCHING			
			T T		This will make
					release faster.
26.1	Bosch process	Z2/ AMS	"SOI ACC ADP",	10 um	ER_PR=130 nm/min.
1-0.,			2'30"	. 5 3	_
					I FR si=5 IIm/min PR
					ER_si=5 um/min. PR remaining=2.3 um.

27	SILICON ISOTROP	PIC ETCHING			
27.1	SF6 Isotropic dry etching	Z2/ AMS	Si_release, 5 min (3+2)	30um width (15 um per side)	ER_PR=50nm/min. ER_Si (lateral)=about 6um/min. PR remaining=about 2 um. (ER_IsSiNx=100 nm/min)
27.2	Inspection	Z6/uScope	Resolution and alignment		The PR is going to burn on the tip of the longest cantilevers (due to difficult heat dissipation). Don't panic. The nitride below is fine.
27.3	SEM inspection	Z1/SEM	Tilt stage 45°		Check release, residual stress, inlets, clamps. Make sure to not need more etching, so that PR can be removed.
27.4	PR strip	Z2/Tepla	Strip_High , 5 min		Check that all the resist is gone, especially from the long cantilevers. If not, add more oxigen plasma. IN CASE OF RESIDUES AROUND THE RESONATORS (passivation coating from Bosch), it is safe to dip the wafer for 3-4 seconds in KOH + 2h neutralization in HCI. Be extra-gentle to not break the released structures. Last rinse must always be IPA.

27.5	Conductivity check	Z16/PM8	Check isolation between bottom and top contacts (R>MΩ). Check also isolation between different bottoms.	R=about 10 ohm on the same pad. R=Mohm between dfferent tracks, and top/bottom	
					Make a deep scratch
	Cleaving in chips	Z1/back (cleavage table)	71/hack		just at the edge of the
					wafer, as aligned as
					possible to the
					cleavage lines
					(scratching extra
28.1				gently multiple times	
				on the same spot). If	
					when pushing down
					to break the wafer, it
					bends, DO NOT
					INSIST, but keep
					scratching the line.
28.2	Inspection	Z6/uScope	Resolution and		
	,		alignment		

Appendix C

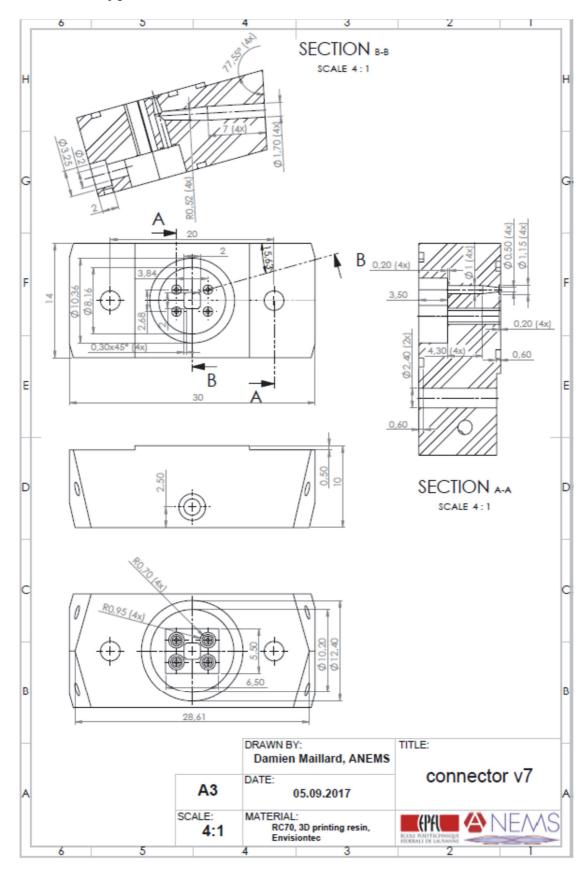
Wafer Layout



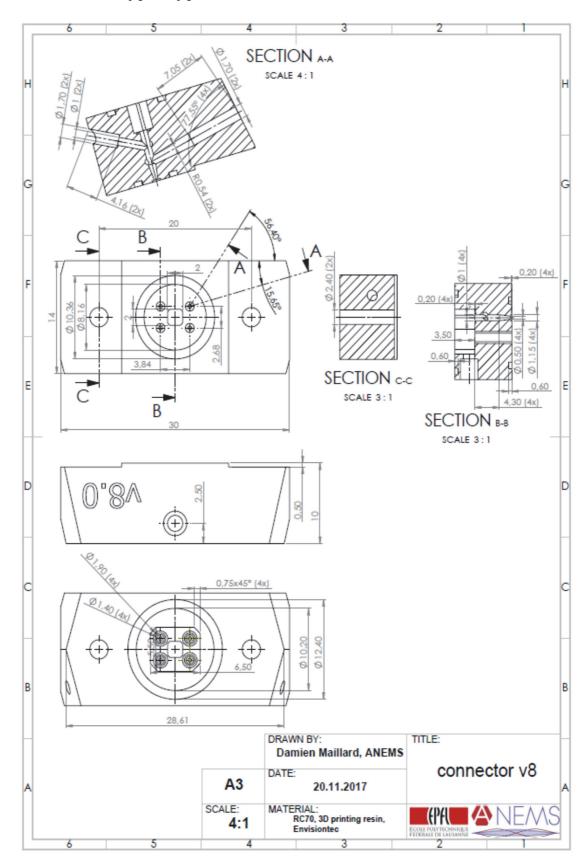
Appendix D

Microfluidic connector: drawings

First Prototype



Second Prototype: Bypass Channels



Appendix E

Codes

Lorentzian Fit - Matlab

```
function fitlor = lorentzfit(array)
z = (array(:,2)/max(array(:,2))).^2;
f = array(:,1);
%AR=5;
meff=2.55e-15;
guessQ=600;
[maximum, number] = max(z);
guessamp=pi*f(number,1)/2/guessQ*maximum;
%z = z - mean(z);
%z s = z*1e+9;
f S = f*1e-6;
ftype = fittype('off1 + amplitude*f0/2/pi/Q/((x - f0)^2 + (f0/2/Q)^2)');
opts = fitoptions('Method','NonlinearLeastSquares','Algorithm','Levenberg-
Marquardt', 'TolX', 1e-10, 'TolFun', 1e-10, 'StartPoint', [guessQ guessamp
f(number,1) 0]);
fitlor = fit(f, z, ftype, opts);
fitlor3=fitlor(f) *max(array(:,2))^2;
figure; plot(f,fitlor3,'r-',f,z*max(array(:,2))^2,'b.');
if fitlor.off1>0
    y0=sqrt(fitlor.off1);
else
    y0=0;
end
format long;
zzz1=sqrt(2*fitlor.Q/pi/fitlor.f0*fitlor.amplitude*max(array(:,2))^2);
%V/rt(Hz) at the maximum
zzz2=sqrt(1.38e-23*300*fitlor.Q/(2*pi^3*fitlor.f0^3*meff)); %m/rt(Hz)
disp(strcat('f0 from fit = ', num2str(fitlor.f0)));
```

```
disp(strcat('Q from fit = ', num2str(fitlor.Q)));
disp(strcat('Background from fit = ',
num2str(sqrt(fitlor.off1*max(array(:,2))^2))));
disp(strcat('A from fit = ', num2str(zzz1)));
disp(strcat('m/rtHz = ', num2str(zzz2)));
disp(strcat('m/V = ', num2str(zzz2/zzz1)));
```

Allan Deviation - Matlab

```
function [tau, allandev] = AllanDevLeti2(data)
time=(data(:,1)-data(1,1));
f=data(:,2);
f0=mean(f);
df=f-f0;
Ts=mean(diff(time));
t=[0:Ts:(length(f)-1)*Ts];
H=2*pi*tf([1],[1 0]);
dphi=lsim(H,f,t);
x=dphi/(2*pi*f0);
tau=Ts*[1:floor(length(x)/2)];
sigmay 2=zeros(1,length(tau));
for ii=1:1:length(tau)
    xtemp=x(1:round(tau(ii)/Ts):length(x));
    ybar=diff(xtemp)/tau(ii);
    for j=1:length(ybar)-1
        sigmay 2(ii) = sigmay 2(ii) + (ybar(j+1) - ybar(j))^2;
    end
    sigmay_2(ii) = 1/2*1/(length(ybar)-1)*sigmay_2(ii);
end
allandev=sqrt(sigmay 2);
scrsz = get(0, 'ScreenSize');
figure('Position',[scrsz(3)/10 scrsz(4)/10 scrsz(3)/2 scrsz(4)*0.8])
subplot(2,1,1);
```

```
plot(t,f*1e-6,'b.');
ylabel('Frequency (MHz)','fontsize',20); xlabel('Time (s)','fontsize',20);
title('Raw data', 'FontSize', 20);
subplot(2,1,2);
loglog(tau,allandev,'b-','LineWidth',2);
ylabel('Allan Deviation','fontsize',20); xlabel('Tau (s)','fontsize',20);
title('Allan Deviation', 'FontSize', 20);
grid(gca, 'minor')
filename='Allan Dev.png';
saveas(gcf, filename);
data2(:,1)=tau;
data2(:,2)=allandev;
DS=dataset(data2);
filename='Allan Dev.dat';
export(DS,'file',filename,'Delimiter','tab','WriteVarNames',false);
end
```

Resonator parameters - Mathematica code

```
In[57]:- (* A. De Pastina, 2017.10.05 *)
     (* Calculation of Neutral axis,
     off-axis placement and motional parameters of suspended microchannel
       resonators with inetgrated PZE electrodes. *)
     Q = 500;
                             (* quality factor *)
     f0 = 236.86 * 10^3;
                             (* [Hz], first mode *)
     YSiN = 260 * 10^9;
                            (* [Pa],
     low stress Silicon Nitride, Aln and Pt Young's modulus *)
     YAlN = 330 * 10^9;
     YPt = 158 * 10^9;
                             (*[C/m^2], PZE coefficient *)
     e31 = -0.58;
     Lcanti = 254 * 10^{-6};
                             (* Cantilever and electrodes length *)
     Lelec = 50 * 10^{-6};
     bcanti = 30 * 10^{-6};
                             (* [m], cantilever width *)
     bchannel = 10 * 10^{-6};
                             (* [m], lateral nitride flap width,
     coming from the ecthing etching of Polysilicon
      in isotropic SF6§
     bflap = 4 * 10^{-6};
     btrench = 0.6 * 10^{-6};
                             (* [m],
     width of trenches defined with the first ebeam lithography: channels' walls *)
     btopelec = 18 * 10^{-6};
                            (* [m], width of tbottom and top electrodes *)
     bbotelec = 30 * 10^{-6};
     tSiN1 = 0.5 * 10^{-6};
                              (* [m], thickness of the first layer of silicon
      nitride: channels' floor *)
     tflap = 6 * 10^{-6};
                              (* [m], thickness of the polysilicon
      layer. Corresponds to the ideal channel height in case of no nitride
      redeposition while closing EBL2*)
     tchannel = 6 * 10^{-6};
                             (* [m], channels' heigth*)
     tSiN2 = \{1.4 * 10^{-6}\};
                            (* [m], total thickness of top nitride,
     resulting from EBL1 nad EBL2 filling: channel's top wall *)
     tPt = 25 * 10^{-9};
                             (* [m], thickness of bottom metal *)
     tPttop = 50 * 10^{-9};
                            (* [m], thickness of top metal *)
     tAlN = 300 * 10^{-9};
                            (* [m], thickness of active PZE layer *)
     tbotAlN = 15 * 10^{-9};
                            (* [m], thickness of PZE seed layer *)
     tcanti = tSiN1 + tflap + tSiN2
     cantilever total thickness (no electrodes) *)
out[79]- \{7.9 \times 10^{-6}\}
```

```
In[80]: InertiaSiN = \frac{\text{bcanti} * \text{tcanti}^3}{100} - \left(2 * \frac{\text{bchannel} * \text{tchannel}^3}{100} + 2 * \frac{\text{bflap} * \text{tflap}^3}{100}\right)
      (★ [m4], Second moment of inertia, not taking into account PZE electrodes ★)
      FlexRigiditySiN = YSiN * InertiaSiN
                                                         (* [Nm2] Flexural rigidity *)
out(80]- \{7.28598 \times 10^{-22}\}
out[81]- \{1.89435 \times 10^{-10}\}
IN[82]:- InertiaAlN = (bbotelec * tbotAlN3 + btopelec * tAlN3)
      (* [m4], Second moment of inertia, AlN only *)
      FlexRigidityAlN = YAlN * InertiaAlN;
In[84]:- N[InertiaAlN]
      N[FlexRigidityAlN]
Out[84]- 4.05084 \times 10^{-26}
out[85]- 1.33678 \times 10^{-14}
Inf861:-
      InertiaPt = (bbotelec * tPt³ + btopelec * tPttop³)
      (* [m4], Second moment of inertia, Pt only *)
      FlexRigidityPt = YPt * InertiaPt;
In[88]:- N[InertiaPt]
      N[FlexRigidityPt]
out[88]- 2.26563 × 10-28
outs891- 3.57969 × 10-17
In[90]:- InertiaTOT = InertiaSiN + InertiaAlN + InertiaPt
      (* [m4], Total Second moment of inertia *)
      FlexuralRigidityTOT = FlexRigiditySiN + FlexRigidityAlN +
         FlexRigidityPt
                                 (* [m4], Total Flexural Rigidity *)
out[90]- \{7.28638 \times 10^{-22}\}
out[91]- \{1.89449 \times 10^{-10}\}
In[92]:- NeutralAxis =
       1/(bcanti * tSiN1 + 3 * btrench * tflap + bcanti * tSiN2 + bbotelec * tbotAlN + bbotelec * tPt +
            btopelec * tAlN + btopelec * tPt) (bcanti * tSiN1 * (tSiN1/2) +
           3 * btrench * tflap * (tSiN1 + tchannel / 2) + bcanti * tSiN2 * (tSiN1 + tchannel + tSiN2 / 2) +
           bbotelec * tbotAlN * (tSiN1 + tchannel + tSiN2 + tbotAlN / 2) +
           bbotelec * tPt * (tSiN1 + tchannel + tSiN2 + tbotAlN + tPt/2) +
           btopelec * tAlN * (tSiN1 + tchannel + tSiN2 + tbotAlN + tPt + tAlN / 2) +
           btopelec * tPt * (tSiN1 + tchannel + tSiN2 + tbotAlN + tPt + tAlN + tPt / 2))
         (* [m], Neutral axis of the resonant structure *)
out[92]- \{5.35543 \times 10^{-6}\}
```

```
AlNAxis =
         tSiN1 + tchannel + tSiN2 + tbotAlN + tPt + tAlN / 2
                                                                                   (* [m], Axis of the PZE layer *)
out[37]- \{8.09 \times 10^{-6}\}
                                                                     (* [m], Axis of the fluidic channel *)
In[38]:- ChannelAxis = tSiN1 + tchannel / 2
Out[38]- 3.5 \times 10^{-6}
In[39]:- ZO = (NeutralAxis - ChannelAxis) / tchannel
                                                                                 (* [/], off-axis placement *)
out[39]- {0.309238}
In[40]:- Deltaz = AlNAxis - NeutralAxis
                                                            (* [um],
           distance between PZE axis and cantilever neutral axis *)
out[40]- \{2.73457 \times 10^{-6}\}
mpage betap = e31 * Deltaz (* PZE off-center coefficient *)
Out[41]- \{-1.58605 \times 10^{-6}\}
In[42]:- Cn = 1.8751;
                                  (* Define the mode. 1.8751 for the first resonance mode *)
       Ws[x_] :=
          \left(\left(\cos\left[\operatorname{Cn}\star\mathbf{x}\right]-\operatorname{Cosh}\left[\operatorname{Cn}\star\mathbf{x}\right]\right)+\left(\frac{\cos\left[\operatorname{Cn}\right]+\operatorname{Cosh}\left[\operatorname{Cn}\right]}{\sin\left[\operatorname{Cn}\right]+\operatorname{Sinh}\left[\operatorname{Cn}\right]}\right)\left(\sinh\left[\operatorname{Cn}\star\mathbf{x}\right]-\sin\left[\operatorname{Cn}\star\mathbf{x}\right]\right)\right)
        (* Deflection function of the beam *)
       Plot[Ws[x], {x, 0, 1}]
        -0.5
Out[44]- -1.0
        -1.5
        -2.0
ln[45]:- Plot[Ws'[x], {x, 0, 1}]
                                                           (* Derivative of beam deflection function *)
                                                    0.8
                                          0.6
        -0.5
       -1.0
        -2.0
        -2.5
```

In[37]:-

```
In[46]:- (* CALCULATION OF MOTIONAL PARAMETERS ASSUMING ELECTRODES' LENGTH =
      ONE FIFTH CANTILEVER LENGTH *)
      Ws'[0.2] (* Ws'(xelec/L) *)
Out[46]- -1.21303
\ln[47]: gamman = (Ws'[0.2])^2/(Cn^4) (* Mode shape constant *)
out[47]- 0.119027
In[48]- Cm = bcanti * btopelec * Lelec * gamman * (betap) ^2

FlexuralRigidityTOT
                                                                      (*[F], motional capacitance *)
Out[48]- \{4.26729 \times 10^{-17}\}
ln[49]:- Lm = \frac{1}{Cm * (2 * 3.14 * f0)^2}
                                          (* [H], Motional Inductance *)
out[49]- {10591.2}
ln[SO]:=Rm = \frac{1}{Cm * Q * (2 * 3.14 * f0)} (* [ohm], Motional Resistance *)
out[50]- \{3.15084 \times 10^7\}
INISTI:- (* CALCULATION OF MOTIONAL PARAMETERS ASSUMING ELECTRODES' LENGTH =
       CANTILEVER LENGTH *)
in[52]:- Ws'[1] (* Ws'(xelec/L)*)
out[52]- -2.753
In[53]:- -1.213029874094648
out[53]- -1.21303
ln[54]- gamman = (Ws'[1])^2/(Cn^4) (* Mode shape constant *)
out[54]- 0.613079
\begin{array}{c} \text{ln[SS]--} \quad \textbf{Cm} = \frac{\text{bcanti} * \text{btopelec} * \text{Lcanti} * \text{ gamman} * \text{(betap) } ^2}{\text{FlexuralRigidityTOT}} \end{array}
                                                                             (*[F], motional capacitance *)
out(55)- \{1.11657 \times 10^{-15}\}
ln[56] = Lm = \frac{1}{Cm * (2 * 3.14 * f0)^2} (* [H], Motional Inductance *)
out[56]= {404.771}
ln[57]:=Rm = \frac{1}{Cm * Q * (2 * 3.14 * f0)} (* [ohm], Motional Resistance *)
out[57]- \{1.20418 \times 10^6\}
```

Bibliography

- [1] G. Tomaiuolo, "Biomechanical properties of red blood cells in health and disease towards microfluidics," *Biomicrofluidics*, vol. 8, 2014/09/17/2014.
- [2] Y. Nematbakhsh and C. T. Lim, "Cell biomechanics and its applications in human disease diagnosis," *Acta Mechanica Sinica*, vol. 31, pp. 268-273, 2015/05/12/ 2015.
- [3] M. M. Brandão, A. Fontes, M. L. Barjas-Castro, L. C. Barbosa, F. F. Costa, C. L. Cesar, *et al.*, "Optical tweezers for measuring red blood cell elasticity: application to the study of drug response in sickle cell disease," *European Journal of Haematology*, vol. 70, pp. 207-211, 2003/04/01/2003.
- [4] J. Guck, S. Schinkinger, B. Lincoln, F. Wottawah, S. Ebert, M. Romeyke, *et al.*, "Optical deformability as an inherent cell marker for testing malignant transformation and metastatic competence," *Biophysical Journal*, vol. 88, pp. 3689-3698, 2005/05// 2005.
- [5] W. Anderson, D. Kozak, V. A. Coleman, Å. K. Jämting, and M. Trau, "A comparative study of submicron particle sizing platforms: Accuracy, precision and resolution analysis of polydisperse particle size distributions," *Journal of Colloid and Interface Science*, vol. 405, pp. 322-330, 2013/09/01/2013.
- [6] S. E. Cross, Y.-S. Jin, J. Tondre, R. Wong, J. Rao, and J. K. Gimzewski, "AFM-based analysis of human metastatic cancer cells," *Nanotechnology*, vol. 19, 2008/09/24/2008.
- [7] M. Plodinec, M. Loparic, C. A. Monnier, E. C. Obermann, R. Zanetti-Dallenbach, P. Oertle, *et al.*, "The Nanomechanical Signature of Breast Cancer," *Biophysical Journal*, vol. 104, 2013/01/29/2013.
- [8] A. Calzado-Martín, M. Encinar, J. Tamayo, M. Calleja, and A. San Paulo, "Effect of Actin Organization on the Stiffness of Living Breast Cancer Cells Revealed by Peak-Force Modulation Atomic Force Microscopy," ACS Nano, vol. 10, pp. 3365-3374, 2016/03/22/2016.
- [9] G. Brock, E. Castellanos-Rizaldos, L. Hu, C. Coticchia, and J. Skog, "Liquid biopsy for cancer screening, patient stratification and monitoring," *Translational Cancer Research*, vol. 4, pp. 280-290, 2015/06/18/2015.
- [10] S. Gkountela, B. Szczerba, C. Donato, and N. Aceto, "Recent advances in the biology of human circulating tumour cells and metastasis," *ESMO Open*, vol. 1, p. e000078, 2016/08/01/2016.
- [11] CELLSEARCH® | Home. Available: https://www.cellsearchctc.com/
- [12] S. H. Au, B. D. Storey, J. C. Moore, Q. Tang, Y.-L. Chen, S. Javaid, *et al.*, "Clusters of circulating tumor cells traverse capillary-sized vessels," *Proceedings of the National Academy of Sciences*, vol. 113, pp. 4947-4952, 2016/05/03/2016.
- [13] E. Sollier, D. E. Go, J. Che, D. R. Gossett, S. O'Byrne, W. M. Weaver, *et al.*, "Size-selective collection of circulating tumor cells using Vortex technology," *Lab on a Chip*, vol. 14, pp. 63-77, 2013/11/28/2013.
- [14] A. F. Sarioglu, N. Aceto, N. Kojic, M. C. Donaldson, M. Zeinali, B. Hamza, *et al.*, "A microfluidic device for label-free, physical capture of circulating tumor cell clusters," *Nature Methods*, vol. 12, pp. 685-691, 2015/07// 2015.
- [15] P. Li, Z. Mao, Z. Peng, L. Zhou, Y. Chen, P.-H. Huang, et al., "Acoustic separation of circulating tumor cells," *Proceedings of the National Academy of Sciences*, vol. 112, pp. 4970-4975, 2015/04/21/2015.
- [16] R. H. Ewoldt, A. E. Hosoi, and G. H. McKinley, "Nonlinear viscoelastic biomaterials: meaningful characterization and engineering inspiration," *Integrative and Comparative Biology*, vol. 49, pp. 40-50, 2009/01/07/ 2009.
- [17] T. A. Waigh, "Microrheology of complex fluids," *Reports on Progress in Physics*, vol. 68, p. 685, 2005/03/01/2005.
- [18] D. Buenger, F. Topuz, and J. Groll, "Hydrogels in sensing applications," *Progress in Polymer Science*, vol. 37, pp. 1678-1719, 2012/12/01/ 2012.
- [19] K. S. Egorova, E. G. Gordeev, and V. P. Ananikov, "Biological Activity of Ionic Liquids and Their Application in Pharmaceutics and Medicine," *Chemical Reviews*, vol. 117, pp. 7132-7189, 2017/05/24/2017.
- [20] F. C. MacKintosh and C. F. Schmidt, "Microrheology," *Current Opinion in Colloid & Interface Science*, vol. 4, pp. 300-307, 1999/08/01/1999.
- [21] E. Lemaire, B. Caillard, M. Youssry, and I. Dufour, "High-frequency viscoelastic measurements of fluids based on microcantilever sensing: New modeling and experimental issues," *Sensors and Actuators A: Physical*, vol. 201, pp. 230-240, 2013/10/15/ 2013.
- [22] A. I. Romoscanu, M. B. Sayir, K. Häusler, and C. Servais, "High frequency probe for the measurement of the complex viscosity of liquids," *Measurement Science and Technology*, vol. 14, p. 451, 2003/04/01/2003.
- [23] M. Plodinec, M. Loparic, C. A. Monnier, E. C. Obermann, R. Zanetti-Dallenbach, P. Oertle, *et al.*, "The Nanomechanical Signature of Breast Cancer," *Biophysical Journal*, vol. 104, p. 321a, 2013/01/29/2013.
- [24] J. Tamayo, P. M. Kosaka, J. J. Ruz, A. San Paulo, and M. Calleja, "Biosensors based on nanomechanical systems," *Chemical Society Reviews*, vol. 42, pp. 1287-1311, 2013.

- [25] M. Calleja, P. M. Kosaka, Á. S. Paulo, and J. Tamayo, "Challenges for nanomechanical sensors in biological detection," *Nanoscale*, vol. 4, pp. 4925-4938, 2012/07/27/2012.
- [26] A. Gupta, D. Akin, and R. Bashir, "Single virus particle mass detection using microresonators with nanoscale thickness," *Applied Physics Letters*, vol. 84, pp. 1976-1978, 2004/03/15/ 2004.
- [27] G. Villanueva, F. Perez-Murano, M. Zimmermann, J. Lichtenberg, and J. Bausells, "Piezoresistive cantilevers in a commercial CMOS technology for intermolecular force detection," *Microelectronic Engineering*, vol. 83, pp. 1302-1305, Apr-Sep 2006.
- [28] G. Villanueva, J. A. Plaza, J. Montserrat, F. Perez-Murano, and J. Bausells, "Crystalline silicon cantilevers for piezoresistive detection of biomolecular forces," *Microelectronic Engineering*, vol. 85, pp. 1120-1123, May-Jun 2008.
- [29] J. Tamayo, P. M. Kosaka, J. J. Ruz, Á. S. Paulo, and M. Calleja, "Biosensors based on nanomechanical systems," *Chemical Society Reviews*, vol. 42, pp. 1287-1311, 2013/01/16/2013.
- [30] J. L. Arlett, E. B. Myers, and M. L. Roukes, "Comparative advantages of mechanical biosensors," *Nature Nanotechnology*, vol. 6, pp. 203-215, 2011/04// 2011.
- [31] G. Tosolini, G. Villanueva, F. Perez-Murano, and J. Bausells, "Silicon microcantilevers with MOSFET detection," *Microelectronic Engineering*, vol. 87, pp. 1245-1247, May-Aug 2010.
- [32] G. Villanueva, J. Montserrat, F. Perez-Murano, G. Rius, and J. Bausells, "Submicron piezoresistive cantilevers in a CMOS-compatible technology for intermolecular force detection," *Microelectronic Engineering*, vol. 73-4, pp. 480-486, Jun 2004.
- [33] J. Tamayo, J. J. Ruz, V. Pini, P. Kosaka, and M. Calleja, "Quantification of the surface stress in microcantilever biosensors: revisiting Stoney's equation," *Nanotechnology*, vol. 23, p. 475702, 2012 2012.
- [34] V. Pini, J. J. Ruz, P. M. Kosaka, O. Malvar, M. Calleja, and J. Tamayo, "How two-dimensional bending can extraordinarily stiffen thin sheets," *Scientific Reports*, vol. 6, Jul 11 2016.
- [35] J. Fritz, M. K. Baller, H. P. Lang, H. Rothuizen, P. Vettiger, E. Meyer, *et al.*, "Translating biomolecular recognition into nanomechanics," *Science*, vol. 288, pp. 316-318, Apr 14 2000.
- [36] D. Ramos, J. Tamayo, J. Mertens, M. Calleja, L. G. Villanueva, and A. Zaballos, "Detection of bacteria based on the thermomechanical noise of a nanomechanical resonator: origin of the response and detection limits," *Nanotechnology*, vol. 19, p. 035503, Jan 23 2008.
- [37] A. Boisen, S. Dohn, S. S. Keller, S. Schmid, and M. Tenje, "Cantilever-like micromechanical sensors," *Reports on Progress in Physics*, vol. 74, p. 036101, 2011/03/01/2011.
- [38] E. A. Corbin, F. Kong, C. T. Lim, W. P. King, and R. Bashir, "Biophysical properties of human breast cancer cells measured using silicon MEMS resonators and atomic force microscopy," *Lab on a Chip*, vol. 15, pp. 839-847, 2015/01/22/ 2015.
- [39] K. L. Ekinci and M. L. Roukes, "Nanoelectromechanical systems," *Review of Scientific Instruments*, vol. 76, p. 061101, 2005/06/01/2005.
- [40] M. Sansa, E. Sage, E. C. Bullard, M. Gely, T. Alava, E. Colinet, *et al.*, "Frequency fluctuations in silicon nanoresonators," *Nature Nanotechnology*, vol. 11, pp. 552-+, Jun 2016.
- [41] J. E. Sader, "Frequency response of cantilever beams immersed in viscous fluids with applications to the atomic force microscope," *Journal of Applied Physics*, vol. 84, pp. 64-76, 1998/07/01/ 1998.
- [42] K. Y. Gfeller, N. Nugaeva, and M. Hegner, "Rapid Biosensor for Detection of Antibiotic-Selective Growth of Escherichia coli," *Applied and Environmental Microbiology*, vol. 71, pp. 2626-2631, 2005/05/01/2005.
- [43] S. K. Vashist and P. Vashist, "Recent Advances in Quartz Crystal Microbalance-Based Sensors," *Journal of Sensors*, vol. 2011, p. e571405, 2011/09/19/ 2011.
- [44] K. Länge, B. E. Rapp, and M. Rapp, "Surface acoustic wave biosensors: a review," *Analytical and Bioanalytical Chemistry*, vol. 391, pp. 1509-1519, 2008/02/12/2008.
- [45] M. K. Ghatkesar, T. Braun, V. Barwich, J.-P. Ramseyer, C. Gerber, M. Hegner, *et al.*, "Resonating modes of vibrating microcantilevers in liquid," *Applied Physics Letters*, vol. 92, p. 043106, 2008/01/28/2008.
- [46] E. Oesterschulze, P. Kehrbusch, B. Radzio, E. A. Ilin, A. Thyssen, J. W. Deitmer, *et al.*, "Tailoring the interface of hybrid microresonators in viscid fluids enhances their quality factor by two orders of magnitude," *Lab on a Chip*, vol. 12, pp. 1316-1319, 2012/03/07/2012.
- [47] M. Melli, G. Scoles, and M. Lazzarino, "Fast Detection of Biomolecules in Diffusion-Limited Regime Using Micromechanical Pillars," *ACS Nano*, vol. 5, pp. 7928-7935, 2011/10/25/2011.
- [48] D. Ziegler and P. D. Ashby, "Encased Cantilevers for Ultra-Low-Noise Force Spectroscopy of Proteins and Ligand Receptor Complexes," *Biophysical Journal*, vol. 102, p. 579a, 2012/01/31/2012.
- [49] T. P. Burg and S. R. Manalis, "Suspended microchannel resonators for biomolecular detection," *Applied Physics Letters*, vol. 83, pp. 2698-2700, 2003/09/29/ 2003.

- [50] M. Rodahl, F. Höök, A. Krozer, P. Brzezinski, and B. Kasemo, "Quartz crystal microbalance setup for frequency and Q-factor measurements in gaseous and liquid environments," *Review of Scientific Instruments*, vol. 66, pp. 3924-3930, 1995/07/01/1995.
- [51] N. Kim, D.-K. Kim, and Y.-J. Cho, "Development of indirect-competitive quartz crystal microbalance immunosensor for C-reactive protein," *Sensors and Actuators B: Chemical*, vol. 143, pp. 444-448, 2009/12/04/2009.
- [52] G. Destgeer and H. J. Sung, "Recent advances in microfluidic actuation and micro-object manipulation via surface acoustic waves," *Lab on a Chip*, 2015/05/28/ 2015.
- [53] N. G. Durmuş, R. L. Lin, M. Kozberg, D. Dermici, A. Khademhosseini, and U. Demirci, "Acoustic-Based Biosensors," in *Encyclopedia of Microfluidics and Nanofluidics*, D. Li, Ed., ed: Springer New York, 2015, pp. 28-40.
- [54] S. U. Senveli, Z. Ao, S. Rawal, R. H. Datar, R. J. Cote, and O. Tigli, "A surface acoustic wave biosensor for interrogation of single tumour cells in microcavities," vol. 16, pp. 163-171, 2015/12/15/ 2015.
- [55] "Oscillating U-tube," in Wikipedia, ed, 2016.
- [56] T. P. Burg, M. Godin, S. M. Knudsen, W. Shen, G. Carlson, J. S. Foster, et al., "Weighing of biomolecules, single cells and single nanoparticles in fluid," *Nature*, vol. 446, pp. 1066-1069, 2007/04/26/ 2007.
- [57] The Koch Institute Galleries: Suspended Microchannel Resonator, 3D Rendering #1. Available: https://ki-galleries.mit.edu/2011/delgado-1
- [58] J. L. Arlett and M. L. Roukes, "Ultimate and practical limits of fluid-based mass detection with suspended microchannel resonators," *Journal of Applied Physics*, vol. 108, p. 084701, 2010/10/15/2010.
- [59] N. Cermak, S. Olcum, F. F. Delgado, S. C. Wasserman, K. R. Payer, M. A. Murakami, *et al.*, "High-throughput measurement of single-cell growth rates using serial microfluidic mass sensor arrays," *Nature Biotechnology*, vol. advance online publication, 2016/09/05/2016.
- [60] S. Byun, S. Son, D. Amodei, N. Cermak, J. Shaw, J. H. Kang, et al., "Characterizing deformability and surface friction of cancer cells," *Proceedings of the National Academy of Sciences*, vol. 110, pp. 7580-7585, 2013/05/07/2013.
- [61] Y. Weng, F. Feijó Delgado, S. Son, T. P. Burg, S. C. Wasserman, and S. R. Manalis, "Mass sensors with mechanical traps for weighing single cells in different fluids," *Lab on a Chip*, vol. 11, pp. 4174-4180, 2011 2011.
- [62] A. Sandikci, D. M. Weinstock, F. Baléras, F. F. Delgado, K. R. Payer, M. A. Murakami, *et al.*, "High-throughput measurement of single-cell growth rates using serial microfluidic mass sensor arrays," *Nature Biotechnology*, vol. 34, p. 1052, 2016/10// 2016.
- [63] M. F. Khan, S. Schmid, P. E. Larsen, Z. J. Davis, W. Yan, E. H. Stenby, et al., "Online measurement of mass density and viscosity of pL fluid samples with suspended microchannel resonator," Sensors and Actuators B: Chemical, vol. 185, pp. 456-461, 2013/08// 2013.
- [64] R. A. Barton, B. Ilic, S. S. Verbridge, B. R. Cipriany, J. M. Parpia, and H. G. Craighead, "Fabrication of a Nanomechanical Mass Sensor Containing a Nanofluidic Channel," *Nano Letters*, vol. 10, pp. 2058-2063, 2010/06/09/2010.
- [65] J. Lee, R. Chunara, W. Shen, K. Payer, K. Babcock, T. P. Burg, *et al.*, "Suspended microchannel resonators with piezoresistive sensors," *Lab on a Chip*, vol. 11, pp. 645-651, 2011/01/31/2011.
- [66] A. De Pastina, D. Maillard, and L. G. Villanueva, "Fabrication of suspended microchannel resonators with integrated piezoelectric transduction," *Microelectronic Engineering*, vol. 192, pp. 83-87, 2018/05/15/2018.
- [67] J. Tamayo, D. Ramos, J. Mertens, and M. Calleja, "Effect of the adsorbate stiffness on the resonance response of microcantilever sensors," *Applied Physics Letters*, vol. 89, p. 224104, 2006/11/27/ 2006.
- [68] G. Kotzar, M. Freas, P. Abel, A. Fleischman, S. Roy, C. Zorman, *et al.*, "Evaluation of MEMS materials of construction for implantable medical devices," *Biomaterials*, vol. 23, pp. 2737-2750, 2002/07// 2002.
- [69] J. M. Gere and B. J. Goodno, *Mechanics of Materials*: Cengage Learning, 2012.
- [70] W.-H. Chuang, T. Luger, R. K. Fettig, and R. Ghodssi, "Mechanical property characterization of LPCVD silicon nitride thin films at cryogenic temperatures," *Journal of Microelectromechanical Systems*, vol. 13, pp. 870-879, 2004/10// 2004.
- [71] S. Schmid, L. G. Villanueva, and M. L. Roukes, *Fundamentals of Nanomechanical Resonators*: Springer International Publishing, 2016.
- [72] T. J. Webster, A. A. Patel, M. N. Rahaman, and B. Sonny Bal, "Anti-infective and osteointegration properties of silicon nitride, poly(ether ether ketone), and titanium implants," *Acta Biomaterialia*, vol. 8, pp. 4447-4454, 2012/12/01/2012.
- [73] J. B. David, A. M. Glennys, Walker, and M. Glenn, "Physics and Applications of Microfluidics in Biology," *Annual Review of Biomedical Engineering*, vol. 4, pp. 261-286, 2002 2002.

- [74] J. E. Sader, T. P. Burg, and S. R. Manalis, "Energy dissipation in microfluidic beam resonators," *Journal of Fluid Mechanics*, vol. 650, pp. 215-250, 2010/05// 2010.
- [75] D. L. DeVoe, "Piezoelectric thin film micromechanical beam resonators," *Sensors and Actuators A: Physical*, vol. 88, pp. 263-272, 2001/01/05/2001.
- [76] P. Ivaldi, J. Abergel, M. H. Matheny, L. G. Villanueva, R. B. Karabalin, M. L. Roukes, *et al.*, "50 nm thick AlN film-based piezoelectric cantilevers for gravimetric detection," *Journal of Micromechanics and Microengineering*, vol. 21, p. 085023, 2011/08/01/2011.
- [77] J. D. Adams, G. Parrott, C. Bauer, T. Sant, L. Manning, M. Jones, *et al.*, "Nanowatt chemical vapor detection with a self-sensing, piezoelectric microcantilever array," *Applied Physics Letters*, vol. 83, pp. 3428-3430, 2003/10/15/2003.
- [78] N. Sinha, G. E. Wabiszewski, R. Mahameed, V. V. Felmetsger, S. M. Tanner, R. W. Carpick, *et al.*, "Piezoelectric aluminum nitride nanoelectromechanical actuators," *Applied Physics Letters*, vol. 95, p. 053106, 2009/08/03/2009.
- [79] Aluminum Nitride | AlN Material Properties. Available: http://accuratus.com/alumni.html
- [80] F. Martin, P. Muralt, M. A. Dubois, and A. Pezous, "Thickness dependence of the properties of highly c-axis textured AlN thin films," *Journal of Vacuum Science & Technology A*, vol. 22, pp. 361-365, 2004/03/01/2004.
- [81] M.-A. Dubois and P. Muralt, "Stress and piezoelectric properties of aluminum nitride thin films deposited onto metal electrodes by pulsed direct current reactive sputtering," *Journal of Applied Physics*, vol. 89, pp. 6389-6395, 2001/06/01/2001.
- [82] A. Gerbino, "Energy Dissipation in Suspended Microchannel Resonators: theoretical, numerical and experimental validation," 2018/01/01/2018.
- [83] J. Donea, A. Huerta, J. P. Ponthot, and A. Rodríguez-Ferran, "Arbitrary Lagrangian–Eulerian Methods," in *Encyclopedia of Computational Mechanics*, ed: American Cancer Society, 2004.
- [84] A. De Pastina, A. Fani, F. Gallaire, and L. G. Villanueva, "3D FEM dissipation model of suspended micro channel resonators," *5th Micro and Nano Flows Conference (MNF 2016)*.
- [85] K. Y. Yasumura, T. D. Stowe, E. M. Chow, T. Pfafman, T. W. Kenny, B. C. Stipe, et al., "Quality factors in micron- and submicron-thick cantilevers," *Journal of Microelectromechanical Systems*, vol. 9, pp. 117-125, 2000/03// 2000.
- [86] J. E. Sader, T. P. Burg, J. Lee, and S. R. Manalis, "Energy dissipation in microfluidic beam resonators: Effect of Poisson's ratio," *Physical Review E*, vol. 84, p. 026304, 2011/08/05/ 2011.
- [87] J. E. Sader, J. Lee, and S. R. Manalis, "Energy dissipation in microfluidic beam resonators: Dependence on mode number," *Journal of Applied Physics*, vol. 108, 2010/12/01/2010.
- [88] J. P. Brody, P. Yager, R. E. Goldstein, and R. H. Austin, "Biotechnology at low Reynolds numbers," *Biophysical Journal*, vol. 71, pp. 3430-3441, 1996/12// 1996.
- [89] C. A. G. Quispe, C. J. R. Coronado, and J. A. Carvalho Jr, "Glycerol: Production, consumption, prices, characterization and new trends in combustion," *Renewable and Sustainable Energy Reviews*, vol. 27, pp. 475-493, 2013/11/01/2013.
- [90] L. D. Landau and E. M. Lifshitz, *Fluid Mechanics*: Elsevier, 2013.
- [91] Physical properties of glycerine and its solutions. New York: Glycerine Producers' Association, 1963.
- [92] "Viscosity," in Wikipedia, ed, 2018.
- [93] M. F. Khan, S. Schmid, Z. J. Davis, S. Dohn, and A. Boisen, "Fabrication of resonant micro cantilevers with integrated transparent fluidic channel," *Microelectronic Engineering*, vol. 88, pp. 2300-2303, 2011/08// 2011.
- [94] T. P. Burg, A. R. Mirza, N. Milovic, C. H. Tsau, G. A. Popescu, J. S. Foster, et al., "Vacuum-Packaged Suspended Microchannel Resonant Mass Sensor for Biomolecular Detection," *Journal of Microelectromechanical Systems*, vol. 15, pp. 1466-1476, 2006/12// 2006.
- [95] J. Groenesteijn, M. J. d. Boer, J. C. Lötters, and R. J. Wiegerink, "A versatile technology platform for microfluidic handling systems, part I: fabrication and functionalization," *Microfluidics and Nanofluidics*, vol. 21, p. 127, 2017/07/01/2017.
- [96] J. Kim, J. Song, K. Kim, S. Kim, J. Song, N. Kim, *et al.*, "Hollow Microtube Resonators via Silicon Self-Assembly toward Subattogram Mass Sensing Applications," *Nano Letters*, 2016/01/27/2016.
- [97] K. R. Williams, K. Gupta, and M. Wasilik, "Etch rates for micromachining processing-Part II," *Journal of Microelectromechanical Systems*, vol. 12, pp. 761-778, 2003/12// 2003.
- [98] Y. Strausser, *Characterization in Silicon Processing*: Elsevier, 2013.
- [99] B. Wu, A. Kumar, and S. Pamarthy, "High aspect ratio silicon etch: A review," *Journal of Applied Physics*, vol. 108, p. 051101, 2010/09/01/2010.
- [100] A. Lozzi, A. De Pastina, L. G. Villanueva, and E. T. T. Yen, "Release area confinement in contour mode resonators," in 2017 IEEE International Ultrasonics Symposium (IUS), 2017, pp. 1-4.

- [101] KOH Etching | BYU Cleanroom. Available: https://cleanroom.byu.edu/KOH
- [102] M. J. Archer and F. S. Ligler, "Fabrication and Characterization of Silicon Micro-Funnels and Tapered Micro-Channels for Stochastic Sensing Applications," *Sensors*, vol. 8, pp. 3848-3872, 2008/06/09/2008.
- [103] J. Charmet, J. Bitterli, O. Sereda, M. Liley, P. Renaud, and H. Keppner, "Optimizing Parylene C Adhesion for MEMS Processes: Potassium Hydroxide Wet Etching," *Journal of Microelectromechanical Systems*, vol. 22, pp. 855-864, 2013/08// 2013.
- [104] K. R. Milkove and C. X. Wang, "Insight into the dry etching of fence-free patterned platinum structures," *Journal of Vacuum Science & Technology A: Vacuum, Surfaces, and Films*, vol. 15, pp. 596-603, 1997/05/01/1997.
- [105] Y. Temiz, R. D. Lovchik, G. V. Kaigala, and E. Delamarche, "Lab-on-a-chip devices: How to close and plug the lab?," *Microelectronic Engineering*, vol. 132, pp. 156-175, 2015/01/25/ 2015.
- [106] D. Maillard, "Development of a microfluidic interface for suspended microchannel resonators," 2016 2016.
- [107] A. D. Pastina, D. Maillard, and L. G. Villanueva, "3D printed fluidic interface with integrated vacuum encapsulation and temperature control," *in preparation*.
- [108] K. L. Ekinci, Y. T. Yang, X. M. H. Huang, and M. L. Roukes, "Balanced electronic detection of displacement in nanoelectromechanical systems," *Applied Physics Letters*, vol. 81, pp. 2253-2255, 2002/09/09/ 2002.
- [109] I. Lee, K. Park, and J. Lee, "Note: Precision viscosity measurement using suspended microchannel resonators," *Review of Scientific Instruments*, vol. 83, p. 116106, 2012/11/01/2012.
- [110] W. Lee, W. Fon, B. W. Axelrod, and M. L. Roukes, "High-sensitivity microfluidic calorimeters for biological and chemical applications," *Proceedings of the National Academy of Sciences*, vol. 106, pp. 15225-15230, 2009/09/08/ 2009.
- [111] T. Larsen, S. Schmid, L. Grönberg, A. O. Niskanen, J. Hassel, S. Dohn, *et al.*, "Ultrasensitive string-based temperature sensors," *Applied Physics Letters*, vol. 98, p. 121901, 2011/03/21/2011.
- [112] M. F. Khan, S. Schmid, A. Boisen, and T. Larsen, "Hollow micro string based calorimeter device," US20160047701A1, 2016-02-18, 2016.
- [113] T. Corman, P. Enoksson, K. Norén, and G. Stemme, "A low-pressure encapsulated resonant fluid density sensor with feedback control electronics," *Measurement Science and Technology*, vol. 11, p. 205, 2000 2000.
- [114] G. S. Kell, "Density, thermal expansivity, and compressibility of liquid water from 0.deg. to 150.deg. Correlations and tables for atmospheric pressure and saturation reviewed and expressed on 1968 temperature scale," *Journal of Chemical & Engineering Data*, vol. 20, pp. 97-105, 1975/01/01/ 1975.
- [115] D. W. Allan, "Statistics of atomic frequency standards," *Proceedings of the IEEE*, vol. 54, pp. 221-230, 1966/02// 1966.
- [116] J. Rutman and F. L. Walls, "Characterization of frequency stability in precision frequency sources," *Proceedings of the IEEE*, vol. 79, pp. 952-960, 1991/07// 1991.
- [117] L. G. Villanueva, R. B. Karabalin, M. H. Matheny, E. Kenig, M. C. Cross, and M. L. Roukes, "A Nanoscale Parametric Feedback Oscillator," *Nano Letters*, vol. 11, pp. 5054-5059, 2011/11/09/2011.
- [118] K. B. Gavan, J. v. d. Heijden, E. v. d. Drift, and H. v. d. Zant, "Resonance frequency behavior of silicon nitride cantilevers as a function of pressure in different gas environments," in *2009 IEEE Sensors*, 2009, pp. 1836-1839.

Curriculum Vitae

PERSONAL DATA

Name: Annalisa De Pastina Born: 25 June 1988, Italy

Nationality: Italian

Email: annalisa.depastina@epfl.ch

Address: EPFL STI IGM NEMS, MED 2 2326 (Batiment MED)

Station 9, Lausanne, CH-1015, Switzerland

SCIENTIFIC INTERESTS

• Silicon- and polymer-based cleanroom microfabrication

- Micro- and nano-electromechanical systems (MEMS & NEMS) for sensing applications
- Microfluidic platforms for Lab-on-chip applications
- Piezoelectric sensing and actuation at the micro- and nanoscale

EDUCATION

01/10/2013 - present	Ph.D. in Microsystems and Microelectronics, École Polytechnique Fédérale			
	de Lausanne (EPFL), Lausanne, Switzerland.			
	Supervisor: Luis Guillermo Villanueva.			
01/09/2012 - 25/01/2013	Master project in Department of Information, Electronics and			
	Telecommunication (DIET), Sapienza Università di Roma, Italy			
01/09/2010 - 25/01/2013	M.Sc. in Biomedical Engineering, Sapienza Università di Roma, Rome, Italy			
01/09/2009 - 13/12/2010	Bachelor project in Department of Information, Electronics and			
	Telecommunication (DIET), Sapienza Università di Roma, Rome, Italy			
01/09/2007 - 13/12/2010	B.Sc. in Clinical Engineering, Sapienza Università di Roma, Rome, Italy			

WORK EXPERIENCE

01/10/2013 - present

•	Lausanne, Switzerland.		
	Project: PZE-actuated suspended microchannel resonators (SMRs) for		
	sensing applications. Supervisor: Luis Guillermo Villanueva.		
01/07/2015 - 31/08/2015	Internship at University of Tokyo, Department of Bioengineering, Tokyo,		
	Japan.		
	Project: Viscoelastic characterization of thermo-responsive hydrogels.		
	Supervisor: Takamasa Sakai.		
01/02/2013 - 30/06/2013	Research assistant in Department of Information, Electronics and		
	Telecommunication (DIET), Sapienza Università di Roma, Rome, Italy.		

Research assistant in Advanced NEMS Laboratory (NEMS), EPFL,

Project: Thermally Actuated Microfluidic System for Polymerase Chain

LANGUAGES

Italian	Mother tongue	
English	Fluent (C1)	
French	Good (B1)	

Reaction Applications. Supervisor: Domenico Caputo.

Teaching activities

Teaching assistant

- TP_A-MICRO 433, Responsible: Prof. P. Renaud (Fall and Spring Semesters 2013 and 2014)
- Structural Mechanics ME-231a, Responsible: Prof. L. G. Villanueva and Prof. D. Briand (Fall Semester 2015 and 2016)

Supervised students

- <u>Semester student</u>: Antoine Aupée, "Solid-On-Liquid Technology for Suspended Microchannel Fabrication" (Fall Semester 2015)
- <u>Semester student</u>: Pierre-Emmanuel Thiriet, "Silicon fusion bonding for microfluidic applications" (Spring Semester 2016)
- <u>Semester student</u>: Mathieu Aberle, "Optimization of atomic layer deposition of aluminum oxide for suspended microchannel fabrication" (Spring Semester 2016)
- <u>Master student</u>: Damien Maillard, "Development of a microfluidic interface for suspended microchannel resonators" (Fall Semester 2016)
- <u>Master student</u>: Maurício Lucena Couto, "Energy Dissipation in Suspended Microchannel Resonators: effect of microfluidic channel off-axis placement" (Spring Semester 2017)
- <u>Master student</u>: Andrea Gerbino, "Energy Dissipation in Suspended Microchannel Resonators: theoretical, numerical and experimental validation" (Spring Semester 2017)

Attended Courses

EPFL Doctoral School

- Biomedical approach for drug evaluation, 1 ECTS (2014/02)
- Microfluidics for lab on Chip, 1 ECTS (2014/04)
- Surface and Thin Film Processes, 2 ECTS (2015/01)
- Responsible Conduct in Biomedical Research, 1 ECTS (2015/03)
- Theoretical Microfluidics, 1 ECTS (2015/04)
- Piezoelectric materials, properties and devices, 1 ECTS (2015/12)
- Design of experiments, 4 ECTS (2016/04)
- Highlights in Micro technology, 4 ECTS (2016/06)

Other

- Scaling laws in MEMS, EPFL Master Course, 2 ECTS. Result: 6/6. (2014/06)
- Wafer Bonding, FSRM Course, no credit assigned (2016/05)
- Teaching toolkit, Cape EPFL, no credit assigned, 13/10/16
- Avoid plagiarism, Learning Center EPFL, no credit assigned, 30/01/18
- French: level A2, no credit assigned, Fall semester 2014
- French: level B1, no credit assigned, Fall semester 2017

Publications

Journal Papers

- A. De Pastina, D. Maillard, and L. G. Villanueva. «Fabrication of Suspended Microchannel Resonators with Integrated Piezoelectric Transduction», Microelectronic Engineering 192 (May 15, 2018): 83–87. https://doi.org/10.1016/j.mee.2018.02.011
- A. De Pastina, D. Maillard, L. G. Villanueva. «3D printed fluidic interface with integrated vacuum encapsulation and temperature control», (in preparation)
- A. De Pastina, D. Maillard, L. G. Villanueva. «Study of frequency stability in Suspended Microchannel Resonators», (in preparation)
- A. Lozzi, A. De Pastina, E. T. T. Yen, and L. G. Villanueva « Engineered release confinment in contour mode for quality factor improvement », (under review)

Books

- A. De Pastina and L. G. Villanueva. Chapter: «Mechanical microcomponents for fluidics» to be included in the book Engineering of Micro/Nano Bio systems: Fundamentals and Applications, Springer, (under review).
- D. Caputo, G. De Cesare, A. De Pastina, P. Romano, R. Scipinotti, N. Stasio and A. Nascetti, «Thermally Actuated Microfluidic System for Polymerase Chain Reaction Applications», C. Di Natale, V. Ferrari, A. Ponzoni, G. Sberveglieri, and M. Ferrari, Eds., ed Cham: Springer International Publishing, 2014, pp. 23-27. http://www.springer.com/de/book/9783319006833

Conference Proceedings

- A. Lozzi, A. De Pastina, L. G. Villanueva, and E. T. T. Yen. «Release area confinement in contour mode resonators». In 2017 IEEE International Ultrasonics Symposium (IUS), 1–4, 2017. http://ieeexplore.ieee.org/document/8092127/
- K. M. Howell, A. De Pastina, A. Lozzi, T. Larsen, M. Faizan, and L. G. Villanueva. «Piezoelectric nanoelectromechanical systems». In 2017 19th International Conference on Solid-State Sensors, Actuators and Microsystems (TRANSDUCERS), 151–54, 2017. http://ieeexplore.ieee.org/document/7994010/
- D. Caputo, G. De Cesare, A. De Pastina, P. Romano, R. Scipinotti, N. Stasio, and A. Nascetti, «Thermally Actuated Microfluidic System for Polymerase Chain Reaction Applications», in Sensors and Microsystems: Proceedings of the 17th National Conference, Brescia, Italy, 5-7 February 2013. http://www.springer.com/de/book/9783319006833

Invited seminar

- A. De Pastina. «Suspended Microchannel Resonators (SMRs) for biological applications». Sapienza University of Rome, Italy, 2018.
- A. De Pastina and José María Fernández-Tenllado Arribas. «Resonant Nanoelectromechanical Systems: From devices to systems». CERN, Geneva, Switzerland, 2017. https://indico.cern.ch/event/598466/

Conferences, oral presentation

- A. De Pastina, D. Maillard and L. G. Villanueva. «Frequency stability in PZE-actuated Suspended Microchannel Resonators». Design, Test, Integration & Packaging of MEMS/MOEMS (DTIP 2018), Rome, Italy, 2018.
- **A. De Pastina** and L. G. Villanueva. «Frequency stability in Suspended Microchannel Resonators». *Ist Workshop on NanoFluidics and NanoMechanics*, Turin, Italy, 2017. (Invited talk) https://infoscience.epfl.ch/record/252910?ln=en
- A. De Pastina, A. Fani, F. Gallaire and L. G. Villanueva. «3D FEM dissipation model of suspended micro channel resonators». 5th Micro and Nano Flows Conference (MNF 2016), Milan, Italy, 2016. https://infoscience.epfl.ch/record/221332?ln=en

Conferences, poster presentation

- A. De Pastina, A. N. D. Aupée, T. Larsen and L. G. Villanueva. «Parylene-Based Hollow Nanomechanical Resonators For Bioapplications». 42nd Micro and Nano Engineering Conference, Vienna, Austria, 2016.
- K. Howell, W. Bashir, A. De Pastina, R. Matloub Aghdam and P. Muralt et al. «50 nm thick AlN Films for Actuation and Detection of Nanoscale Resonators». 42nd Micro and Nano Engineering Conference, Vienna, Austria, 2016.
- A. De Pastina and L. G. Villanueva. «Fabrication of suspended hollow micro-resonators integrated with PZE electrodes». *18th Conference in NanoBioTech*, Montreux, 2015.

Acknowledgements

Almost five years ago I had a Skype call with a young Professor who was looking for PhD students to start his research group. To describe what working on a PhD project would be like, he said that « There will be moments when you will feel like you are alone in the desert ». Actually, it has been much tougher than I could have imagined back then, but I never found myself alone. For this I would like to truly thank my supervisor, *Prof. Guillermo Villanueva*, for sharing with me both successes and failures, for the countless scientific discussions and his invaluable leadership. Thank you for hiring me, believing in me and always giving me the freedom to pursue my ideas.

I am also grateful to *Prof. Anja Boisen* from DTU, *Prof. Scott Manalis* from MIT and *Prof. François Gallaire* from EPFL for accepting to be the jury members of my thesis defense, as well as for reading and correcting it. Special thanks to *Prof. Jürgen Brugger* for being the jury president.

I am thankful to Prof. Jürgen Brugger and *Prof. Philippe Renaud* from EPFL, as well as *Prof. Takamasa Sakai* and *Prof. Ung-il Chung* from UTokyo for providing me the great opportunity to work in their laboratories. I am also grateful to the staff members of the EPFL clean room facilities, as well as the members of LMIS1 and LMIS4 laboratories for their support and precious advice.

This journey would not have been the same without all the current and former members of the ANEMS group, in which I found the best colleagues and friends. I am deeply thankful to *Tom* for always being there to help me, either with his deep knowledge in the lab, or with his constructive feedback on my work. Thank you especially for the support during the last months of my PhD, when your wise advice helped me to clear my mind to make decisions about my future. A special thanks goes to my dear old friend Andrea, in whom I have always found a unique support as a scientist and as a person. Thanks for all the « walks » around the building, for the music out loud in the office, for taking care to always let me know the details of all your emotional ups and downs, and for all the times we « made it round ». You, *Elena* and *Margherita* have been my piece of family here. Thank you, Damien, for joining the « SMR team » and for making the battles in the lab and cleanroom such a pleasant experience. Thank you also for proofreading my thesis, as well as the several presentations, and for always encouraging me in the moments of highest stress. You showed me the best face of this country. Thank you to Kaitlin for being so full of energy and always bring all of us together, and thanks to Marsha who recently joined the group. I would like to thank Marco, Faizan and Alberto, the weirdest and funniest trio I have ever seen, for all the weekends and nice trips, and for the crazy adventures in the cleanroom. Thanks to Josè for the nice times and his awesome electronics lectures and to Waqas for sharing with me our first year of the PhD. A big thanks to my closest friends Elmira and Soumya, for being such brilliant and kind women. Our « girls' nights » have been a breath of fresh air during the hard work of these past five years.

I have been fortunate to have supervised a number of talented and motivated students during their master studies. I would like to thank *Antoine*, *Mathieu*, *Pierre-Emmanuel*, *Damien*, *Mauricio* and *Andrea Gerbino* for contributing to and helping me to think critically about my work.

I am grateful to all the persons I met here and who contributed to make this years in Lausanne a great time. A special thanks to *Mario*, *Katy*, *Enrica*, *Laszlo*, *Maneesha*, *Mahmoud*, *Mohammad*, *Thomas*, *Samuel*, *Matthieu*, *Shenqi*, *Jonathan*, *Cristina*, *Marco*, *Alessandro*, *Anam*, *Francesca* and *Roberto*. I thank my dearest Italian friends, *Marianna* and *Anna Chiara*, who have always been so close despite the distance and our busy lifes.

Finally, I would like to thank my *parents* for being an example of hard work, resilience and courage in my life. And thank you to *Alessandro*, who followed me in this crazy adventure and always believed in me even when I did not. Thank you for your limitless patience, for listening to my rehearsals in the middle of the night, for your « fishing weekends » at -10°C in the swiss winter. You have been the sweetest partner and we did this together.

Lausanne, 29 May 2018

Annalisa De Pastina